Doklady Physics, Vol. 49, No. 6, 2004, pp. 347–349. Translated from Doklady Akademii Nauk, Vol. 396, No. 4, 2004, pp. 474–476.

PHYSICS

Effect of Optical Nonreciprocity in Crystals

V. I. Denisov

Presented by Academician A.R. Khokhlov January 22, 2004

Received January 27, 2004

The property of a material medium to provide different conditions for light propagation in the opposite directions is usually called optical nonreciprocity. This nonreciprocity can be related to the phase (propagation velocity), amplitude, and polarization of an electromagnetic wave. This work is focused on the optical nonreciprocity in phase, which is caused by different propagation velocities of the electromagnetic wave in the opposite directions.

The optical nonreciprocity of a substance is usually manifested only when it is exposed to various external fields. However, from the general theoretical standpoint, the natural optical nonreciprocity in certain crystals may exist in the absence of any external fields. In my opinion, the existence of an intracrystalline electromagnetic field is one of the causes responsible for the natural optical nonreciprocity of a crystal. In this case, the preferential direction along which the optical nonreciprocity is maximal is determined by the vector product of intracrystalline electric and magnetic fields averaged over physically infinitesimal volumes. If the average value of this product in a crystal is nonzero, then the optical nonreciprocity can arise due to the nonlinearity of vacuum electrodynamics.

As is well known [1], recent experiments at the Stanford accelerator confirmed that vacuum electrodynamics is nonlinear theory. Therefore, the propagation of electromagnetic waves in external electromagnetic fields differs from that in vacuum. In particular, as was shown in [2, 3], the propagation velocity of electromagnetic waves in the direction of the vector product of the external electric and magnetic fields differs from that in the opposite direction.

It is worth noting that, in addition to the intracrystalline electromagnetic field, other causes can be responsible for the natural optical nonreciprocity in crystals. Therefore, one of the urgent problems of crystal optics is the theoretical study of various mechanisms responsible for the optical nonreciprocity and investigation of laws governing the propagation of electromagnetic waves in nonreciprocal crystals. The search for experimental methods for studying this phenomenon and experimental verification of its various possible mechanisms are also very important.

Below, ignoring the details of various mechanisms that provide the natural optical nonreciprocity in crystals, we analyze basic laws governing the propagation of electromagnetic waves in them.

In order to solve the posed problem, it is convenient to write the coupling equations in the form $\mathbf{D} = \mathbf{D}(\mathbf{B}, \mathbf{E})$, $\mathbf{H} = \mathbf{H}(\mathbf{B}, \mathbf{E})$. This study is focused on the analysis of phenomena in anisotropic media in the presence of relatively weak electromagnetic fields, when nonlinear effects can be neglected. In this case, the coupling equations can be written as

$$D_\alpha = E_{\alpha\beta}E_\beta + \xi_{\alpha\beta}B_\beta, \quad H_\alpha = \Psi_{\alpha\beta}E_\beta + T_{\alpha\beta}B_\beta, \quad (1)$$

where $E_{\alpha\beta}$ is a tensor, $T_{\alpha\beta}$ is the tensor reciprocal to the magnetic susceptibility tensor $\mu_{\alpha\nu}$, and $\xi_{\alpha\beta}$ and $\Psi_{\alpha\beta}$ are axial tensors.

In the absence of free charges and currents, the vectors **D** and **E**, as well the axial vectors **B** and **H**, satisfy the equations of macroscopic electrodynamics:

$$\begin{aligned} \mathrm{curl}\mathbf{H} &= \frac{1}{c}\frac{\partial \mathbf{D}}{\partial t}, \quad \mathrm{div}\mathbf{D} = 0, \\ \mathrm{curl}\mathbf{E} &= -\frac{1}{c}\frac{\partial \mathbf{B}}{\partial t}, \quad \mathrm{div}\mathbf{B} = 0. \end{aligned} \quad (2)$$

The propagation of electromagnetic waves is usually studied for frequencies corresponding to the transparency band of a substance when absorption is negligibly small (see [4, 5]). As is well known, the time-averaged divergence of the Poynting vector must vanish in this case. Using macroscopic Maxwell equations (2), it is easy to show that absorption is absent under the conditions

$$E^*_{\alpha\beta} = E_{\beta\alpha}, \quad T^*_{\alpha\beta} = T_{\beta\alpha}, \quad \xi^*_{\alpha\beta} = -\Psi_{\beta\alpha}. \quad (3)$$

It follows from these conditions that the real parts of the tensors $E_{\alpha\beta}$ and $T_{\alpha\beta}$ are symmetric with respect to the permutation of the subscripts, whereas their imaginary parts are antisymmetric. An arbitrary tensor of the sec-

Moscow State University,
Vorb'evy gory, Moscow, 119899 Russia
e-mail: Denisov@srd.sinp.msu.ru

1028-3358/04/4906-0347$26.00 © 2004 MAIK "Nauka/Interperiodica"

ond rank can invariantly be represented as the sum of a symmetric tensor and an antisymmetric tensor, and an antisymmetric tensor in the three-dimensional space is dual to an axial vector. Therefore, according conditions (3), we have

$$E_{\alpha\beta} = \varepsilon_{\alpha\beta} + ie_{\alpha\beta\nu}a_\nu, \quad T_{\alpha\beta} = \tau_{\alpha\beta} + ie_{\alpha\beta\nu}f_\nu,$$
$$\xi_{\alpha\beta} = -\Psi^*_{\beta\alpha}, \quad \Psi_{\alpha\beta} = \Psi'_{\alpha\beta} + e_{\alpha\beta\nu}w_\nu + i[\Psi''_{\alpha\beta} + e_{\alpha\beta\nu}u_\nu], \tag{4}$$

where $e_{\alpha\beta\nu}$ is the absolutely antisymmetric Levi–Civita three-dimensional axial tensor and $e_{123} = 1$.

To simplify analysis of effects caused by the natural optical nonreciprocity, we neglect both the frequency dispersion and spatial dispersion and consider a weakly anisotropic crystal for which

$$\Psi'_{\alpha\beta} = \Psi''_{\alpha\beta} = 0, \quad \varepsilon_{\alpha\beta} = \varepsilon\delta_{\alpha\beta}, \quad \tau_{\alpha\beta} = \frac{\delta_{\alpha\beta}}{\mu}.$$

We assume that the vectors **u** and **w**, as well as the axial vectors **a** and **f**, are small quantities of the same order of smallness.

We now assume that a plane electromagnetic wave propagates in a crystal obeying coupling equations (1). The magnetic and electric fields of this wave are specified as

$$\mathbf{B} = \mathbf{B}_0\exp[-i(\omega t - \mathbf{kr})], \quad \mathbf{E} = \mathbf{E}_0\exp[-i(\omega t - \mathbf{kr})],$$

where ω and **k** are the frequency and the wave vector, respectively. In this case, Eqs. (2) take the form

$$\frac{\omega}{c}B_\alpha = e_{\alpha\sigma\nu}k_\sigma E_\nu, \quad \frac{\omega}{c}D_\alpha + e_{\alpha\sigma\nu}k_\sigma H_\nu = 0. \tag{5}$$

We now multiply the second of these equations by $\frac{\omega}{c}$ and substitute expressions (1) and (4) into it. As a result, taking into account the first of Eqs. (5), we arrive at the homogeneous set of three linear algebraic equations for the three components of the vector $E_\beta = (\mathbf{E})_\beta$:

$$\Pi_{\alpha\beta}E_\beta = 0, \tag{6}$$

where the three-dimensional tensor $\Pi_{\alpha\beta}$ is of the form

$$\Pi_{\alpha\beta} = \frac{\omega^2}{c^2}E_{\alpha\beta} + \frac{\omega}{c}[e_{\alpha\sigma\nu}\Psi_{\nu\beta} + e_{\beta\sigma\nu}\Psi^*_{\nu\alpha}]k_\sigma$$
$$+ e_{\alpha\sigma\nu}e_{\delta\rho\beta}k_\sigma k_\rho T_{\nu\delta}.$$

Substituting relationships (4) into this expression and using the formula

$$e_{\alpha\mu\nu}e_{\sigma\tau\beta} = \delta_{\alpha\sigma}[\delta_{\mu\tau}\delta_{\nu\beta} - \delta_{\nu\tau}\delta_{\mu\beta}]$$
$$-\delta_{\alpha\tau}[\delta_{\mu\sigma}\delta_{\nu\beta} - \delta_{\nu\beta}\delta_{\mu\sigma}] + \delta_{\alpha\beta}[\delta_{\mu\sigma}\delta_{\nu\tau} - \delta_{\mu\tau}\delta_{\nu\sigma}],$$

we reduce the tensor $\Pi_{\alpha\beta}$ to the more convenient form

$$\Pi_{\alpha\beta} = \frac{\omega^2}{c^2}[\varepsilon_{\alpha\beta} + ie_{\alpha\beta\nu}a_\nu] + \frac{\omega}{c}\{2(\mathbf{kw})\delta_{\alpha\beta}$$
$$+ i[k_\alpha u_\beta - k_\beta u_\alpha] - k_\alpha w_\beta - k_\beta w_\alpha\} - i\{k^2 e_{\alpha\beta\nu}f_\nu$$
$$+ e_{\alpha\sigma\nu}f_\sigma k_\nu k_\beta + e_{\beta\sigma\nu}f_\nu k_\sigma k_\alpha\} + \frac{1}{\mu}[k_\alpha k_\beta - k^2\delta_{\alpha\beta}]. \tag{7}$$

For the existence of nontrivial solutions of the set of Eqs. (6), its determinant must be equal to zero: $\det\|\Pi_{\alpha\beta}\| = 0$. Using tensor algebra [6], we write this equation as

$$2\Pi_{(3)} - 3\Pi_{(1)}\Pi_{(2)} + \Pi^3_{(1)} = 0. \tag{8}$$

Composing invariants of powers of tensor (7), taking relationships (5) into account, and neglecting all terms higher than squares of the small quantities **u**, **w**, **a**, and **f**, we reduce expression (8) to the form

$$\frac{\omega^4}{c^4}n^2\{n^4 - \mu^2\mathbf{a}^2\} + 2\frac{\omega^3}{c^3}\mu n^2\{2n^2(\mathbf{kw}) - \mu(\mathbf{k}[\mathbf{ua}])\}$$
$$+ \frac{\omega^2}{c^2}\{\mu^2\mathbf{k}^2[\mathbf{a}^2 - n^2\mathbf{u}^2 - n^2\mathbf{w}^2] + \mu^2 n^2[5(\mathbf{kw})^2$$
$$+ 2(\mathbf{ka})(\mathbf{kf}) + (\mathbf{ku})^2] - \mu^2(\mathbf{ka})^2 - 2n^4\mathbf{k}^2\}$$
$$+ \frac{2\omega}{c}\mu\mathbf{k}^2\{\mu(\mathbf{k}[\mathbf{ua}]) - 2n^2(\mathbf{kw})\} + \mathbf{k}^2\{\mu^2\mathbf{k}^2[\mathbf{w}^2 + \mathbf{u}^2]$$
$$- \mu^2[(\mathbf{ku})^2 + (\mathbf{kw})^2 + n^2(\mathbf{kf})^2] + \mathbf{k}^2 n^2\} = 0,$$

where, as usual, $n = \sqrt{\varepsilon\mu}$.

The last relationship is the dispersion equation. Solving this equation, we can find the frequency of the plane electromagnetic wave as a function of its wave vector.

Retaining only terms linear in the small quantities **a**, **f**, **u**, and **w**, we have

$$\omega = \frac{c}{n}\left\{k + \frac{\mu}{2n^2}\left[-2(\mathbf{kw})n \pm \sqrt{[(\mathbf{kf})n^2 - (\mathbf{ka})]^2}\right]\right\}, \tag{9}$$

where the radicand is the square of the axial scalar and the plus and minus signs correspond to the electromagnetic wave of the first and second normal modes, respectively.

It follows from expression (9) that the phase and group velocities of the electromagnetic wave in crystals with coupling equations (1) depend on the propagation

direction. In particular, in the forward direction ($\mathbf{k} = k\mathbf{N}$, where $\mathbf{N}^2 = 1$), we have

$$V_{\mathrm{ph}}^{1,2} = \frac{c}{n}\left\{1 + \frac{\mu}{2n^2}\left[-2(\mathbf{Nw})n \pm \sqrt{[(\mathbf{Nf})n^2 - (\mathbf{Na})]^2}\right]\right\},$$

$$\mathbf{V}_{\mathrm{gr}}^{1,2} = \frac{c}{n}\left\{\mathbf{N} - \frac{\mu}{n}\mathbf{w} \pm \frac{\mu\eta}{2n^2}[n^2\mathbf{f} - \mathbf{a}]\right\},$$

where η is the axial scalar equal to –1 and +1 in the left-hand and right-hand coordinate systems, respectively. In the backward direction ($\mathbf{k} = -k\mathbf{N}$), we obtain

$$V_{\mathrm{ph}}^{1,2} = \frac{c}{n}\left\{1 + \frac{\mu}{2n^2}\left[2(\mathbf{Nw})n \pm \sqrt{[(\mathbf{Na}) - (\mathbf{Nf})n^2]^2}\right]\right\},$$

$$\mathbf{V}_{\mathrm{gr}}^{1,2} = \frac{c}{n}\left\{-\mathbf{N} - \frac{\mu}{n}\mathbf{w} \pm \frac{\mu\eta}{2n^2}[n^2\mathbf{f} - \mathbf{a}]\right\}.$$

Since $(n - 1) \geq 10^{-1}$ in the transparency region of crystals, and the magnitudes of **u**, **w**, **a**, and **f** are assumed to be much smaller than unity, we can conclude that $V_{\mathrm{ph}}^{1,2} < c$ and $V_{\mathrm{gr}}^{1,2} < c$.

Thus, the natural optical nonreciprocity in the propagation velocity of electromagnetic waves can be manifested along several directions in crystals.

ACKNOWLEDGMENTS

This work was supported by the Russian Foundation for Basic Research, project no. 04-02-16604.

REFERENCES

1. D. L. Burke, R. C. Field, G. Horton-Smith, *et al.*, Phys. Rev. Lett. **79**, 1626 (1997).
2. V. I. Denisov, Phys. Rev. D **61**, 036004 (2000).
3. V. I. Denisov, J. Opt. A: Pure Appl. Opt. **2**, 372 (2000).
4. V. M. Agranovich and V. L. Ginzburg, *Crystal Optics with Spatial Dispersion, and Theory of Excitons* (Nauka, Moscow, 1979; Springer-Verlag, New York, 1984).
5. L. D. Landau and E. M. Lifshitz, *Course of Theoretical Physics*, Vol. 8: *Electrodynamics of Continuous Media* (Nauka, Moscow, 1982; Pergamon, New York, 1984).
6. I. P. Denisova and B. V. Mehta, Gen. Relativ. Gravit. **29**, 583 (1997).

Translated by G. Merzon

Doklady Physics, Vol. 49, No. 6, 2004, pp. 350–353. Translated from Doklady Akademii Nauk, Vol. 396, No. 6, 2004, pp. 762–765.

PHYSICS

Investigation of the Electrical Conductivity of a Plasma in a Spherical Tokamak

Corresponding Member of the RAS D. P. Kostomarov*, F. S. Zaitsev*, R. J. Akers, and A. G. Shishkin***

Received April 2, 2004

INTRODUCTION

Spherical tokamaks provide promising prospects for the solution of the problem of controlled thermonuclear fusion. At these setups, the toroidal geometry of a plasma has a large inverse aspect ratio. A configuration close to spherical makes it possible to develop the projects of relatively compact and cheap thermonuclear power stations.

The behavior of a plasma in spherical tokamaks is actively studied both theoretically and experimentally in the last decade. Two large spherical tokamaks—MAST (UK) and NSTX (USA)—were commissioned several years ago. Successful experiments were carried out, and a plasma with record parameters was obtained.

The problem of the electrical conductivity of a plasma is a key problem of the controlled thermonuclear fusion. The so-called neoclassical transport theory provided an answer to this problem in the late 1960s. The plasma properties in toroidal geometry were shown to differ strongly from those in cylindrical geometry. Electrical conductivity is lower in toroidal geometry. Moreover, additional electric current, so-called bootstrap current, arises, and radial energy transport increases.

Since that time, the electrical conductivity of a toroidal plasma and bootstrap current were theoretically calculated in detail in numerous works. The basic results were reviewed in [1]. However, the most general formulas were obtained only recently [2, 3].

It is of natural interest to compare theoretical results for the electrical conductivity of the plasma with experimental data. Such a comparison has not yet been made for spherical tokamaks.

This work is devoted to the study of the electrical conductivity of the plasma in discharges at the MAST setup by the mathematical simulation method and a comparison of theoretical results with experimental data.

The basic difficulty of the study of conductivity is that the parameters are not measured inside the plasma, and the accuracy of solving the inverse problem of reconstructing the internal properties is insufficient for reliable conclusion. We develop a new approach for determining the plasma conductivity in a real experiment by using accurately measured characteristics and known parameters of the setup.

MATHEMATICAL MODEL

The model of the evolution of a toroidal plasma was described in detail in [4]. Here, we give only the brief mathematical formulation of the problem. In the framework of the usual tokamak approximation, the Maxwell equations, force-balance equation, and Ohm's law are reduced to the set of the following two strongly nonlinear equations for two unknown functions $\psi(t, R, Z)$ and $F(t, \psi)$:

$$R\frac{\partial}{\partial R}\left(\frac{1}{R}\frac{\partial\psi}{\partial R}\right) + \frac{\partial^2\psi}{\partial Z^2} = -\mu_0 R j_\eta,$$

$$j_\eta(R, \psi) = \begin{cases} R\dfrac{\partial p(t, \psi)}{\partial\psi} + \dfrac{1}{2\mu_0 R}\dfrac{\partial F^2(t, \psi)}{\partial\psi} \\ \text{within } \Gamma_p(t) \\ \displaystyle\sum_{i=1}^{L} J_i(t)\delta(R - R_i)\delta Z - Z_i \\ \text{beyond } \Gamma_p(t), \end{cases} \quad (1)$$

$$\frac{\partial}{\partial t}\left(\int_0^Z \tilde{F} dZ\right)\frac{\partial\psi}{\partial Z} - \frac{\partial\psi}{\partial t}\tilde{F} = \frac{1}{\mu_0\sigma_\parallel}\left(\frac{\partial\tilde{F}}{\partial R}\frac{\partial\psi}{\partial R} + \frac{\partial\tilde{F}}{\partial Z}\frac{\partial\psi}{\partial Z}\right)$$
$$- \frac{1}{\mu_0\sigma_\parallel}\tilde{F}\left(R\frac{\partial}{\partial R}\left(\frac{1}{R}\frac{\partial\psi}{\partial R}\right) + \frac{\partial^2\psi}{\partial Z^2}\right) - \frac{R^2}{\sigma_\parallel}\mathbf{j}_{\text{add}} \cdot \mathbf{B} \quad (2)$$
$$\text{within } \Gamma_p(t),$$

* *Faculty of Computational Mathematics and Cybernetics, Moscow State University, Vorob'evy gory, Moscow, 119899 Russia*

e-mail: kostomar@cs.msu.su, zaitsev@cs.msu.su

** *Euratom/UKAEA Fusion Association, Culham Science Centre, Abingdon, United Kingdom*

1028-3358/04/4906-0350$26.00 © 2004 MAIK "Nauka/Interperiodica"

$$F(t, \psi) = \langle \tilde{F}(t, R, Z) \rangle_\psi \text{ within } \Gamma_p(t), \quad (3)$$

$$\langle \cdot \rangle_\psi \equiv \frac{\oint\limits_{\psi = \text{const}} \cdot B_{\text{pol}}^{-1} dl}{\oint\limits_{\psi \equiv \text{const}} B_{\text{pol}}^{-1} dl}. \quad (4)$$

Here, $\Gamma_p(t)$ is the plasma boundary defined as a closed surface ψ = const of the maximum width; $\mathbf{B} = B_{\text{tor}}\mathbf{i}_\eta + B_{\text{pol}}\mathbf{i}_\xi$, where $B_{\text{tor}} = \frac{F}{R}$ and B_{pol} are the toroidal and poloidal components of the magnetic field, respectively, $\mathbf{i}_\eta$ and $\mathbf{i}_\xi = \frac{(\nabla\psi \times \mathbf{i}_\eta)}{|\nabla\psi|}$ are the unit vectors in the toroidal and poloidal directions, respectively; $\sigma_\parallel$ is the electrical conductivity of the plasma along the magnetic field $\mathbf{B}$; $p(t, \psi)$ is the kinetic pressure of the plasma; $J_i(t)$ are the current in the solenoid, poloidal-field coils, and chamber walls; and the term $\frac{\mathbf{j}_{\text{add}} \cdot \mathbf{B}}{\sigma_\parallel}$ presents currents induced by external nonelectric forces such as bootstrap current, Pfirsch–Schluter current, diamagnetic current, current generated by rf waves, injection of neutrals, varying magnetic field, etc. Equation (1) is the well-known Grad–Shafranov equation obtained from the Ampere law and force balance for an axisymmetric magnetic field. Equation (2) is the projection of Ohm's law on the magnetic field $\mathbf{B}$. Both equations are written in the cylindrical coordinates (R, η, Z). The toroidal angle η does not enter into the set due to the axial symmetry.

Averaging (4) is performed by integrating over the intersection line of the magnetic surface ψ = const and plane η = const. Such an averaging simulates relatively fast processes transforming the plasma to the equilibrium state at each time, where F must be a function of ψ (see, e.g., [1]). The factor B_{pol}^{-1} ensures the equality of integral (4) to the average value with respect to the angle ξ in the coordinate system (γ, ξ, η), where γ is the label of the surface ψ = const. The integration with respect to ξ has a clear interpretation: it yields an average value over the angle.

Equations (1)–(4) are supplemented by the initial and boundary conditions

$$\psi(0, R, Z) = \psi_0(R, Z), \quad F(0, \psi) = F_0(\psi),$$
$$\lim_{R \to 0} \psi(t, R, Z) = \lim_{\substack{R \to \infty \\ Z \to \infty}} \psi(t, R, Z) = 0, \quad (5)$$
$$\tilde{F}(t, R, Z)\big|_{\Gamma_p(t)} = \frac{\mu_0}{2\pi} I_{\text{rod}}(t).$$

Here, $I_{\text{rod}}(t)$ is the electric current through the central core of the setup that is responsible for the toroidal magnetic field and $\psi_0(R, Z)$ is the solution of equilibrium equation (1) with given initial conditions $p(0, \psi)$ and $F_0(\psi)$.

The problem specified by Eqs. (1)–(5) is a two-dimensional problem with a free boundary $\Gamma_p(t)$, which is determined during solution.

PENETRATION OF AN INDUCED MAGNETIC FIELD INTO THE PLASMA

The electromagnetic induction effect is extensively used in spherical tokamaks to maintain current in a plasma. Electric voltage inducing current is primarily generated by a solenoid located at the center of a tokamak. Poloidal-field coils controlling the shape and position of the plasma can noticeably contribute to the induced current.

The induced current is often simulated under the steady-state assumption that the solenoid and other coils instantaneously induce current at any point of the plasma. Such an assumption is valid for stationary induced voltage applied to the plasma for a long time. However, the real situation in current experiments is usually far from the stationary case.

It is known that the penetration of the magnetic field into the plasma takes a certain characteristic time, estimated in [5] as $\tau_{\mathbf{B}_{\text{ind}}} = \mu_0 L^2 \sigma$, where L is the characteristic scale of the spatial variation in the magnetic field $\mathbf{B}_{\text{ind}}$ and σ is the plasma conductivity. For a typical discharge at the MAST setup, $\tau_{\mathbf{B}_{\text{ind}}} \sim 0.5$ s. Therefore, in a discharge with a duration of about 0.5 s, the induced voltage is expected to reach a stationary regime only at the final stage. Therefore, an accurate calculation of the distribution of the induced voltage U_{ind} inside the plasma is of fundamental importance for the adequate description of the experiment.

Within the boundary $\Gamma_p(t)$, $U_{\text{ind}}(t, R, Z)$ satisfies the diffusion equation

$$\frac{\partial U_{\text{ind}}}{\partial t} = \frac{1}{\mu_0 \sigma_\parallel}\left(R \frac{\partial}{\partial R}\left(\frac{1}{R}\frac{\partial U_{\text{ind}}}{\partial R}\right) + \frac{\partial^2 U_{\text{ind}}}{\partial Z^2}\right) - \frac{1}{\sigma_\parallel}\frac{\partial \sigma_\parallel}{\partial t} U_{\text{ind}}. \quad (6)$$

At the plasma boundary $(R, Z) \in \Gamma_p(t)$, we have

$$U_{\text{ind}}(t, R, Z) = -2\pi\mu_0 \sum_{i=1}^{N_c} \frac{dJ_{c,i}(t)}{dt} G(R, Z, R_{c,i}, Z_{c,i}), \quad (7)$$

where G is the Green's function of the pointlike ring current at the point $(R_{c,i}, Z_{c,i})$ and the summation is performed over all ring currents for which the point (R, Z)

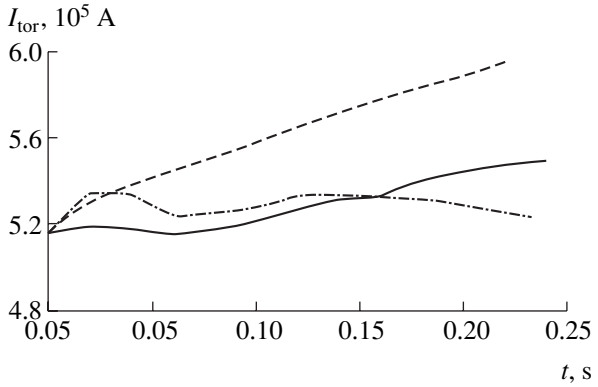

Toroidal current $I_{tor}(t)$ in the plasma. The solid, dashed, and dash–dotted lines correspond to neoclassical conductivity, Spitzer conductivity, and measurement, respectively.

is directly or almost directly visible from the point ($R_{c,i}$, $Z_{c,i}$), i.e., is not strongly shielded by the plasma.

Knowing U_{ind}, one can calculate the induction component of the source in Eq. (2) as

$$\frac{\mathbf{j}_{add,\,ind}}{\sigma_{\|}} \equiv E_{ind}\mathbf{i}_{\eta} = \frac{U_{ind}\mathbf{i}_{\eta}}{2\pi R}.$$

Calculation of U_{ind} is complicated by the large inverse aspect ratio (when R can be close to zero), the sharp dependence of the plasma conductivity on (R, Z), the plasma shielding effect of remote sections from ring coils, the complicated shape of the plasma boundary, and the necessity of including events at the discharge-formation stage.

COMPUTATIONAL EXPERIMENT

The computational experiment was carried out by means of the SCoPE code, whose capabilities, details of numerical algorithms realized in it, and structure of software were described in detail in [4].

To obtain the most adequate model, the initial parameters are specified as close as possible to the experimental conditions. The following input data were used in the model: the position of the setup walls; current $I_{rod}(t)$ in the toroidal-field coils; the coordinates of the solenoid windings and current in them; experimentally determined position of the plasma boundary (currents in the control coils of the poloidal field are chosen in calculations such that the calculated plasma boundary is close to the given boundary); mass m_β and charge e_β of plasma particles of kind β; and measured density $n_\beta(t, \psi)$, temperature $T_\beta(t, \psi)$, pressure $p = \sum_\beta n_\beta T_\beta$ of particles, and effective charge $Z_{eff}(t, \psi)$ per ion.

The evolution of equilibrium begins with the same condition for neoclassical and Spitzer models of plasma conductivity. Conductivity and bootstrap current are calculated by formulas taken from [2, 3]. The total toroidal current $I_{tor}(t)$ in the plasma for $t = 0$ is taken to be equal to the experimental value. The quantity $F(0, \psi)$ was calculated in terms of pressure $p(0, \psi)$ and plasma current density $j_\eta(0, R, Z)$ reconstructed by the EFIT code from magnetic measurements at $t = 0$. Further, the evolution of $I_{tor}(t)$ and $F(t, \psi)$ is determined by Ohm's law (2). Quantities calculated in the model are compared with experimental data. Only undoubtedly reliable data were analyzed, including the total current in the plasma $I_{tor}(t)$ and currents in the poloidal-field coils.

Figure 1 shows the evolution of the current $I_{tor}(t)$ in the MAST setup for discharge 9037, magnetic axis $R_{mag} \sim 0.8$ m, small radius ~0.5 m, elongation ~1.5, $B(R_{mag}) \sim 0.52$ T, $n_{e,d} \sim 4 \times 10^{19}$ m^{-3}, and $T_{e,d} \sim 0.4$ keV.

It is seen that current for neoclassical conductivity is closer to the experimental data than that for Spitzer conductivity. The rate of change in current in the Spitzer case is about twice as high as in the neoclassical case, which corresponds to the difference in the conductivity value. This fact has a clear physical interpretation: larger current is generated in a plasma with higher conductivity.

Comparison of the calculated and measured currents in control coils shows that the dominating difference is observed for the P5 coils, where current in the neoclassical case is about twice as close to the experimental value as in the Spitzer case. The absolute value of current in the neoclassical case is higher than in the Spitzer case. The physical explanation of the difference in currents is simple. Neoclassical conductivity has a steeper profile, which is responsible for a larger current concentration at the plasma center and its closer location to the chamber wall. Current in the coils P5 repulses the plasma from the wall. Therefore, the absolute value of current in the neoclassical case must be larger, which is consistent with calculations.

The above results, as well as numerous calculations with different variations of the mathematical model and plasma parameters, show that conductivity at the MAST setup is neoclassical.

CONCLUSIONS

Plasma conductivity at the MAST spherical tokamak was analyzed by the mathematical simulation method. An extensive computational experiment was carried out for various models of conductivity. The basic characteristics of the plasma were calculated and compared with measurements in the natural experiment. The closeness of experimental and numerical data, as well as the physical interpretation of observed effects, reliably shows that plasma conductivity at the MAST setup corresponds to neoclassical theory. Since the mathematical model is universal, the result can be extrapolated to other spherical tokamaks.

The neoclassical theoretical results were compared with experiments at tokamaks with relatively small inverse aspect ratio in [4]. According to that work, the electrical conductivity of the plasma and bootstrap current correspond to neoclassical theory.

In this work, the conclusion about the neoclassical conductivity of the toroidal plasma was generalized to the case of a large inverse aspect ratio. Moreover, we developed a new approach fundamentally different from [6]. The conclusion made in [6] is based on analysis of electric voltage on the plasma surface. The accuracy of measuring and calculating this voltage may be low due to the displacement of the plasma boundary and necessity of taking the derivative of an approximately specified function. The conclusion made in this work is based on reliable measurements of the total current in the plasma and accurate data on currents in poloidal-field coils.

ACKNOWLEDGMENTS

This work was supported by the Russian Foundation for Basic Research (project nos. 01-01-99258 and 02-01-00299), the Council of the President of the Russian Federation for Support of Young Russian Scientists and Leading Scientific Schools (project no. NSh-1349.2003.1), UK Department of Trade and Industry, Euratom, and Fusion Advanced Research Group.

REFERENCES

1. Yu. N. Dnestrovskij and D. P. Kostomarov, *Numerical Simulations of Plasmas* (Nauka, Moscow, 1993; Springer, New York, 1986).
2. O. Sauter, C. Angioni, and Y. R. Lin-Liu, Phys. Plasmas **6** (7), 2834 (1999).
3. O. Sauter, C. Angioni, and Y. R. Lin-Liu, Phys. Plasmas **9** (12), 5140 (2002).
4. F. S. Zaitsev, A. G. Shishkin, D. P. Kostomarov, *et al.*, Comput. Phys. Commun. **157**/**2**, 107 (2004).
5. F. Chen, *Introduction to Plasma Physics and Controlled Fusion* (Plenum, New York, 1983; Mir, Moscow, 1987), Vol. 1.
6. M. Kikuchi and M. Azumi, Plasma Phys. Controlled Fusion **37**, 1215 (1995).

Translated by R. Tyapaev

Doklady Physics, Vol. 49, No. 6, 2004, pp. 354–356. Translated from Doklady Akademii Nauk, Vol. 396, No. 4, 2004, pp. 477–479.

TECHNICAL PHYSICS

Polynomial Statistics and Their Application in the Problem of the Blind Identification of Radio Technical Systems

O. V. Goryachkin

Presented by Academician Yu.V. Gulyaev February 3, 2004

Received February 3, 2004

The so-called blind problem has attracted great attention in recent years [1, 2]. This problem is the problem of reconstructing unknown signals passing through a linear channel or medium with unknown characteristics over additive background noise. Blind identification, i.e., the estimation of the pulse characteristic of the channel by using only observed signals, is a key element of this problem. Blind identification is opposite to problems of the classical identification of systems, where an observed signal is used and input signals are known. The blind problem often arises in various applications of digital processing of signals and images: in radio technical systems including radiolocation, radio navigation, radio astronomy, digital television, radio communication, etc. [1, 2].

For channels with one entry and one exit, the identifiability conditions are formulated in the statistical-identification context that implies a certain set of output-signal realizations formed with the constant pulse characteristic of the channel.

The moment method implying the change of equations relating input and output signals to equations relating the corresponding moment functions is the basic approach used for blind statistical identification. For example, it is well known that the covariance functions of a stationary process at the exit of a linear system do not involve information on the phase of its transmission function, and identification is possible only for systems with the minimum phase. For this reason, identification is performed by using high-order statistics and, correspondingly, non-Gaussian models of input signals [3]. Second-order statistics can be used for blind identification of the channel for a nonstationary model of an input or output signal, including a cyclostationary signal [1]. Nevertheless, the statistics of input signals are assumed to be known *a priori* in all these cases. However, this assumption is often inapplicable. In particular, the statistic of the backscattering coefficient in radiolocation problems depends on the properties of a target, and the statistic of a signal in radiocommunication systems is determined by transmitted information.

In this work, a new approach for solving the problem of statistical blind identification is proposed on the basis of the polynomial representation of the moments of random sequences [2]. This approach transfers the problem of blind identification from the linear space to the ring of multivariate polynomials and involves a mathematical technique that was successfully developed in recent years and is based on algebraic geometry and commutative algebra. This approach makes it possible to solve the problem of blind identification for various degrees of prior uncertainty in the statistic of information signals including absolute prior uncertainty.

POLYNOMIAL STATISTICS

A polynomial cumulant of the order $k + m$, where $k = k_1 + k_2 + \ldots + k_r$ and $m = m_1 + m_2 + \ldots + m_r$, of a random vector $\mathbf{x}$ is defined as a polynomial of r variables that belongs to the ring $C[z_1, z_2, \ldots, z_r]$:

$$K^x_{k_1, k_2, \ldots, k_r, m_1, m_2, \ldots, m_r}(z_1, z_2, \ldots, z_r)$$
$$= \operatorname{cum}\{x(z_1)^{k_1} x(z_2)^{k_2} \ldots x(z_r)^{k_r} x^*(z_1)^{m_1} x^*(z_2)^{m_2} \ldots x^*(z_r)^{m_r}\}.$$

In the space C^r, the set of points at which a polynomial cumulant $K^x_{k_1, k_2, \ldots, k_r, m_1, m_2, \ldots, m_r}(z_1, z_2, \ldots, z_r)$ is equal to zero,

$$\Xi^x_{k_1, k_2, \ldots, k_r, m_1, m_2, \ldots, m_r}(t)$$
$$= \{z \in C^r: K^x_{k_1, k_2, \ldots, k_r, m_1, m_2, \ldots, m_r}(z_1, z_2, \ldots, z_r) = t\}$$

Volga State Academy of Telecommunication and Informatics, ul. L'va Tolstogo 23, Samara, 443010 Russia
e-mail: gor@mail.radiant.ru

1028-3358/04/4906-0354$26.00

is an affine variety in the space C^r and is called the given-correlation variety [2].

POSSIBILITIES OF STATISTICAL BLIND IDENTIFICATION

If an input sequence is finite and the number of realizations available for processing is sufficient for statistical identification, the signal at the exit of a linear stationary system is representable in the form of the product of polynomials over the complex number field $C[z]$:

$$y(z) = h(z)x(z) + v(z). \quad (1)$$

Here, $y(z)$, $h(z)$, $x(z)$, and $v(z) \in C[z]$ are the polynomials corresponding to an observed discrete signal, finite discrete pulse characteristic of the channel, information sequence at the channel entry, and noise counts, respectively. Algorithms of blind identification are usually constructed under the assumption that the pulse characteristic $K^x_{k_1, k_2, \ldots, k_r, m_1, m_2, \ldots, m_r}(z_1, z_2, \ldots, z_r)$ of the information signal is known. However, only very general assumptions, if any, exist for the case of the statistic information sequence under consideration.

Let us show that the structure of zero-correlation varieties of the observed signal can be used for blind identification in this case. Since the noise statistic is usually known, the zero-correlation variety of the received signal is expressed according to Eq. (1) as

$$\Xi^{y-v}_{k_1, k_2, \ldots, k_r, m_1, m_2, \ldots m_r}(0) = \Xi^{h}_{k_1, k_2, \ldots, k_r, m_1, m_2, \ldots, m_r}(0) \cup \Xi^{x}_{k_1, k_2, \ldots, k_r, m_1, m_2, \ldots, m_r}(0), \quad (2)$$

where

$$\Xi^{h}_{k_1, k_2, \ldots, k_r, m_1, m_2, \ldots, m_r}(0) = \{z \in C^r: (h(z_1))^{k_1}(h(z_2))^{k_2}\ldots(h(z_r))^{k_r}(h^*(z_1))^{m_1}(h^*(z_2))^{m_2}\ldots(h^*(z_r))^{m_r} = 0\},$$

$$\Xi^{y-v}_{k_1, k_2, \ldots, k_r, m_1, m_2, \ldots, m_r}(0) = \{z \in C^r: K^{y}_{k_1, k_2, \ldots, k_r, m_1, m_2, \ldots, m_r}(z_1, z_2, \ldots, z_r) - K^{v}_{k_1, k_2, \ldots, k_r, m_1, m_2, \ldots, m_r}(z_1, z_2, \ldots, z_r) = 0\}.$$

Since a complex univariate polynomial always has a complete set of roots, the variety $\Xi^{h}_{k_1, k_2, \ldots, k_r, m_1, m_2, \ldots, m_r}(0)$ is zero-dimensional, i.e., consists of a finite number of points corresponding to the zeros of the channel polynomial. This variety can be factorized into a combination of no more than $(L-1)^{2r}$ of simplest varieties describing points in C^r, where L is the length of the pulse characteristic of the channel. At the same time, the zero correlation variety generated by the information sequence polynomial can either also be factorized into a combination of irreducible varieties or remain irreducible. The irreducibility of the variety cannot generally be the determining factor of the separation of the channel parameters from the information sequence. However, the dimension of the variety can be the separation factor. If the variety generated by the channel polynomial is always zero-dimensional, the zero-correlation variety generated by a random information signal has a dimension of no less than one. Therefore, the zeros of the channel and information sequence can be separated by a certain procedure of selecting varieties according their dimension.

As an example, let us consider identification according to second-order polynomial statistics and independent equally distributed readings of an information sequence. In this case, the zero-correlation variety of an observed signal in C^2 disregarding noise has the form

$$\Xi^{y}_{1,0,0,1}(0) = \Xi^{h}_{1,0,0,1}(0) \cup \Xi^{x}_{1,0,0,1}(0). \quad (3)$$

The one-dimensional variety $\Xi^{x}_{1,0,0,1}(0)$ is the bundle of curves in C^2, and, as was mentioned above, $\Xi^{h}_{1,0,0,1}(0)$ is zero-dimensional. Analyzing expansion (3) by taking into account the dimension of simplest vari-

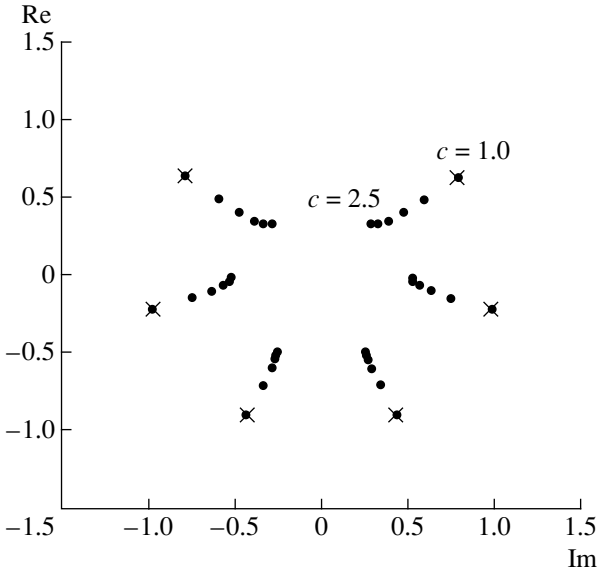

Separation of the zeros of the system characteristic of a channel according to sections of zero-correlation varieties for $L = 7$, information-sequence length $N = 7$, and 1000 realizations of the signal. The crosses and points are the zeros of the system characteristic and information sequence, respectively, upon variation in c from 1 to 2.5.

eties, *a priori* unknown varieties of the channel and information sequence can be separated by taking different sections $\Xi^{y}_{1,0,0,1}(0)$. Let

$$\mathbf{W}(c) = \mathrm{roots}(K^{y}_{1,0,0,1}(z, c)) \quad (4)$$

be the vector of the complex roots of a univariate polynomial of the variable z. Here, c is the constant determining the section of the affine variety and root(·) is the operation of calculating the roots of a univariate polynomial with allowance for their multiplicities. Then, the principle of separating roots of the pulse characteristic from roots induced by the information sequence is as follows. Change in c leads to the displacement of roots associated with the information sequence over the variety $\Xi^{x}_{1,0,0,1}(0)$, whereas roots induced by an unknown channel are not displaced. This property allows their definite separation. In particular, the figure shows the displacement of roots induced by the information sequence on the complex plane with variation in c in Eq. (4). For $c = 1$, the corresponding zeros coincide and the channel identification is impossible.

The use of polynomial statistics in problems of the blind identification of signal propagation channels allows a definite estimate of the pulse characteristic of the channel in the absence of prior information on the statistical characteristics of an input signal. The separation factor is the difference between the dimensions of the zero-correlation affine varieties generated by the determinate pulse characteristic of the channel and a random input signal.

REFERENCES

1. L. Tong and S. Perreau, Proc. IEEE **86**, 1951 (1998).
2. O. V. Goryachkin, *Methods of Blind Processing of Signals and Their Applications in Systems of Radio Engineering and Communications* (Radio i Svyaz', Moscow, 2003).
3. C. L. Nikias and M. R. Raghuveer, Proc. IEEE **75**, 869 (1987).

Translated by R. Tyapaev

Doklady Physics, Vol. 49, No. 6, 2004, pp. 357–360. Translated from Doklady Akademii Nauk, Vol. 396, No. 5, 2004, pp. 611–614.

TECHNICAL PHYSICS

Modified Method of Antenna Aperture Synthesis

V. K. Volosyuk*, V. F. Kravchenko, A. V. Ksendzuk*, and Corresponding Member of the RAS V. I. Pustovoĭt*****

Received January 22, 2004

In this study, we propose a new aperture-synthesis method realizing the ideas developed in [1, 2]. This method is based on solving the inverse optimization problem of reconstructing the specific effective scattering area, which is a statistical characteristic of a spatially nonstationary (inhomogeneous) random process, instead of the problem of reconstructing an image as a regular function of two variables. This approach implies both the operations inherent in the traditional aperture-synthesis method and the new operations of the adaptive decorrelation of received signals as random nonstationary processes, which make it possible to considerably increase (by a factor of 2–4) the resolution of the reconstruction of coherent images of surfaces. To understand the physical essence of the method, we consider the solutions of optimization problems of reconstructing the images of surfaces in two formulations.

1. The observation equation representing the model of oscillations taken from the antenna output of a synthetic-aperture radar (SAR) has the form [1–3]

$$u(t) = s(t, \dot{F}(\mathbf{r})) + n(t), \quad \mathbf{r} \in D, \quad t \in 0, 1, \ldots, T. \tag{1}$$

Here, $s(t, \dot{F}(\mathbf{r}) = \mathrm{Re}\int_D \dot{F}(\mathbf{r})\dot{s}_{\mathrm{un}}(t, \mathbf{r})d\mathbf{r}$ is the desired signal scattered by surface D and $n(t)$ is white noise with the correlation function

$$R(t_1 - t_2) = \frac{N_0}{2}\delta(t_1 - t_2),$$

where $\delta(t_1 - t_2)$ is the Dirac delta function. The complex scattering coefficient $\dot{F}(\mathbf{r})$ can be estimated by solving the integral equation

$$\dot{Y}(\mathbf{r}) = \int_0^T \dot{U}_{\mathrm{env}}\dot{s}^*_{\mathrm{env}}(t, \mathbf{r})dt = \int_D \dot{F}(\mathbf{r}_1)\dot{\Psi}(\mathbf{r}, \mathbf{r}_1)d\mathbf{r}_1, \tag{2}$$

where $\dot{s}_{\mathrm{un}}(t, \mathbf{r}) = s_{\mathrm{env}}(t, \mathbf{r})e^{j\omega_0 t}$ is the complex unit signal scattered by an element $d\mathbf{r}$ for $\dot{F}(\mathbf{r}) = 1$ and $\dot{U}_{\mathrm{env}}(t)$ is the complex envelope of the received oscillation $u(t) = \dot{U}_{\mathrm{env}}(t)e^{j\omega_0 t}$. The problem of reconstructing the complex function $\dot{F}(\mathbf{r})$ is incorrect, and its solution requires a certain regularization, for example, the statistical one by introducing *a priori* data on its behavior. However, this is of no use, because, even at the achieved SAR resolutions, the width of their ambiguity functions

$$\dot{\Psi}(\mathbf{r}, \mathbf{r}_1) = \int_0^T \dot{s}_{\mathrm{env}}(t, \mathbf{r})\dot{s}^*_{\mathrm{env}}(t, \mathbf{r})dt \tag{3}$$

considerably exceeds the characteristic correlation range of the process $\dot{F}(\mathbf{r})$. For this reason, as a primary image of the surface, we have to take either the real and imaginary parts of the SAR output effect $\dot{Y}(\mathbf{r})$, $|\dot{Y}(\mathbf{r})|$, or $|\dot{F}(\mathbf{r})|^2$. The integral on the left-hand side of Eq. (2) is representative of the essence of the aperture-synthesis method in the SAR with the focused processing of signals [4]. However, the indicated primary images have a pronounced spotty structure (speckle structure), and it is unclear what should be considered as the image and noise upon their reconstruction. To eliminate the speckle structure, averaging and window smoothing of the function $|\dot{Y}(\mathbf{r})|$ or $|\dot{Y}(\mathbf{r})|^2$ are performed. However, these operations reduce the resolution. Moreover, the smoothed function $|\dot{Y}(\mathbf{r})|^2$ is essentially an estimate of the effective backscattering cross section $\sigma^0(\mathbf{r})$ (the specific effective scattering area), and this estimate is far

* *National Aerospace University, Kharkov Aviation Institute, ul. Chkalova 17, Kharkov, 61070 Ukraine*

** *Institute of Radio Engineering and Electronics, Russian Academy of Sciences, ul. Mokhovaya 11, korp. 7, Moscow, 125009 Russia*

*** *Scientific and Technological Center of Unique Instrumentation, Russian Academy of Sciences, ul. Butlerova 15, Moscow, 117342 Russia*

1028-3358/04/4906-0357$26.00 © 2004 MAIK “Nauka/Interperiodica”

from optimal. Therefore, it is worthwhile to estimate the function $\sigma^0(\mathbf{r})$ by solving the corresponding optimization problem that is inverse not relative to $\dot{F}(\mathbf{r})$ but to $\sigma^0(\mathbf{r})$ as to the statistical characteristic of a nonstationary random process.

2. To obtain the best consistent estimate of the function $\sigma^0(\mathbf{r})$, the Bayesian quality criteria, as well as *a priori* data regularizing the inverse-problem solution, must be used. However, the primary principal operations necessary for estimating this function can also be obtained by the maximum likelihood method. This estimate will be inconsistent. It can be smoothed at the stage of the secondary processing by all known methods of window averaging (median filters, sigma filters, Lee and Frost filters, atomic functions [7], etc.). We assume that the signal $s(t, \dot{F}(\mathbf{r}))$ in Eq. (1) is stochastic due to the random nature of the scattering coefficient $\dot{F}(\mathbf{r})$. Thus, the correlation function for the entire observation equation has the form [5, 6]

$$R_u(t_1, t_2) = \langle u(t_1)u(t_2)\rangle$$
$$= \frac{1}{2}\mathrm{Re}\int_D \sigma^0(\mathbf{r})\dot{s}_{\mathrm{env}}(t_1, \mathbf{r})\dot{s}^*_{\mathrm{env}}(t_2, \mathbf{r})d\mathbf{r} + \frac{N_0}{2}\delta(t_1 - t_2), \quad (4)$$

where

$$\sigma^0_u(\mathbf{r}) = \int_D \langle \dot{F}(\mathbf{r})\dot{F}^*(\mathbf{r}_+\Delta\mathbf{r})\rangle e^{-j\mathbf{q}_\perp\Delta\mathbf{r}}d\Delta\mathbf{r}.$$

If the random process $u(t)$ is assumed to be Gaussian with the zero mathematical expectation, the likelihood functional can be written relative to the parameter $\sigma^0(\mathbf{r})$ as

$$p[u(t)|\sigma^0(\mathbf{r})] = k[\sigma^0(\mathbf{r})]$$
$$\times \exp\left\{-\frac{1}{2}\int_0^T\int_0^T u(t_1)W[t_1, t_2, \sigma^0(\mathbf{r})]u(t_2)dt_1dt_2\right\}. \quad (5)$$

Here, the inverse correlation function is found from the integral equation

$$\int_0^T W(t_1, t_2, \sigma^0(\mathbf{r}))R[t_1, t_3, \sigma^0(\mathbf{r})]dt_2 = \delta(t_1 - t_3).$$

The desired parameter $\sigma^0(\mathbf{r})$ is a function of coordinates $\mathbf{r}$. Therefore, the problem of seeking the maximum of functional (5) is variational. Solving it, we obtain the integral equation

$$\int_0^T\int_0^T \frac{\delta R[t_1, t_2, \sigma^0(\mathbf{r})]}{\delta\sigma^0(\mathbf{r})}W[t_1, t_2, \sigma^0(\mathbf{r})]dt_1dt_2$$
$$= \int_0^T\int_0^T u(t_1)\frac{\delta W[t_1, t_2, \sigma^0(\mathbf{r})]}{\delta\sigma^0(\mathbf{r})}u(t_2)dt_1dt_2. \quad (6)$$

It is appropriate to write the variational (functional) derivative of the inverse correlation function as follows:

$$\frac{\delta W[t_1, t_2, \sigma^0(\mathbf{r})]}{\delta\sigma^0(\mathbf{r})} = \int_0^T\int_0^T W[t_1, t_2, \sigma^0(\mathbf{r})]$$
$$\times \frac{\delta R[t_3, t_4, \sigma^0(\mathbf{r})]}{\delta\sigma^0(\mathbf{r})}W[t_4, t_2, \sigma^0(\mathbf{r})]dt_3dt_4.$$

Substituting this equality and the obvious identity

$$W[t_1, t_2, \sigma^0(\mathbf{r})] = \int_0^T\int_0^T W[t_1, t_3, \sigma^0(\mathbf{r})]$$
$$\times R[t_3, t_4, \sigma^0(\mathbf{r})]W[t_4, t_2, \sigma^0(\mathbf{r})]dt_3dt_4$$

into Eq. (6) and calculating the corresponding variational derivatives, we obtain the integral equation for estimating the specific effective scattering area:

$$\left|\dot{Y}_{\mathrm{out}}(\mathbf{r})^2\right| = \frac{1}{4}\int_D \sigma^0(\mathbf{r}_1)\left|\dot{\Psi}_w(\mathbf{r}_1, \mathbf{r})\right|^2 d\mathbf{r}_1 + \frac{N_0}{2}E_w(\mathbf{r}). \quad (7)$$

Here,

$$\dot{Y}_{\mathrm{out}}(\mathbf{r}) = \frac{1}{2}\int_0^T\int_0^T \dot{U}_{\mathrm{env}}(t_1, \mathbf{r})W[t_1, t_2, \sigma^0(\mathbf{r})]s^*_{\mathrm{env}}(t_2, \mathbf{r})dt_1dt_2$$
$$= \frac{1}{2}\int_0^T \dot{U}_{\mathrm{env}}(t_1)s^*_w(t_1, \mathbf{r})dt_1 \quad (8)$$

is the complex output effect of the optimal processing system for received oscillations,

$$\dot{s}_w(t, \mathbf{r}) = \int_0^T W[t_1, t_2, \sigma^0(\mathbf{r})]\dot{s}^*_{\mathrm{env}}(t_2, \mathbf{r})dt_2$$

is the reference signal, and

$$E_w(\mathbf{r}) = \int_0^T |\dot{s}_w(t, \mathbf{r})|^2 dt$$

is the reference-signal energy.

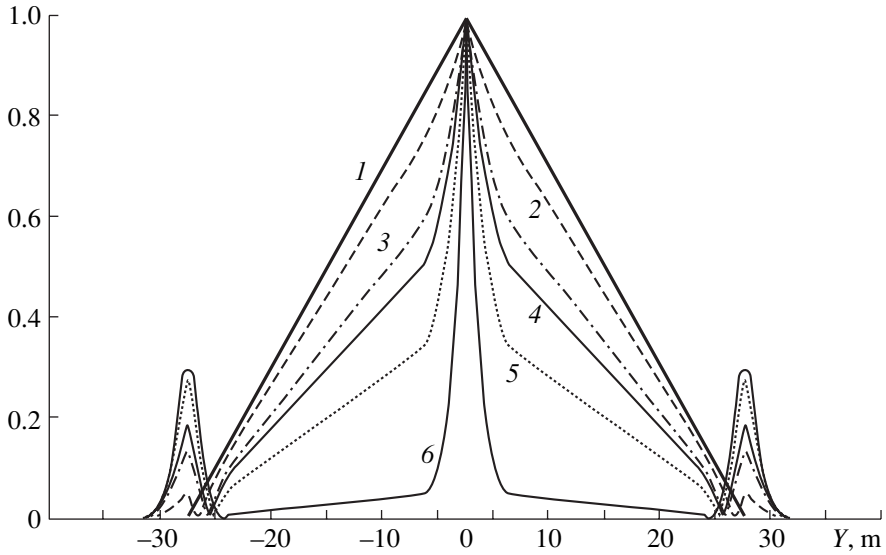

Fig. 1. Section of the absolute value of normalized spatial ambiguity functions (*1*) for matched filtering and for the decorrelation of a received signal for a signal-to-noise ratio of (*2*) 10, (*3*) 20, (*4*) 50, (*5*) 75, and (*6*) 100.

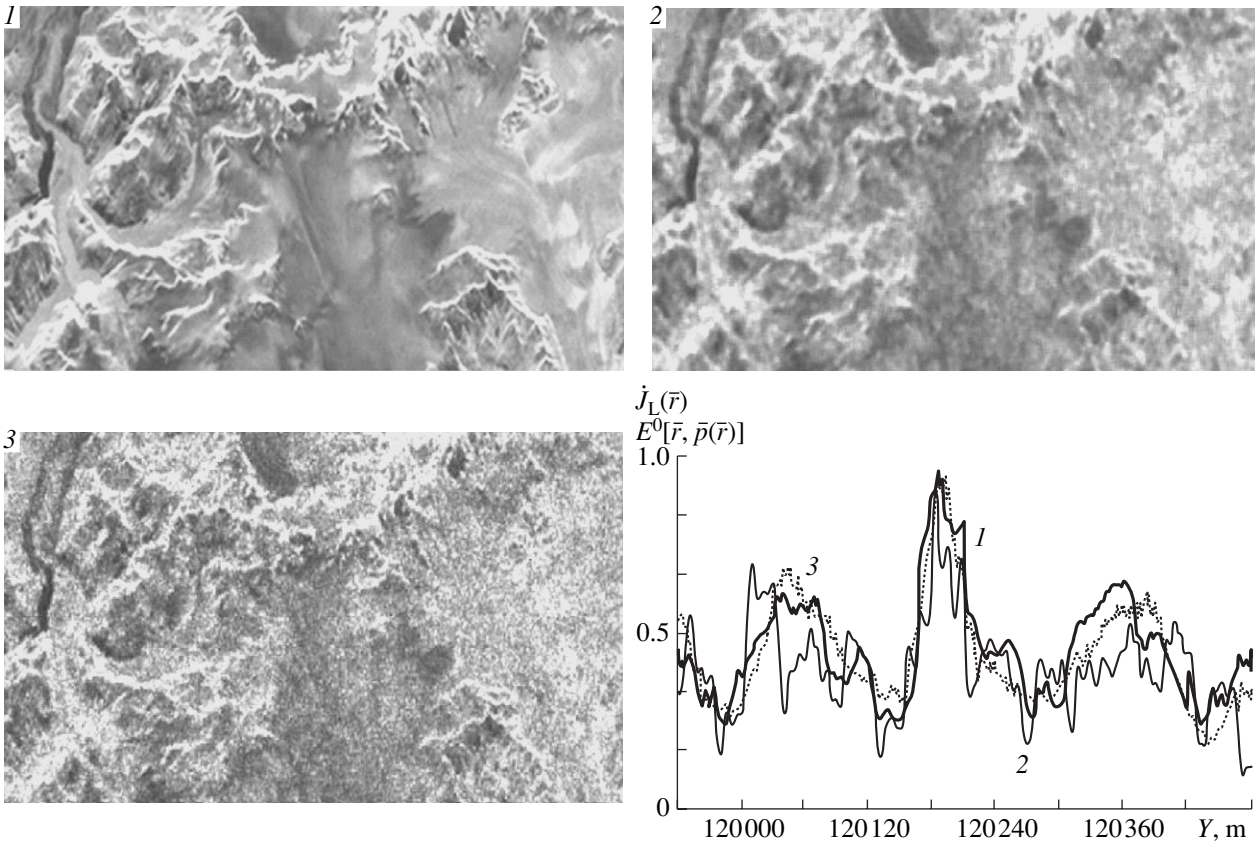

Fig. 2. Results of radar-image processing (for an average signal-to-noise ratio of 50): *1* is the initial (test) radar image, *2* is the radar image after initial processing by the matched-filtering technique with subsequent smoothing by the Lee filter, and *3* is the radar image after initial processing with decorrelation and subsequent smoothing by the Lee filter.

3. Expression (8) represents the essence of the modified method of aperture synthesis. Contrary to the classical aperture-synthesis method by the matched filtering of a received signal with a reference unit signal, the modified method implies the decorrelation of the signals reflected from the ground by integrating them with a weight $W[t_1, t_2, \sigma^0(\mathbf{r})]$. Due to this decorrelation, the characteristic speckle ranges (sizes of spots) are much

smaller than those for matched filtering. Therefore, they can then be smoothed with the same efficiency by narrower windows, which finally enables us to increase the SAR resolution. The ambiguity function

$$\dot{\Psi}_w(\mathbf{r}_1, \mathbf{r}_2) = \int_0^T\int_0^T \dot{s}_{\text{env}}(t_1, \mathbf{r}) W[t_1, t_2, \sigma^0(\mathbf{r})] \times \dot{s}^*_{\text{env}}(t_2, \mathbf{r}) dt_1 dt_2 \quad (9)$$

of this SAR is much narrower. Figure 1 exemplifies the ambiguity functions for matched filtering and decorrelation. It is noteworthy that the type of the reference signal depends on the signal-to-noise ratio. It is expedient to introduce the reference signal in algorithm (8) for a certain average signal-to-noise ratio. Otherwise, the reference signal should vary following variation of $\sigma^0(\mathbf{r})$]. Figure 2 shows the results of the formation and processing of radar images by the algorithms corresponding to the classical aperture-synthesis method and to the modified method with decorrelation.

Thus, the antenna-aperture synthesis method proposed and justified above provides an increase in the resolution of promising aerospace systems of remote sounding of natural environments by a factor of 2–4 due to the adaptive decorrelation of received signals as random processes.

REFERENCES

1. A. A. Goncharenko, V. F. Kravchenko, and V. I. Ponomarev, *Remote Probing of Inhomogeneous Media* (Mashinostroenie, Moscow, 1991).
2. S. E. Fal'kovich, V. I. Ponomarev, and Yu. V. Shkvarko, *Optimal Reception of Space–Time Signals in Radio Channels with Scattering* (Radio i Svyaz', Moscow, 1989).
3. V. K. Volosyuk, V. F. Kravchenko, and S. E. Fal'kovich, Dokl. Akad. Nauk **322**, 277 (1992) [Sov. Phys. Dokl. **37**, 23 (1992)].
4. L. J. Cutrona and G. O. Hall, IRE Trans. Mil. Electron. **6**, 119 (1962).
5. V. K. Volosyuk, V. F. Kravchenko, and V. I. Pustovoĭt, Dokl. Akad. Nauk **356**, 472 (1997) [Phys. Dokl. **42**, 542 (1997)].
6. V. K. Volosyuk, Élektromagn. Volny i Élektron. Sistemy **8** (1), 35 (2003).
7. V. F. Kravchenko, *Lectures on the Atomic Function Theory and Their Applications* (Radiotekhnika, Moscow, 2003).

Translated by V. Bukhanov

Doklady Physics, Vol. 49, No. 6, 2004, pp. 361–365. Translated from Doklady Akademii Nauk, Vol. 396, No. 4, 2004, pp. 480–484.

MECHANICS

Bifurcation of a Flow of a Viscous Fluid in a Plane Diffuser

L. D. Akulenko and S. A. Kumakshev*

Presented by Academician V.F. Zhuravlev February 5, 2004

Received February 9, 2004

The evolution of steady flows of a viscous incompressible fluid in a plane diffuser is analyzed for the classical formulation of the Jeffery–Hamel problem [1–3]. The complete solution of the problem is given depending on the determining parameters. For a fixed expansion angle, the behavior of solutions is found upon varying the Reynolds number of the basic single-mode flow. We determine the critical values at which the bifurcation of the pattern occurs and a single-mode steady flow is impossible. The revealed mechanism of bifurcation and a constructed bifurcation diagram are not available in the previously published papers on the Jeffery–Hamel problem. The critical Reynolds number at which bifurcation occurs is found as a function of the expansion angle of the diffuser. Results may be interesting for engineering and geophysical applications.

1. We consider the classical Jeffery–Hamel problem for a diffuser flow [1–3]. A fluid with density ρ and dynamic viscosity μ flows in the plane domain $\Omega = \{(r, \theta) : r > 0, |\theta| < \beta\}$, where r and θ are the polar coordinates and β is the half-expansion angle ($0 < \beta \le \pi$). On the diffuser walls, $r > 0$ and $\theta = \pm\beta$, no-slip conditions are valid, and the flow at $r = 0$ has a singularity of a constant-power source $Q < 0$. The system has two dimensionless parameters—expansion angle 2β and Reynolds number $\mathrm{Re} = \dfrac{\rho Q}{\mu} < 0$—which are insufficient for making the equations of motion completely dimensionless [3–5].

There is a self-similar solution for which the velocity field is radial,

$$v_r = -\frac{Q}{r}V(\theta), \quad v_\theta \equiv 0, \tag{1}$$

and automatically satisfies the incompressibility condition for an arbitrary smooth function $V(\theta)$. The components of the strain v and stress σ rate tensors are given by the expressions

$$v_{rr} = -v_{\theta\theta} = \frac{Q}{r^2}V(\theta), \quad v_{r\theta} = -\frac{Q}{2r^2}V'(\theta);$$
$$\sigma_{rr;\,\theta\theta} = -p \pm \frac{2\rho Q^2}{r^2\mathrm{Re}}V(\theta), \quad \sigma_{r\theta} = -\frac{\rho Q^2}{r^2\mathrm{Re}}V'(\theta). \tag{2}$$

Quantities (1) and (2) are expressed in terms of unknown functions of the velocity V and pressure p profiles, which satisfy the relations (following from the Navier–Stokes equations [3])

$$V'' + 4V - \mathrm{Re}V^2 = C = \mathrm{const}; \tag{3}$$

$$p = \frac{\rho Q^2}{2r^2\mathrm{Re}}(C - 4V). \tag{4}$$

The local no-slip boundary condition for the fluid and the integral condition of the constant rate (outflow) impose the following additional conditions on the dimensionless function $V(\theta)$:

$$V(\pm\beta) = 0, \quad \int_{-\beta}^{\beta} V(\theta)d\theta = 1. \tag{5}$$

To calculate quantities (1), (2), (4), etc., unknown function $V(\theta)$ and constant $C = V''(\pm\beta)$ must be determined from Eqs. (3) and (5) for arbitrary values $\mathrm{Re} < 0$ and $0 < \beta \le \pi$, which is a very difficult analytical and computational problem. An implicit solution of the multidimensional nonlinear boundary value problem in terms of elliptic functions by using the first integral of Eq. (3) is inapplicable for efficient accurate calculations in a rather wide region of the parameters. In the available approaches (see, e.g., [6, 7]), integral condition (5) is usually ignored and the value $V(0) = V_0$ is fixed. These assumptions strongly distort the sense and formulation of the classical Jeffery–Hamel problem [1–5]. The implicit analytical solution leads to the set of three transcendental equations for unknown integration constants. A solution of this problem is associated with fundamental computational difficulties due to insuffi-

Institute for Problems in Mechanics,
Russian Academy of Sciences,
pr. Vernadskogo 101-1, Moscow, 119526 Russia
** e-mail: kumak@ipmnet.ru*

1028-3358/04/4906-0361$26.00

cient accuracy of tabulating elliptic functions and integrals.

2. The nonlinear boundary value problem given by Eqs. (3) and (5) is efficiently solved with high accuracy by our numerical–analytical method [8] based on the modified Newton algorithm and continuation in the parameters. For convenience, the original boundary value problem is written in terms of the normalized velocity profile y, argument x, and unknown parameters γ and λ, as well as substantial known parameters a and b:

$$y(x) = 2\beta V(\theta), \quad x = \frac{1}{2}\left(\frac{\theta}{\beta} + 1\right), \quad 0 \le x \le 1, \tag{6}$$

$$a = 4\beta, \quad b = 2\beta\mathrm{Re}, \quad \lambda = 8\beta^3 C, \quad \gamma = y'(0).$$

Integral condition (5) is taken into account by means of an unknown function $z(x)$ characterizing outflow. As a result, we arrive at the Cauchy problem for y and z with unknown parameters γ and λ, which are found by including the boundary conditions

$$y'' + a^2 y - by^2 = \lambda, \quad y(0) = 0, \quad y'(0) = \gamma,$$
$$z' = y - 1, \quad z(0) = 0, \tag{7}$$
$$y(1) = z(1) = 0.$$

The parameters γ and λ must be determined as functions of the known parameters a and b. First, it is easy to determine γ and λ by continuing in the parameter $b \le 0$ for a parameter a fixed in the range $0 < a \le 2\pi$, i.e., angle β in the range $0 < \beta \le \frac{\pi}{2}$, because a solution of problem (7) is found in an explicit analytical form for $b = 0$ (Re = 0). Then, after the substitution of resulting parameters $\gamma(b)$ and $\lambda(b)$ (for fixed a), the desired function y is obtained by numerically integrating Cauchy problem (7).

Thus, for $b = 0$, we obtain

$$y_0(x) = \frac{a}{2D}\left[\cos\left(ax - \frac{a}{2}\right) - \cos\frac{a}{2}\right],$$

$$\gamma_0 = \frac{a^2}{2D}\sin\frac{a}{2}, \quad \lambda_0 = -\frac{a^3}{2D}\cos\frac{a}{2}, \tag{8}$$

$$D = \sin\frac{a}{2} - \frac{a}{2}\cos\frac{a}{2} \ne 0.$$

A solution regularly continuable in the Reynolds number Re < 0, i.e., in the parameter $b < 0$, exists if $a \ne a^* = \arg D(a)$, i.e., $\beta \ne \beta^* \equiv 2.2467047$ [5]. The critical expansion angle $2\beta^* \simeq 257°$ exceeds the straight angle and is close to 270°, corresponding to the right angle between the outer sides of the diffuser walls. For $a \ne a^*$, the solutions of problem (7) are found by the recursive refinement procedure for $\gamma(b)$ and $\lambda(b)$ for the sequence of decreasing values $b = b_k$, where $k = 0, 1, \ldots, k^*$:

$$\gamma_{n+1} = \gamma_n + \delta\gamma_n, \quad \lambda_{n+1} = \lambda_n + \delta\lambda_n,$$

$$\delta\gamma_n = -[y_n(1)s_n(1) - z_n(1)h_n(1)]\Delta_n^{-1}(1),$$

$$\delta\lambda_n = [y_n(1)w_n(1) - z_n(1)g_n(1)]\Delta_n^{-1}(1), \tag{9}$$

$$\Delta_n(x) = y_n(x)s_n(x) - h_n(x)w_n(x),$$

$$\Delta_n(1) \ne 0, \quad n = 0, 1, \ldots.$$

Here, $y_n(x)$ and $z_n(x)$ are the solutions of Cauchy problem (7) for values $\gamma_n(b)$ and $\lambda_n(b)$ known at the preceding step. The sensitivity functions g_n and w_n, as well as h_n and s_n, of the solutions y_n, as well as z_n, to the parameters γ and λ, respectively, are calculated by integrating the linear Cauchy problems with known functions $y_n(x)$, as well as $z_n(x)$ (or jointly):

$$g'' + a^2 g - 2byg = 0, \quad w' = g;$$

$$g(0) = w(0) = 0, \quad g'(0) = 1; \tag{10}$$

$$h'' + a^2 h - 2byh = 1, \ s' = h; \ h(0) = h'(0) = s(0) = 0.$$

The initial approximation for $n = 0$ is given by Eqs. (8) for $b = b_1 < b_0 = 0$. Sufficiently accurate resulting values $\gamma_n(b_1)$ and $\lambda_n(b_1)$ are used as the initial approximations for $b = b_2 < b_1$, etc. Accuracy can be characterized by the absolute values of residuals in the ordinates $y_n(1)$ and $z_n(1)$ or abscissas $\varepsilon_n = 1 - \xi_n$ and $\mu_n = 1 - \eta_n$, where ξ_n and η_n are the zeros of the functions $y_n(x)$ and $z_n(x)$, respectively, that are closest to the point $x = 1$. The algorithm given by Eqs. (9) and (10) has fast (square) convergence [4, 5, 8] and provides accurate (with relative and absolute errors of about 10^{-5}–10^{-8}) operative mass calculations and the construction of the desired dependences of y and y', as well as γ and λ, necessary for determining the kinematic and dynamic characteristics of flows of the viscous fluid in the plane diffuser. The numerical–analytical investigations testify to a complicated pattern of flows in the diffuser for various values of the parameters a and b (i.e., β and Re), which was previously analyzed either incompletely [1–3] or distortedly [6, 7].

3. Below, we present the results for comparatively small expansion angles 2β of the diffuser $\left(0 < \beta \le \frac{\pi}{2}\right)$. The limiting cases $\beta = 0$ and $\frac{\pi}{2}$ correspond to the Poiseuille flow and flow in a half-plane, respectively. Attention is focused on calculations and analysis of the

pattern of flows for small angle $\beta = 10°$, which may be of interest for engineering, hydromechanical, and geophysical applications. Figure 1 shows $\gamma(b)$ and $\lambda(b)$ for $0 \geq b \geq -25$ obtained by the above method of continuing in parameter (9) on the basis of generating solution (8).

It is found that the function $\gamma = \gamma_{(1)}(b)$ decreases from a certain positive value to zero when b decreases from zero to the critical value $b_* \approx -18.8$ corresponding to the degeneration of the basic single-mode flow, i.e., a "purely diverging flow" according to [6]. With a further decrease in $b < b_*$, a decrease in $\gamma < 0$ continues, and the flow becomes triple-mode, i.e., includes inflow and outflow sections. The outflow of the fluid ($y > 0$) is near the bisector $\left(x = \frac{1}{2}, \text{i.e., } \theta = 0\right)$. The inflow of the fluid occurs symmetrically along the walls of the diffuser ($y < 0$), i.e., near the points $x = 0$ ($x > 0$) and $x = 1$ ($x < 1$) corresponding to the angles $\theta = \mp\beta$ ($\theta > -\beta$ and $\theta < \beta$), respectively. The triple-modality of these flows is enhanced when the parameter b decreases from b_* to the critical value $b = b^* \approx -21.7$. For $b < b^*$, solutions of this type are impossible, because the curves $\gamma_{(3)}(b)$ and $\lambda_{(3)}(b)$ at this point have vertical tangents, which corresponds to the turning point (Fig. 1).

The existence of the second branch of triple-mode flows for $b^* < b < 0$ is revealed by continuing in the parameter b to the right by means of the above approach. In this case, $\gamma_{(3)}$ decreases rapidly to $-\infty$, and $\lambda_{(3)}$ increases to $+\infty$ when $b \to 0$. For example, $\gamma_{(3)} \sim -10^3$ and $\lambda_{(3)} \sim 10^4$ for $b \approx -1$. As a result, it is found that no less than two types of triple-mode flows with strongly different characteristics, i.e., values of γ and λ, exist for $b^* < b < b_*$. Lines *1* and *2* in Fig. 2 are the triple-mode velocity profiles $y(x)$ for $b = -20$. They are symmetric about the bisector. Stability and practical realization must be discussed separately.

Analysis of the vicinity of the critical point b_*, where $\gamma = 0$, reveals the possibility of the existence of two types of double-mode asymmetric flows when b increases in the range $b_* < b < 0$. The inflow ($y > 0$) and outflow ($y < 0$) of the fluid occur near the first and second walls, respectively. Since both cases ($x = 0$, 1 or $\theta = \mp\beta$) are equivalent, the curve $\gamma_{(2)}(b)$ consists of two branches $\gamma^{\pm}_{(2)}$ symmetric about the abscissa axis, and its tangent at $b = b_*$ is vertical. An increase in the parameter b leads to the unlimited increase in $|\gamma^{\pm}_{(2)}|$ similar to the above case of triple-mode flows. The curve $\lambda_{(2)}(b)$ exists for $b_* \leq b < 0$ and increases very rapidly to infinity when $b \to 0$, as does the curve $\lambda_{(3)}(b)$.

Thus, for $b_* < b < 0$, the existence of ($\gamma_{(1)} > 0$, $\lambda_{(1)} \gtrless 0$) basic single-, ($\gamma^{\pm}_{(2)} \gtrless 0$ 0, $\lambda_{(2)} > 0$) double-, and ($\gamma_{(3)} < 0$, $\lambda_{(3)} > 0$) triple-mode flows is revealed (see

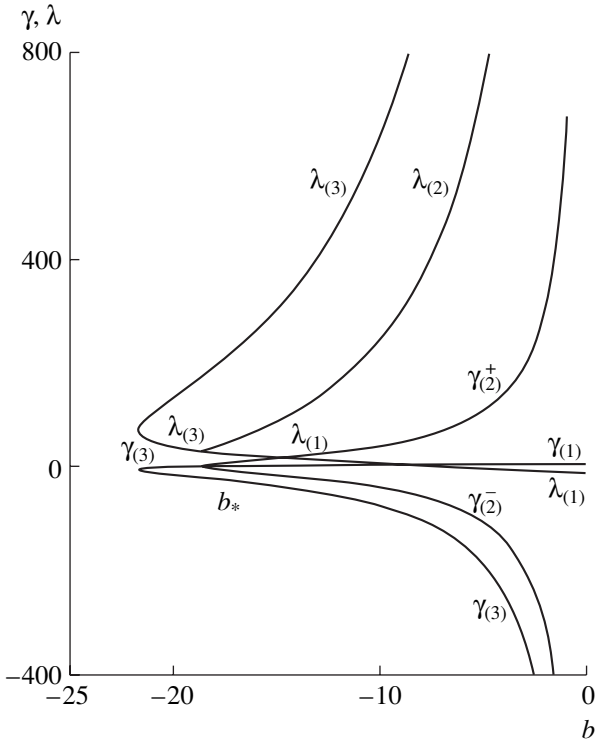

Fig. 1. Distributions $\gamma(b)$ and $\lambda(b)$, as well as the bifurcation points b_* and b^*, corresponding to ($\gamma_{(1)}$, $\lambda_{(1)}$) the basic single-, ($\gamma^{\pm}_{(2)}$, $\lambda_{(2)}$) double-, and ($\gamma_{(3)}$, $\lambda_{(3)}$) triple-mode flows for $\beta = 10° \left(\frac{\pi}{18}\right)$.

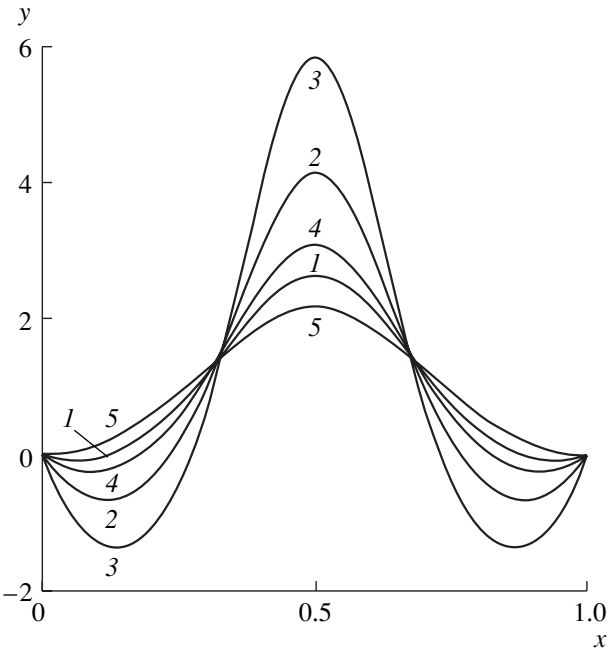

Fig. 2. Velocity profiles for triple-mode flows for b = (*1* and *2*) –21, (*3*) b_*, and (*4*) b^*, as well as for (*5*) degenerate single-mode flow for $b = b_*$.

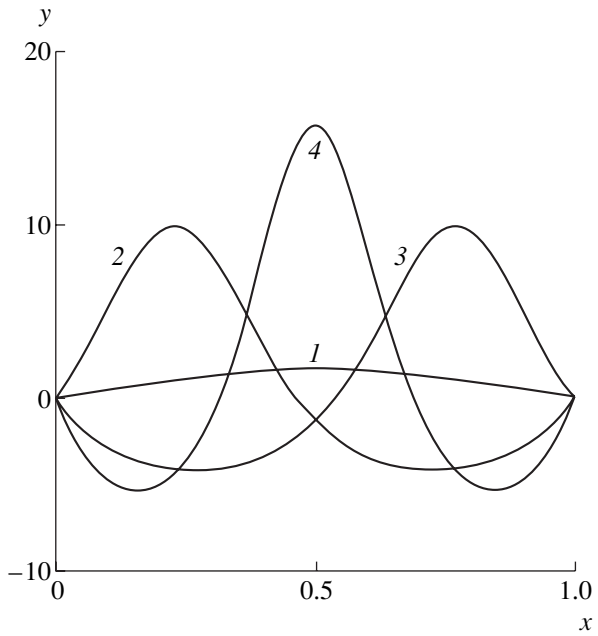

Fig. 3. Velocity profiles for (*1*) single-, (*2* and *3*) two double-, and (*4*) triple-mode flows for $b = -10$.

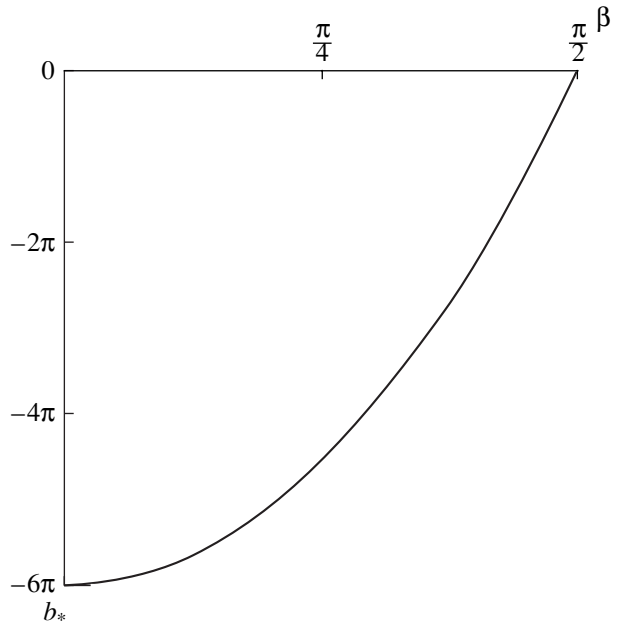

Fig. 4. Critical value b_* vs. the half-expansion angle β of the diffuser.

Fig. 1) and transitions between them are determined. The corresponding velocity profiles $y(x)$ for $b = -10$ are shown by lines *1–3*, respectively, in Fig. 3. The velocity profiles $y(x)$ have interesting properties for the critical values $b = b_*$ and b^* (Fig. 2, lines *3–5*).

The above calculations provides the first analysis of a complicated pattern of the bifurcation of flows in a comparatively narrow range $0 \ge b \ge -25$ ($0 \ge \mathrm{Re} \ge -72$ for $\beta = 10°$). This analysis reveals the mechanism of the rearrangement of flows upon varying the parameter b, i.e., the Reynolds number Re, in the unlimited half-interval $b < 0$ and for arbitrary expansion angle $0 < 2\beta \le 2\pi$.

4. The above pattern of the bifurcation of flows remains virtually unchanged when the parameter a, i.e., the diffuser expansion angle 2β ($0 < \beta \le 10°$), decreases. In particular, the value $b_* \to -6\pi$ for $\beta \to 0$ differs only slightly from $b_* = -18.8$ for $\beta = 10°$. The other characteristics (b^*, $\gamma_0 = 6$, $\lambda_0 = -12$, etc.) also change slightly.

An increase in the half-expansion angle β from +0 to $\frac{\pi}{2}$ monotonically reduces γ_0 from 6 to 0 and increases λ_0 from –12 to $4\pi^2 \approx 39.6$. The critical point b_* is also monotonically shifted to the right. Indeed, $b_* = -6\pi$ for $\beta = +0$, the numerical value $b_* \approx -18.8 > -6\pi$ is found for $\beta = \frac{\pi}{18} \simeq 0.175$ (10°) in Section 3, and constructions similar to Fig. 1 yield $b_* \simeq -14.2$ for $\beta = \frac{\pi}{4}$ (45°). Below, for the limiting value $\beta = \frac{\pi}{2}$ (90°), we show both numerically and analytically that $b_* = 0$; i.e., a single-mode (purely diverging) flow does not exist. For $b < 0$, there are two triple-mode regularly continuable flows similar to those considered above. Double-mode flows also do not exist for $\beta = \frac{\pi}{2}$. The critical value b^* can be numerically found as a function of β: $b^* \simeq -22$ for $\beta \lesssim 10°$ and $b_* \approx -18.5$ and –9 for $\beta = \frac{\pi}{4}$ and $\frac{\pi}{2}$, respectively.

The function $b_*(\beta)$ for $0 < \beta < \frac{\pi}{2}$ that determines the boundary of the existence of the single-mode flow is found in an implicit analytical form by using the first integral of the first of Eqs. (7) and quadratures:

$$-b_* = 6\xi K(\xi)L(\xi), \quad \beta = \frac{K(\xi)}{\sqrt{2}}, \quad 0 \le \xi < \infty;$$

$$K(\xi) = \int_0^1 \frac{dq}{\sqrt{f(q,\xi)}}, \quad L(\xi) = \int_0^1 \frac{q\,dq}{\sqrt{f(q,\xi)}}, \qquad (11)$$

$$f(q,\xi) = q(1-q)[2 + \xi(1+q)].$$

According to Eqs. (11), $b_* = -6\pi$ and 0 for $\beta = +0$ and $\frac{\pi}{2}$, respectively. Figure 4 shows b_* for $0 < \beta < \frac{\pi}{2}$. The maximum value of $y(x)$ and parameter λ are

expressed in terms of the values $\xi_* = \xi(\beta)$ and $b_*(\beta)$ for a given angle β as

$$y_m = y\left(\frac{1}{2}\right) = -12\beta^2\frac{\xi_*}{b_*}, \quad \lambda_* = -48\beta^4\frac{\xi_*}{b_*}(2 + \xi_*).$$

Critical values $b^*(\beta)$ determining the boundary of the existence of the triple-mode flows [see $\gamma_{(3)}(b^*)$ and $\lambda_{(3)}(b^*)$ in Fig. 1] correspond to singularities of the derivatives $\frac{\partial\gamma_{(3)}}{\partial b}$ and $\frac{\partial\lambda_{(3)}}{\partial b}$. They are determined by the above numerical–analytical procedure with fast convergence.

5. The kinematic and hydrodynamic characteristics of diffuser flows are obtained by means of the resulting expressions for $y(x, b)$, $\gamma(b)$, and $\lambda(b)$ for a fixed angle β. According to Eqs. (6),

$$V(\theta, \mathrm{Re}) = \frac{1}{2\beta}y\left(\frac{\theta/\beta + 1}{2}, 2\beta\mathrm{Re}\right),$$

$$v_r(\theta, r, \mathrm{Re}) = -\frac{Q}{r}V(\theta, \mathrm{Re}),$$
$$p(\theta, r, \mathrm{Re}) = \frac{\rho Q^2}{2r^2\mathrm{Re}}\left(\frac{\lambda}{(2\beta)^3} - 4V(\theta, \mathrm{Re})\right), \tag{12}$$
$$\lambda = \lambda(2\beta\mathrm{Re}).$$

Strain v and stress σ rate tensors are found by substituting expressions (12) for V, λ, and $V' = (2\beta)^{-2}y'$ into Eqs. (2). The stress vector components are determined in terms of σ_{rr} and $\sigma_{r\theta}$ [5]. The total force density components $\mathbf{F} = (F_r, F_\theta)$ at the distance r are given by

$$F_r = \int_{-\beta}^{\beta} r\sigma_{rr}d\theta = \frac{\rho Q^2}{r\mathrm{Re}}\left(4 - \frac{\lambda}{8\beta^2}\right), \quad F_\theta \equiv 0. \tag{13}$$

Similarly to Eqs. (13), the force power density N induced by stress σ_{rr} and $\sigma_{r\theta}$ is calculated as

$$N = \int_{-\beta}^{\beta} r\sigma_{rr}v_r d\theta$$
$$= \frac{\rho Q^3}{r^2\mathrm{Re}}\left(\frac{\lambda}{2(2\beta)^3} - \frac{4}{\mathrm{Re}}\left(V'\Big|_{-\beta}^{\beta} + 4 - \frac{\lambda}{(2\beta)^2}\right)\right). \tag{14}$$

By means of Eqs. (12)–(14), the desired parameters of the steady flow of the viscous fluid in the plane diffuser are expressed in terms of the initial dimensional and dimensionless physical parameters. For Q = const, the force characteristics are singular for $\mathrm{Re} \to 0$, or $\mu \to \infty$. The local and integral properties of radial flows in the diffuser are analyzed by using Eqs. (12)–(14).

ACKNOWLEDGMENTS

This work was supported by the Russian Foundation for Basic Research (project nos. 02-01-00252, 02-01-00157, and 03-01-96539) and the Council of the President of the Russian Federation for Support of Young Russian Scientists and Leading Scientific Schools (project nos. NSh-1627.2003.1 and MK-2093.2003.1).

REFERENCES

1. G. B. Jeffery, Philos. Mag. **29** (172), 455 (1915).
2. G. Hamel, Jahresber. Dtsch. Math. Ver. **25**, 34 (1917).
3. N. E. Kochin, I. A. Kibel', and N. V. Roze, *Theoretical Hydromechanics* (Fizmatgiz, Moscow, 1963), Chap. 2.
4. L. D. Akulenko, D. V. Georgievskiĭ, and S. A. Kumakshev, Dokl. Akad. Nauk **383**, 46 (2002) [Dokl. Phys. **47**, 219 (2002)].
5. L. D. Akulenko, D. V. Georgievskiĭ, and S. A. Kumakshev, Izv. Ross. Akad. Nauk, Mekh. Zhidk. Gaza, No. 1, 15 (2004).
6. G. K. Batchelor, *An Introduction to Fluid Dynamics* (Cambridge University Press, Cambridge, 1967; Mir, Moscow, 1973).
7. K. Millsaps and K. Pohlhausen, J. Aeronaut. Sci. **2**, 187 (1953).
8. L. D. Akulenko, S. A. Kumakshev, and S. V. Nesterov, Prikl. Mat. Mekh. **66**, 723 (2002).

Translated by R. Tyapaev

Doklady Physics, Vol. 49, No. 6, 2004, pp. 366–368. Translated from Doklady Akademii Nauk, Vol. 396, No. 4, 2004, pp. 485–487.

MECHANICS

On the First Integrals of the Problem of Jumping a Massive Rigid Body on a Smooth Horizontal Plane

A. A. Burov* and D. P. Chevallier**

Presented by Academician V.V. Rumyantsev January 12, 2004

Received January 22, 2004

The problem of moving a massive rigid body on a smooth horizontal plane is considered. We formulate the existence conditions for the first integrals, which are satisfied in the free flight of the body, as well as upon its contact with the plane.

The existence of the first integrals of the problem of continuously moving a massive rigid body on smooth horizontal rigid [1, 2] and deformable [3] planes has been analyzed. Powerful methods of studying the existence conditions for the first integrals in the dynamics of rigid bodies under unilateral constraints have been proposed in [5, 6].

FORMULATION OF THE PROBLEM

We consider a massive rigid body moving on a smooth horizontal plane π. Let $\mathbb{O}X_\alpha X_\beta X_\gamma$ be an absolute coordinate system whose $\mathbb{O}X_\alpha$ and $\mathbb{O}X_\beta$ axes lie in the plane, $\mathbb{O}X_\gamma$ axis is directed upward, and $\mathbb{O} \in \pi$. The axes of the moving coordinate system $\mathscr{C}x_1x_2x_3$ coincide with the principal central axes of inertia of the body.

Since the plane π is assumed smooth, there are no forces acting on the body along the plane and the momentum projection on the plane is conserved. Hence, without loss of generality, we assume that the body's center of mass moves vertically. In this case, the kinetic and potential energies of the system are given by the expressions

$$T = T_V + T_\omega = \frac{1}{2}mV_\gamma^2 + \frac{1}{2}(\mathbf{I}\boldsymbol{\omega}, \boldsymbol{\omega}),$$

$$U = mgX_\gamma, \quad X_\gamma = (\mathbf{r}, \boldsymbol{\gamma}).$$

Here, m is the body's mass, $\mathbf{I} = \mathrm{diag}(I_1, I_2, I_3)$ is the principal central tensor of inertia, V_γ is the vertical component of the center-of-mass velocity, $\boldsymbol{\omega} = (\omega_1, \omega_2, \omega_3)$ is the angular velocity vector, $\mathbf{r} = (r_1, r_2, r_3)$ is the $\overrightarrow{\mathbb{O}\mathscr{C}}$ vector, g is the gravitational acceleration, $\boldsymbol{\gamma} = (\gamma_1, \gamma_2, \gamma_3)$ is the upward unit vector, and X_γ is the distance from the body's center of mass to the plane π.

EQUATIONS OF MOTION ABOVE THE PLANE AND THEIR FIRST INTEGRALS

The free flight of the body is described by the dynamical equations for its angular momentum and momentum,

$$\mathbf{I}\dot{\boldsymbol{\omega}} = \mathbf{I}\boldsymbol{\omega} \times \boldsymbol{\omega}, \quad \dot{V}_\gamma = -g, \tag{1}$$

and by the kinematic relations

$$\dot{X}_\gamma = V_\gamma, \quad \dot{\boldsymbol{\gamma}} = \boldsymbol{\gamma} \times \boldsymbol{\omega}. \tag{2}$$

In this case, the translational and rotational variables of the problem are completely separated, and these equations are completely integrable. The conserved integrals

$$\mathscr{J}_\omega = T_\omega \text{ and } \mathscr{J}_V = T_V + U$$

represent the kinetic rotational energy and total translational energy, respectively.

The angular momentum vector of the body's free flight remains constant in the absolute coordinate system. Hence, the vertical component $\mathscr{J}_\gamma = (\mathbf{I}\boldsymbol{\omega}, \boldsymbol{\gamma})$ and magnitude squared $\mathscr{J} = (\mathbf{I}\boldsymbol{\omega}, \mathbf{I}\boldsymbol{\omega})$ of the angular momentum are also constant. Since the vector $\boldsymbol{\gamma}$ is a unit vector, $\mathscr{J}_e = (\boldsymbol{\gamma}, \boldsymbol{\gamma}) - 1 = 0$.

EQUATIONS OF THE BODY'S CONTACT WITH THE PLANE

We now assume that the body comes in contact with the plane π at a point $\mathscr{K}$. Let $\mathbf{x}$ be the vector $\overrightarrow{\mathscr{C}\mathscr{K}}$. If the

* *Computer Center, Russian Academy of Sciences, ul. Vavilova 40, GSP-1, Moscow, 117967 Russia*

** *Ecole Nationale des Ponts et Chaussées, 6 et 8 avenue Blaise Pascal, Cité Descartes, Champs-sur-Marne, F-77455 Marne-la-Vallee cedex 2, France*

1028-3358/04/4906-0366$26.00 © 2004 MAIK "Nauka/Interperiodica"

equation $f(\mathbf{x}) = 0$ describes the body surface in the moving coordinate system, then the dependence $\mathbf{x} = \mathbf{x}(\boldsymbol{\gamma})$ can be found from the expression

$$\boldsymbol{\gamma} = -\frac{\partial f}{\partial \mathbf{x}}\left|\frac{\partial f}{\partial \mathbf{x}}\right|^{-1}$$

for the vector $\boldsymbol{\gamma}$ collinear to the normal to the body's surface at the point X [7, 8]. In this case, as is known,

$$\frac{\partial(\mathbf{x}(\boldsymbol{\gamma}), \boldsymbol{\gamma})}{\partial \boldsymbol{\gamma}} = \mathbf{x}(\boldsymbol{\gamma}).$$

We assume that the body's interaction with the plane is lossless. According to [8], the coordinates of the body do not change upon its contact with the plane, while the transformation $(V_\gamma, \boldsymbol{\omega}) \to (V'_\omega, \boldsymbol{\omega}')$ of its center-of-mass velocity and its angular velocity at this time are determined by the equations

$$\mathbf{I}(\boldsymbol{\omega}' - \boldsymbol{\omega}) = R\mathbf{x} \times \boldsymbol{\gamma}, \quad m(V'_\gamma - V_\gamma) = R. \tag{3}$$

Statement 1. *The quantities*

$$\mathcal{J}_\mathbf{x} = (\mathbf{I}\boldsymbol{\omega}, \mathbf{x}), \quad \mathcal{J}_\gamma = (\mathbf{I}\boldsymbol{\omega}, \boldsymbol{\gamma}) \tag{4}$$

are conserved upon the impact.

The proof reduces to the scalar multiplication of the left and right sides of the first equality of Eqs. (3) by the vectors $\mathbf{x}$ and $\boldsymbol{\gamma}$, respectively.

Therefore, the vertical component of the angular momentum is conserved upon the impact, as well as in the course of continuous motion, i.e., for the total time of motion.

DETERMINATION OF THE REACTIONS

Since the potential energy depends only on the body position, which does not change at the impact time, the quantity R can be found from the condition of kinetic-energy conservation:

$$(\mathbf{I}\boldsymbol{\omega}', \boldsymbol{\omega}') + mV'^2_\gamma = (\mathbf{I}\boldsymbol{\omega}, \boldsymbol{\omega}) + mV^2_\gamma. \tag{5}$$

Performing the scalar multiplication of Eqs. (3) by $\boldsymbol{\omega}' + \boldsymbol{\omega}$ and Eq. (5) by $V'_\gamma + V_\gamma$, summing the results, and taking Eq. (5) into account, we arrive at the equation

$$\begin{aligned}&(\mathbf{I}\boldsymbol{\omega}', \boldsymbol{\omega}') + mV'^2_\gamma - (\mathbf{I}\boldsymbol{\omega}, \boldsymbol{\omega}) - mV^2_\gamma \\ &= R[(\boldsymbol{\omega}' + \boldsymbol{\omega}, \mathbf{x} \times \boldsymbol{\gamma}) + (V'_\gamma + V_\gamma)] = 0.\end{aligned} \tag{6}$$

The quantities $\boldsymbol{\omega}'$ and V'_γ are found from Eqs. (3):

$$\boldsymbol{\omega}' = \boldsymbol{\omega} + R \cdot \mathbf{I}^{-1}(\mathbf{x} \times \boldsymbol{\gamma}), \quad V'_\gamma = V_\gamma + R. \tag{7}$$

Substituting expressions (7) into Eq. (5), we arrive at the equality

$$(2\boldsymbol{\omega} + R \cdot (\mathbf{I}^{-1}(\mathbf{x} \times \gamma), \mathbf{x} \times \boldsymbol{\gamma})) + 2V_\gamma + m^{-1}R = 0$$

from which the nonzero root of Eqs. (5) is found in the form

$$R = -2\frac{V_\gamma + (\boldsymbol{\omega}, \mathbf{x} \times \boldsymbol{\gamma})}{m^{-1} + (\mathbf{I}^{-1}(\mathbf{x} \times \boldsymbol{\gamma}), \mathbf{x} \times \boldsymbol{\gamma})}. \tag{8}$$

DYNAMICALLY SYMMETRIC CASE

We consider an axisymmetric body whose symmetry axis coincides with the $\mathcal{C}x_3$ axis. In this case, the surface is described by the equation

$$f(\rho, x_3) = 0, \quad \rho = (x_1^2 + x_2^2)^{1/2}. \tag{9}$$

The differentiation of Eq. (9) with respect to x_1 and x_2 yields

$$\gamma_i = -\frac{\partial f}{\partial \rho}\frac{x_i}{\rho}\left|\frac{\partial f}{\partial \mathbf{x}}\right|^{-1}, \quad i = 1, 2.$$

We also assume that the condition $I_1 = I_2$ is satisfied. In this case, by virtue of relation (3), we have

$$\omega'_3 = \omega_3.$$

Therefore, all first integrals are conserved even if a unilateral constraint is imposed.

AN ANALOGUE OF THE HESS–APPELROT CASE

Let $I_1 > I_2 > I_3$. As is known, if

$$\mathbf{a} = (a_1, a_2, a_3):$$

$$a_1 = \sqrt{I_2^{-1} - I_1^{-1}}, \quad a_2 = 0, \text{ and } a_3 = \sqrt{I_3^{-1} - I_2^{-1}},$$

then the equations of free motion have the particular integrals (invariant relations)

$$\mathcal{F}_\varepsilon = a_1 I_1 \omega_1 + \varepsilon a_3 I_3 \omega_3 = 0, \quad \varepsilon = \pm 1. \tag{10}$$

According to Eqs. (3), these relations hold for the body–plane contact if the conditions

$$a_1\left(x_3\frac{\partial f}{\partial x_2} - x_2\frac{\partial f}{\partial x_3}\right) + \varepsilon a_3\left(x_2\frac{\partial f}{\partial x_1} - x_1\frac{\partial f}{\partial x_2}\right) = 0 \tag{11}$$

are satisfied (see [1]). Treating relations (11) as linear partial differential equations, we find their solution in the form

$$\begin{aligned}&\mathcal{F} = \mathbf{F}(u, v) = 0, \quad u = b_1 x_1 + \varepsilon b_3 x_3, \\ &v = (-\varepsilon b_3 x_1 + b_1 x_3)^2 + x_2^2,\end{aligned} \tag{12}$$

$$b_1 = \sqrt{\frac{I_2^{-1} - I_1^{-1}}{I_3^{-1} - I_1^{-1}}}, \quad b_2 = 0, \quad b_3 = \sqrt{\frac{I_3^{-1} - I_2^{-1}}{I_3^{-1} - I_1^{-1}}}.$$

Remark. A similar solution holds in the case of a body moving between two parallel horizontal planes π_1 and π_2.

MASSIVE GYROSCOPE

The results obtained above for the integrals of motion of a massive rigid body jumping on a plane can be extended for a massive gyroscope. In this case, instead of Eqs. (2), we consider the equations

$$\mathbf{I}\dot{\boldsymbol{\omega}} = (\mathbf{I}\boldsymbol{\omega} + \mathbf{k}) \times \boldsymbol{\omega}, \quad \dot{\boldsymbol{\gamma}} = \boldsymbol{\gamma} \times \boldsymbol{\omega}, \tag{13}$$

where $\mathbf{k} = (k_1, k_2, k_3)$ is the constant gyroscopic moment of the body. In this case, the variables are also separated, the energy integrals and the geometrical integral have the above form, while the vertical component of the angular momentum takes the form

$$\mathcal{J}_\gamma = (\mathbf{I}\boldsymbol{\omega} + \mathbf{k}, \boldsymbol{\gamma}). \tag{14}$$

The relations describing the impact and the expression for the quantity R obtained above remain valid.

Statement 2. *The quantities*

$$\mathcal{J}_x = (\mathbf{I}\boldsymbol{\omega} + \mathbf{k}, \mathbf{x}), \quad \mathcal{J}_\gamma = (\mathbf{I}\boldsymbol{\omega} + \mathbf{k}, \boldsymbol{\gamma}) \tag{15}$$

are conserved upon the impact.

To prove the statement, we rewrite relation (3) in the form

$$(\mathbf{I}\boldsymbol{\omega}' + \mathbf{k}) - (\mathbf{I}\boldsymbol{\omega} + \mathbf{k}) = R\mathbf{x} \times \boldsymbol{\gamma} \tag{16}$$

and multiply the left and right sides of equality (16) by the vectors $\mathbf{x}$ and $\boldsymbol{\gamma}$, respectively.

Therefore, the vertical component of the angular momentum is conserved upon the impact as well as in the course of continuous motion, i.e., for the total time of motion.

Using arguments similar to those presented above, one can prove that this mapping in the dynamically symmetric case conserves one more integral $\omega_3' = \omega_3$ under the additional condition $\mathbf{k} = (0, 0, k_3)$. If the conditions

$$k_2 = 0$$

and $$\delta I_2 \sqrt{(I_2^{-1} - I_1^{-1})(I_3^{-1} - I_2^{-1})} = \sqrt{I_2^{-1} - I_3^{-1}}\, k_1 - \varepsilon \sqrt{I_2^{-1} - I_1^{-1}}\, k_3,$$

supplementing conditions (12) are satisfied, then mapping (5) conserves the Sretenskiĭ integral [9]

$$\mathcal{F}_\varepsilon = a_1 I_1 \omega_1 + \varepsilon a_3 I_3 \omega_3 + \delta = 0, \tag{17}$$

which similar to the Hess–Appelrot integral.

ACKNOWLEDGMENTS

This work was supported by the Russian Foundation for Basic Research (project no. 02-01-00196) and by the Ministry of Education of the Russian Federation (Federal Program “Integratsiya”).

REFERENCES

1. A. A. Burov, *Problems of Studying the Stability and Stabilization of Motion* (Vych. Tsentr Akad. Nauk SSSR, Moscow, 1985), pp. 118–121.
2. A. A. Burov, *Problems of Studying the Stability and Stabilization of Motion* (Vych. Tsentr Akad. Nauk SSSR, Moscow, 1985), pp. 107–115.
3. A. A. Bourov and D. P. Chevallier, Cahiers du CERMA, No. 13, 17 (1994).
4. T. V. Kozlova, Vestn. Mosk. Univ., Ser. 1: Mat., Mekh., No. 3, 69 (2001).
5. T. V. Kozlova, J. Phys. A **34**, 2121 (2001).
6. A. P. Markeev, *Dynamics of a Body in Contact with a Solid Surface* (Nauka, Moscow, 1992).
7. A. V. Karapetyan, *Stability of Stationary Motion* (URSS, Moscow, 1998).
8. E. J. Routh, *The Elementary Part of a Treatise on the Dynamics of a System of Rigid Bodies*, 6th ed. (Macmillan, London, 1897; Nauka, Moscow, 1983), Vol. 1.
9. L. N. Sretenskiĭ, Vestn. Mosk. Univ., Ser. 1: Mat., Mekh., No. 3, 60 (1963).

Translated by V. Chechin

Doklady Physics, Vol. 49, No. 6, 2004, pp. 369–373. Translated from Doklady Akademii Nauk, Vol. 396, No. 4, 2004, pp. 488–491.

MECHANICS

Problem of Accumulation of Periodic Disturbances in a Periodically Nonstationary Quasi-Harmonic System

M. Ya. Izrailovich

Presented by Academician K.V. Frolov January 14, 2004

Received February 4, 2004

The generalization of the classical Bulgakov problem to the case of steady periodic regimes was first given in [1] for a one-dimensional linear stationary system. For linear stationary systems of arbitrary structure, the solution was presented in [2] on the basis of the construction of Green's functions (pulse-frequency characteristics) for steady periodic regimes. In the case of periodically nonstationary systems, the corresponding generalization was given in [3]. At the same time, for both stationary and periodically nonstationary systems, it is important to estimate the limiting oscillation intensity not only in a steady regime but also in the process of its establishment, because the oscillation intensity is maximal in this process (with the exception of the exact-resonance case). For linear stationary systems, such solutions were obtained on the basis of the construction of a sequence of Green's functions characterizing the establishment process [4, 5]. The corresponding generalization for systems with periodically unsteady piecewise-constant parameters was given in [6]. It should be noted that the derivation of the estimates for periodically nonstationary systems requires very cumbersome calculations both for steady regimes and, the more so, for the process of their establishment. At the same time, the efficiency of approximate methods for analyzing periodic nonstationary systems is well known [7].

In this paper, the problem of disturbance accumulation in a one-dimensional periodically nonstationary quasi-harmonic system is approximately solved under the conditions of the main parametric resonance. The solution is obtained in the closed form for both the steady regime and the process of its establishment.

STEADY REGIME

We will consider a one-dimensional system with periodically varying stiffness

$$\ddot{x} + \varepsilon \cdot 2k\dot{x} + \omega_0^2(1 - \varepsilon h\cos 2t)x = \varepsilon u(t), \qquad (1)$$

where ε is a small parameter, $u(t) = u(t + 2\pi)$ is an external periodic disturbing force limited in amplitude $|u| \le U$, and $h > 0$. It is assumed that the quantity $1 - \omega_0^2$ is of the order of ε. Equation (1) is transformed to the form

$$\ddot{x} + x = \varepsilon(-2k\dot{x} + \omega_0^2 h\cos 2tx + \mu x), \qquad (2)$$

where $\mu = \dfrac{1 - \omega_0^2}{\varepsilon}$.

It is necessary to estimate the maximum amplitude $\bar{x}$ of steady oscillations. Since system (2) is quasi-harmonic, the first approximation of the asymptotic method [7] (with an accuracy to ε^2) is determined in the form

$$x(t) = a(t)\cos t + b(t)\sin t. \qquad (3)$$

Substituting (3) in Eq. (2) and averaging with respect to explicitly entering time, we obtain the following equations for the slowly varying functions $a(t)$ and $b(t)$:

$$\begin{aligned}\dot{a} &= \varepsilon\left[-ka + \left(\frac{\omega_0^2 h}{2} - \frac{1}{2}\mu\right)b - \frac{1}{2\pi}\int_0^{2\pi}\sin\tau u(\tau)d\tau\right],\\ \dot{b} &= \varepsilon\left[\left(\frac{\omega_0^2 h}{2} + \frac{1}{2}\mu\right)a - kb + \frac{1}{2\pi}\int_0^{2\pi}\cos\tau u(\tau)d\tau\right].\end{aligned} \qquad (4)$$

The steady regime is associated with $\dot{a} = 0$ and $\dot{b} = 0$. As a result, Eqs. (4) are reduced to a system of two linear algebraic equations for a and b. Under the condition that

$$\Delta = k^2 + \frac{1}{4}\mu^2 - \left(\frac{\omega_0^2 h}{4}\right)^2 \neq 0,$$

Institute of Mechanical Engineering, Russian Academy of Sciences, ul. Bardina 4, Moscow, 117334 Russia

1028-3358/04/4906-0369$26.00 © 2004 MAIK "Nauka/Interperiodica"

its solution takes the form

$$a = -\frac{1}{2\pi\Delta}\int_0^{2\pi}(\alpha\cos\tau + ks\sin\tau)u(\tau)d\tau,$$
$$b = \frac{1}{2\pi\Delta}\int_0^{2\pi}(k\sin\tau - \beta\cos\tau)u(\tau)d\tau, \quad (5)$$

where

$$\alpha = \frac{1}{2}\mu - \frac{\omega_0^2 h}{4}, \quad \beta = \frac{1}{2}\mu + \frac{\omega_0^2 h}{4}.$$

From Eqs. (3) and (5), we determine the stationary solution in the form

$$x(t) = \frac{1}{2\pi\Delta}\int_0^{2\pi}[(k\sin t - \alpha\cos t)\cos\tau$$
$$-(k\cos t + \beta\sin t)\sin\tau]u(\tau)d\tau$$
$$= \frac{1}{2\pi\Delta}A_0(t)\int_0^{2\pi}\cos[\tau + \psi_0(t)]u(\tau)d\tau, \quad (6)$$

where

$$A_0(t) = \left[\frac{1}{4}\mu^2 + k^2 + \left(\frac{\omega_0^2 h}{4}\right)^2 + k\frac{\omega_0^2 h}{2}\sin 2t - \frac{1}{4}\omega_0^2 h\mu\cos 2t\right]^{\frac{1}{2}}, \quad (7)$$

$$\psi_0(t) = \arccos\left[\frac{k\sin t - \alpha\cos t}{A_0(t)}\right]. \quad (8)$$

From Eq. (6), the maximum steady oscillation amplitude is directly estimated as

$$\bar{x} = \max_{t\in[0;2\pi)}\frac{A_0(t)U}{2\pi\Delta}\int_0^{2\pi}|\cos[\tau + \psi_0(t)]|d\tau. \quad (9)$$

Since

$$\int_0^{2\pi}|\cos[\tau + \psi_0(t)]|d\tau = 4$$

for each $\psi_0(t)$, the maximum value of the function $A_0(t)$ is

$$\max_{t\in[0;2\pi)}A_0(t) = \left[\frac{1}{4}\mu^2 + k^2 + \left(\frac{\omega_0^2 h}{4}\right)^2 + 2\frac{\omega_0^2 h}{4}\sqrt{\frac{1}{4}\mu^2 + k^2}\right]^{\frac{1}{2}} = \sqrt{\frac{1}{4}\mu^2 + k^2} + \frac{\omega_0^2 h}{4}. \quad (10)$$

According to Eqs. (9) and (10),

$$\bar{x} = \frac{1}{\pi}\frac{U}{\sqrt{\mu^2 + 4k^2} - \frac{\omega_0^2 h}{2}} \quad (11)$$

for

$$\frac{\omega_0^2 h}{2} < \sqrt{\mu^2 + 4k^2}.$$

PROCESS OF ESTABLISHMENT OF THE PERIODIC REGIME

For the process of establishment of the periodic regime, the functions $a(t)$ and $b(t)$ are determined from the system of linear differential equations (4). For zero initial conditions, the solution of this system takes the form

$$a(t) = -\frac{1}{2\pi\Delta}\left\{[k + e^{-\varepsilon kt}(\gamma\sin\varepsilon\gamma t - k\cos\varepsilon\gamma t)]\right.$$
$$\times\int_0^{2\pi}\sin\tau u(\tau)d\tau + \sqrt{\frac{\alpha}{\beta}}[\gamma - e^{-\varepsilon kt}(k\sin\varepsilon\gamma t + \gamma\cos\varepsilon\gamma t)]$$
$$\left.\times\int_0^{2\pi}\cos\tau u(\tau)d\tau\right\},$$
$$b(t) = \frac{1}{2\pi\Delta}\left\{[k + e^{-\varepsilon kt}(\gamma\sin\varepsilon\gamma t - k\cos\varepsilon\gamma t)]\right. \quad (12)$$
$$\times\int_0^{2\pi}\cos\tau u(\tau)d\tau - \sqrt{\frac{\beta}{\alpha}}[\gamma - e^{-\varepsilon kt}(k\sin\varepsilon\gamma t + \gamma\cos\varepsilon\gamma t)]$$
$$\left.\times\int_0^{2\pi}\sin\tau u(\tau)d\tau\right\},$$

where $\gamma = \sqrt{\alpha\beta}$.

Substituting Eqs. (12) into expression (3), we determine the following law $x(t)$ of establishment of the periodic regime:

$$x(t) = \frac{1}{2\pi\Delta}\left\{[k - e^{-\varepsilon kt}(\gamma\sin\varepsilon\gamma t - k\cos\varepsilon\gamma t)]\sin t\right.$$

$$\left. - \sqrt{\frac{\alpha}{\beta}}[\gamma - e^{-\varepsilon kt}(k\sin\varepsilon\gamma t + \gamma\cos\varepsilon\gamma t)]\cos t\right\}$$

$$\times \int_0^{2\pi} \cos\tau u(\tau)d\tau$$

$$- \frac{1}{2\pi\Delta}\left\{[k + e^{-\varepsilon kt}(\gamma\sin\varepsilon\gamma t - k\cos\varepsilon\gamma t)]\cos t\right.$$

$$\left. + \sqrt{\frac{\alpha}{\beta}}[\gamma - e^{-\varepsilon kt}(k\sin\varepsilon\gamma t + \gamma\cos\varepsilon\gamma t)]\sin t\right\}$$

$$\times \int_0^{2\pi} \sin\tau u(\tau)d\tau. \quad (13)$$

Similar to the case of the steady periodic regime, expression (13) is transformed to the form

$$x(t) = \frac{1}{2\pi\Delta}A(t)\int_0^{2\pi}\cos[\tau + \psi(t)]u(\tau)d\tau, \quad (14)$$

where

$$A(t) = \left\{[k + e^{-\varepsilon kt}(\gamma\sin\varepsilon\gamma t - k\cos\varepsilon\gamma t)]^2\right.$$

$$+ \frac{1}{2}\frac{\beta - \alpha}{\gamma}[k + e^{-\varepsilon kt}(\gamma\sin\varepsilon\gamma t - k\cos\varepsilon\gamma t)]$$

$$\times [\gamma - e^{-\varepsilon kt}(k\sin(\varepsilon\gamma t + \gamma\cos\varepsilon\gamma t))]\sin 2t$$

$$\left. + [\gamma - e^{-\varepsilon kt}(k\sin\varepsilon\gamma t + \gamma\cos\varepsilon\gamma t)]^2\left(\frac{\beta}{\alpha}\sin^2 t + \frac{\alpha}{\beta}\cos^2 t\right)\right\}^{\frac{1}{2}}, \quad (15)$$

$$\psi(t) = \arccos\left\{A^{-1}(t)[k + e^{-\varepsilon kt}(\gamma\sin\varepsilon\gamma t - k\cos\varepsilon\gamma t)]\right.$$

$$\times \sin t - A^{-1}(t)\sqrt{\frac{\alpha}{\beta}}$$

$$\left. \times [\gamma - e^{-\varepsilon kt}(k\sin\varepsilon\gamma t + \gamma\cos\varepsilon\gamma t)]\right\}. \quad (16)$$

Since

$$\int_0^{2\pi}|\cos[\tau + \psi(t)]|d\tau = 4,$$

Eq. (14) yields the following solution of the problem of disturbance accumulation in the process of establishment of the periodic regime:

$$\bar{x}(t) = \frac{2A(t)}{\pi\Delta}U. \quad (17)$$

THE CASE OF A STATIONARY SYSTEM

The solutions obtained above can also be used in the case of the absence of parametric excitation, because the corresponding exact formulas have a considerably more cumbersome structure. In the case of a steady regime, Eq. (11) yields

$$\bar{x} = \frac{4}{\pi}\frac{U}{\sqrt{\mu^2 + 4k^2}}. \quad (18)$$

The exact estimate for system (1) at $\varepsilon = 1$ and $h = 0$ is determined from the formula [5]

$$\bar{x}^* = \frac{\tilde{A}}{\omega_0^2}\left\{k\sin\tilde{\psi} + \omega\cos\tilde{\psi} + 2e^{k\frac{\tilde{\psi}}{\omega}}\omega\left(1 - e^{-k\frac{\pi}{\omega}}\right)^{-1}\right.$$

$$\times\left[e^{-k\frac{\pi}{\omega}} - e^{-k\frac{\pi}{\omega}(n+1)}\right] + (-1)^{n+1}e^{-2k\pi}[k\sin(2\pi\omega + \tilde{\psi})$$

$$\left. + \omega\cos(2\pi\omega + \tilde{\psi})]\right\}U, \quad (19)$$

$$\omega \in \left(\frac{n}{2} - \frac{\tilde{\psi}}{2\pi}; \frac{n+1}{2} - \frac{\tilde{\psi}}{2\pi}\right), \quad n = 1, 2, \ldots,$$

where

$$\tilde{A} = [\omega(1 + e^{-4k\pi} - 2e^{-2k\pi}\cos 2\pi\omega)]^{-1},$$

$$\tilde{\psi} = \arccos[\omega A(1 - e^{-2k\pi}\cos 2\pi\omega)],$$

$$\omega = \sqrt{\omega_0^2 - k^2}.$$

Figure 1 shows the ω_0 dependences of $\frac{\bar{x}}{U}$ given by (18) and $\frac{\bar{x}^*}{U}$ given by (19) for $\varepsilon = 1$.

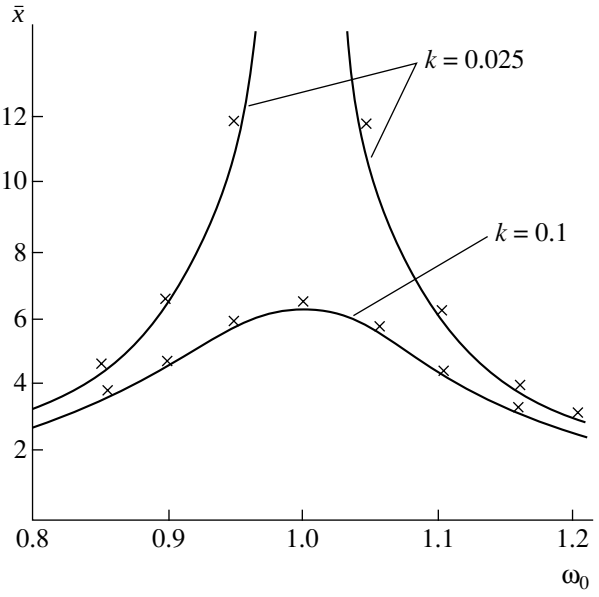

Fig. 1. (Lines) Approximate and (points) exact estimates of the maximum amplitude of steady oscillations vs. the natural frequency ω_0 for a stationary system at $U = 1$.

For the course of establishment of the periodic regime, expression (17) at $h = 0$ takes the form

$$\bar{x}(t) = \frac{4}{\pi}\frac{(1 - 2e^{-\varepsilon kt}\cos\varepsilon\gamma t + e^{-2\varepsilon kt})^{\frac{1}{2}}}{\sqrt{\mu^2 + 4k^2}}U. \qquad (20)$$

According to Eq. (20), the upper and lower envelopes of the oscillating curve $\bar{x}(t)$ have the form

$$\bar{x}_{\pm}(t) = \frac{4}{\pi}\frac{1 \pm e^{-\varepsilon kt}}{\sqrt{\mu^2 + 4k^2}}U. \qquad (21)$$

The corresponding lines are given in Fig. 2.

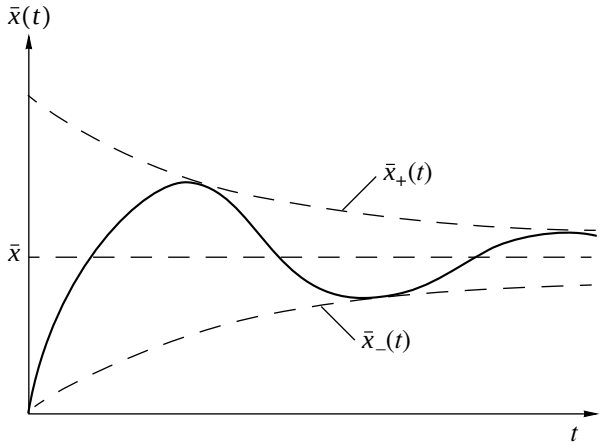

Fig. 2. Estimates of the maximum oscillation amplitude for a linear stationary system for the process of establishment of the periodic regime.

The exact expression for the estimate $\bar{x}^*(t)$ for the process of establishment of the periodic regime, which is derived in the closed form by constructing a sequence of Green's functions [5, 6], has a very cumbersome structure. It can be simplified only in the case of the "exact resonance" $\omega_0 = 1$. In this case,

$$\bar{x}^*(t) = \frac{1}{\omega}\int_0^t e^{-k\tau}|\sin\omega\tau|d\tau U$$

$$= \frac{1}{\omega}\Big[\omega + 2\omega\left(1 - e^{-k\frac{\pi}{\omega}}\right)^{-1}\left(e^{k\frac{\pi}{\omega}} - e^{-k\frac{\pi}{\omega}(n+1)}\right)$$

$$+ e^{-kt}(-1)^{n+1}(k\sin\omega t + \omega\cos\omega t)\Big]U, \quad \omega = \sqrt{1 - k^2}, \qquad (22)$$

$$t \in \left(\frac{n\pi}{\omega}, \frac{(n+1)\pi}{\omega}\right), \quad n = 1, 2, \ldots .$$

Approximate solution (20) for this case takes the form

$$\bar{x}(t) = \frac{2}{\pi k}(1 - e^{-\varepsilon kt})U. \qquad (23)$$

The disturbance accumulation curves given by Eqs. (22) and (23) are monotonically increasing and correspond to the classical Bulgakov problem on the disturbance accumulation [in the absence of the periodicity condition imposed on $u(t)$]. Figure 3 shows the curves $\bar{x}(t)$ (for $\varepsilon = 1$) and $\bar{x}^*(t)$.

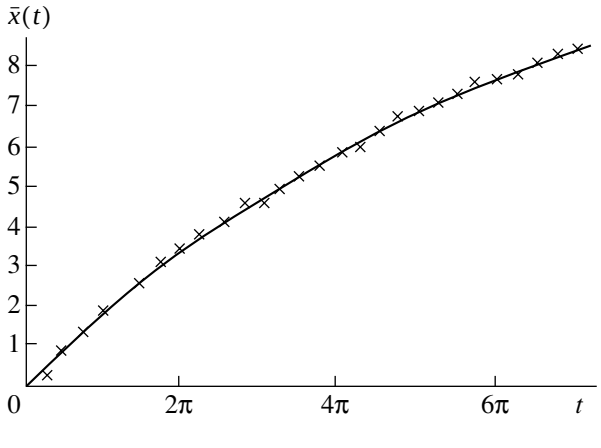

Fig. 3. (Points) Exact and (line) approximate estimates of the disturbance accumulation for a linear stationary system at $\omega_0 = 1$, $k = 0$, and $U = 1$.

REFERENCES

1. V. A. Troitskiĭ, Inzh. Zh. Mekh. Tverd. Tela, No. 5, 22 (1966).
2. E. N. Rozenvasser, *Oscillations of Nonlinear Systems: Method of Integral Equations* (Nauka, Moscow, 1969).
3. E. N. Rozenvasser, *Periodic Nonstationary Control Systems* (Nauka, Moscow, 1973).
4. M. Ya. Izrailovich, Mashinovedenie, No. 1, 34 (1976).
5. M. Ya. Izrailovich, Probl. Mashinostr. Nadezhnosti Mashin., No. 6, 22 (1996).
6. M. Ya. Izrailovich, Mashinovedenie, No. 4, 34 (1977).
7. N. N. Bogolyubov and Yu. A. Mitropol'skii, *Asymptotic Methods in the Theory of Nonlinear Oscillations* (Nauka, Moscow, 1974; Gordon and Breach, New York, 1962).

Translated by M. Lebedev

Doklady Physics, Vol. 49, No. 6, 2004, pp. 374–377. Translated from Doklady Akademii Nauk, Vol. 396, No. 4, 2004, pp. 492–495.

MECHANICS

Consistent Variant of Continuum Deformation Theory in the Quadratic Approximation

V. N. Paĭmushin* and V. I. Shalashilin**

Presented by Academician I.F. Obraztsov December 25, 2003

Received December 30, 2003

The complete (see, e.g., [1]) and incomplete (see, e.g., [2, 3]) variants of the nonlinear theory of continuum deformations are analyzed in the quadratic approximation. It is shown that the complete-variant relationships determining tensile strains and incomplete-variant relationships determining shear strains are incorrect, because they yield spurious bifurcation points in particular problems. For small tensile strains and intermediate shear strains, a consistent variant of kinematic relationships in the quadratic approximation is constructed as a combination of the relationships of the complete and incomplete variants.

1. QUADRATIC-APPROXIMATION RELATIONSHIPS OF DEFORMATION THEORY

Let (x, y, z) be rectangular Cartesian coordinates of a body in its initial (undeformed) state and (u, v, w) be the displacement components. Then, for arbitrary displacements, the tensile strains E_x, E_y, and E_z and shear strains $\sin\gamma_{xy}$, $\sin\gamma_{xz}$, and $\sin\gamma_{yz}$ obey the formulas

$$E_x = \sqrt{1 + 2\varepsilon_{xx}} - 1, \ldots, \tag{1.1}$$

$$\sin\gamma_{xy} = (1 + 2\varepsilon_{xx})^{-1/2}(1 + 2\varepsilon_{yy})^{-1/2}\varepsilon_{xy}, \ldots. \tag{1.2}$$

These formulas, along with six strain components

$$\varepsilon_{xx} = u_{,x} + \frac{1}{2}(u_{,x}^2 + v_{,x}^2 + w_{,x}^2), \ldots, \tag{1.3}$$

$$\varepsilon_{xy} = u_{,y} + v_{,x} + u_{,x}u_{,y} + v_{,x}v_{,y} + w_{,x}w_{,y}, \ldots, \tag{1.4}$$

describe an arbitrary deformed state of the body. Formulas (1.1)–(1.4) were derived and analyzed in detail in [1]. At present, they are used in almost any paper concerning nonlinear elasticity theory.

When tensile strains are small, i.e., $E_x \approx \varepsilon \ll 1$, Eqs. (1.1) in the approximation $2 + E_x \approx 2$ yield the relationships

$$E_x \approx \varepsilon_{xx} = u_{,x} + \frac{1}{2}(u_{,x}^2 + v_{,x}^2 + w_{,x}^2), \ldots, \tag{1.5}$$

and Eqs. (1.2) in the approximation $(1 + 2E_x)^{-1/2} \approx 1$ yield

$$\sin\gamma_{xy} \approx \varepsilon_{xy} = u_{,y} + v_{,x} + u_{,x}u_{,y} + v_{,x}v_{,y} + w_{,x}w_{,y}, \ldots. \tag{1.6}$$

For small shear angles γ_{xy}, γ_{xz}, and γ_{yz}, Eqs. (1.6) can be written in the form

$$\gamma_{xy} \approx \varepsilon_{xy} = u_{,y} + v_{,x} + u_{,x}u_{,y} + v_{,x}v_{,y} + w_{,x}w_{,y}, \ldots. \tag{1.7}$$

Formulas (1.5) and (1.7) were derived in [1] and used as the kinematic relationships in the quadratic approximation.

Another incomplete quadratic variant of the kinematic relationships was derived in [2], where $E_x, \ldots$ and $\sin\gamma_{xy}, \ldots$ were calculated up to the squares and pairwise products of derivatives with respect to displacements by the formulas

$$E_x = u_{,x} + \frac{1}{2}(v_{,x}^2 + w_{,x}^2), \ldots, \tag{1.8}$$

$$\sin\gamma_{xy} = u_{,y} + v_{,x} - u_{,x}v_{,x} - u_{,y}v_{,y} + w_{,x}w_{,y}, \ldots. \tag{1.9}$$

A simpler variant of relations (1.9),

$$\gamma_{xy} = u_{,y} + v_{,x} + w_{,x}w_{,y}, \ldots \tag{1.10}$$

was considered in [3].

The necessity of evaluating the quality of the above three variants of the kinematic relationships in the quadratic approximation arose due to the appearance of spurious bifurcation points when solving the particular problems formulated in [4] on the basis of Eq. (1.5). The applicability of these variants to elementary stress–strain states, i.e., for uniaxial tension–compression and simple shear, can be an evaluation criterion.

* *Kazan State Technical University, ul. Karla Marksa 10, Kazan, 420111 Tatarstan, Russia*

** *Moscow State Institute of Aviation, Volokolamskoe sh. 4, Moscow, 125080 Russia*

1028-3358/04/4906-0374$26.00 © 2004 MAIK “Nauka/Interperiodica”

2. UNIAXIAL TENSION–COMPRESSION

For uniaxial tension–compression of a rod by a force P applied to its ends, formulas (1.8) are better than formulas (1.5). Moreover, formulas (1.8) in this case are applicable for any elastic strains. This can be justified as follows.

According to the Novozhilov approach, the variation of work done by the forces applied to an elementary parallelepiped, whose dimensions before deformation were dx, dy, and dz and which was deformed after loading along the x axis, has the form

$$\delta dA = \sigma^*_{xx}\delta\varepsilon_{xx}dxdydz, \tag{2.1}$$

where

$$\sigma^*_{xx} = \frac{S^*_x}{S_x}\frac{\sigma_{xx}}{\sqrt{1+2\varepsilon_{xx}}}, \quad S_x = dydz. \tag{2.2}$$

Then,

$$\delta dA = (\sigma_{xx}S^*_x)\delta(\sqrt{1+2\varepsilon_{xx}}-1)dx = dP_x\delta(E_xdx). \tag{2.3}$$

Here, dP_x is the normal force applied to the $dy\,dz$ face of the element.

Expression $\delta dA = dP_x\delta(E_xdx)$ can be written immediately from the virtual work principle for the deformed element, because $(1+E_x)dx$ is its deformed length. On the other hand, the deformed length of the element has the form

$$dx + \frac{du}{dx}dx = \left(1+\frac{du}{dx}\right)dx.$$

Comparing, we see that

$$E_x = \frac{du}{dx}. \tag{2.4}$$

Expression (1.8) leads to formula (2.4). Since $v_x = w_x \equiv 0$ in the case under consideration, Eq. (2.4) is obtained also by the substitution of Eq. (1.3) into Eq. (1.1):

$$E_x = \sqrt{1+2\varepsilon_{xx}}-1 = \sqrt{1+2u_{,x}+u^2_{,x}}-1 = \frac{du}{dx}.$$

At the same time, approximation (1.5) provides the expression

$$E_x \approx \varepsilon_{xx} = \frac{du}{dx}+\frac{1}{2}\left(\frac{du}{dx}\right)^2, \tag{2.5}$$

the use of which in the problem of the compression of a rod by a force P results in the spurious bifurcation value of $P = EF$ (F is the cross-sectional area) of "absurd" loss of the rod stability [4].

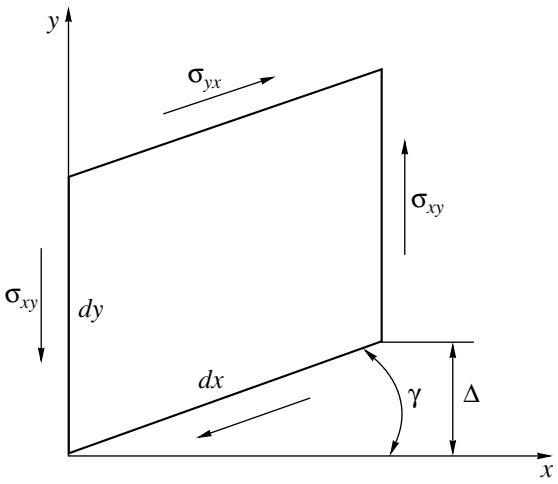

Figure.

3. SIMPLE SHEAR

According to the Novozhilov approach, the work variation for simple shear in the xy plane has the form

$$\delta dA = \sigma^*_{xy}\delta\varepsilon_{xy}dxdydz, \tag{3.1}$$

where

$$\sigma^*_{xy} = \frac{S^*_x}{S_x}\frac{\sigma_{xy}}{1+E_y}, \quad 1+E_y = \sqrt{1+2\varepsilon_{yy}}. \tag{3.2}$$

The figure shows one of the possible positions of the element with respect to the coordinate axes. The other positions are obtained from that shown in the figure by the rotation of the rigid body. For the shown variant, $u = u(x)$ and $v = v(x)$. In this case, the displacements must be such that $E_x = E_y = 0$. They can be easily found in the form

$$v = x\sin\gamma, \quad u = x(\cos\gamma - 1). \tag{3.3}$$

According to Eqs. (3.3), $E_x = E_y = 0$ and $S^*_x = S_x$. In addition, for simple shear, $\sigma_{xx} = \sigma_{yy} = 0$ and $\sigma^*_{xy} = \sigma_{xy}$. As a result, we obtain

$$\delta dA = \sigma_{xy}\delta(\varepsilon_{xy})dxdydz. \tag{3.4}$$

Writing $\delta(dA)$ according to the virtual work principle and taking into account that $\sigma_{xx} = 0$ for simple shear, we obtain $\tau_{xy} = \sigma_{xy}$ and

$$\delta dA = \tau_{xy}dydz\cdot\delta(\Delta) = \sigma_{xy}\delta(dx\sin\gamma)dydz. \tag{3.5}$$

Expression (3.5) coincides with Eq. (3.4) when formula (1.6) is used for ε_{xy}. In this case, $\varepsilon_{xy} = \sin\gamma$ for any γ.

If relations (1.9) are used, then

$$\sin\gamma_{xy} = \sin\gamma - (\cos\gamma - 1)\sin\gamma \approx \sin\gamma + \frac{1}{2}(\sin\gamma)^3. \quad (3.6)$$

This case is similar to the case of compression, where the use of approximation (1.5) leads to the appearance of the spurious bifurcation point in the solution [4].

Thus, the best approximation for elementary states is provided by the combined variant of the kinematic relationships in the quadratic approximation, where tensile and shear strains are calculated by Eqs. (1.8) (according to the Donnell approach) and Eqs. (1.6) (according to the Novozhilov approach), respectively.

Finally, it should be noted that (as is seen in figure) energetically consistent generalized displacement for τ_{xy} is $\sin\gamma = \sin\gamma_{xy}$ rather than $\gamma = \gamma_{xy}$; i.e., the measure of shear strain is $\sin\gamma$ rather than γ. However, this note is related only to the form of representation of Hooke's law for shear strains and to the processing of corresponding experimental data for large shear strains. In other words, for the linearly elastic behavior of a material under considerable shear strains, Hooke's law must be represented in the form $\tau = G\sin\gamma$ (where G is the shear modulus) rather than $\tau = G\gamma$, as is universally used.

With allowance for this note, Eq. (1.10) should be written in the form

$$\sin\gamma_{xy} = u_{,y} + v_{,x} + w_{,x}w_{,y}, \ldots. \quad (3.7)$$

Then, the combined variant of Eqs. (1.8) and (3.7) is also consistent.

4. ANALYSIS OF THE KINEMATIC RELATIONSHIPS IN ORTHOGONAL CURVILINEAR COORDINATES

The undeformed body is considered in an orthogonal curvilinear coordinate system x^α ($\alpha = 1, 2, 3$), where the Lamé parameters H_α and unit vectors $\mathbf{l}_\alpha$ are defined. Let the displacement vector $\mathbf{U}$ of an arbitrary point $M(x^\alpha)$ be represented by a decomposition $\mathbf{U} = U_\alpha\mathbf{l}_\alpha$. Then, the unit vectors $\mathbf{l}_\alpha^*$, as well as tensile E_α and shear $\gamma_{\alpha\beta}$ strains in a deformed state (without any limitations on their values) are given by the following formulas similar to those presented in Section 1 (the notation and summation rules are universally accepted):

$$\mathbf{l}_\alpha^* = \frac{(\delta_{\alpha\beta} + e_{\alpha\beta})\mathbf{l}_\beta}{h_\alpha^*}, \quad h_\alpha^* = (1 + 2\varepsilon_{\alpha\alpha})^{1/2}, \quad (4.1)$$

$$E_\alpha = \sqrt{1 + 2\varepsilon_{\alpha\alpha}} - 1, \quad (4.2)$$

$$\sin\gamma_{\alpha\beta} = 2\varepsilon_{\alpha\beta}(1 + 2\varepsilon_{\alpha\alpha})^{-1/2}(1 + 2\varepsilon_{\beta\beta})^{-1/2}, \ \alpha \neq \beta, \quad (4.3)$$

where

$$2\varepsilon_{\alpha\beta} = e_{\alpha\beta} + e_{\beta\alpha} + e_{\alpha\delta}e_{\beta\delta} = \delta_{\beta\pi}e_{\alpha\pi} + \delta_{\alpha\pi}e_{\beta\pi} + e_{\alpha\pi}e_{\beta\pi} = \left(\delta_{\alpha\pi} + \frac{e_{\alpha\pi}}{2}\right)e_{\beta\pi} + \left(\delta_{\beta\pi} + \frac{e_{\beta\pi}}{2}\right)e_{\alpha\pi}, \quad (4.4)$$

$$e_{11} = \frac{1}{H}\frac{\partial u_1}{\partial x^1} + \frac{1}{H_1H_2}\frac{\partial H_1}{\partial x^2}u_2 + \frac{1}{H_1H_3}\frac{\partial H_1}{\partial x^3}u_3,$$

$$e_{12} = \frac{1}{H_1}\frac{\partial u_2}{\partial x^1} - \frac{1}{H_1H_2}\frac{\partial H_1}{\partial x^2}u_1, \quad (4.5)$$

$$e_{13} = \frac{1}{H_1}\frac{\partial u_3}{\partial x^1} - \frac{1}{H_1H_3}\frac{\partial H_1}{\partial x^3}u_1 \quad (1, 2, 3).$$

The formulas

$$E_\alpha \approx \varepsilon_{\alpha\alpha}, \quad (4.6)$$

simplified for small tensile strains, which are analogues of Eqs. (1.5) and follow from Eqs. (4.2) in the approximation $2 + E_\alpha \approx 2$, are commonly accepted. The approximate formulas

$$\gamma_{\alpha\beta} \approx 2\varepsilon_{\alpha\beta}, \quad \alpha \neq \beta \quad (4.7)$$

follow from Eqs. (4.3) in the approximation $(1 + 2\varepsilon_{\alpha\alpha})^{-1/2} \approx 1$ and $\sin\gamma_{\alpha\beta} \approx \gamma_{\alpha\beta}$.

Let the x^α axes be the principal deformation axes at each point of the deformed body. In this coordinate system,

$$\gamma_{\alpha\beta} = 2\varepsilon_{\alpha\beta} = 0 \ \text{ for } \ \alpha \neq \beta. \quad (4.8)$$

These formulas are obtained only if $e_{\alpha\beta} = 0$ for $\alpha \neq \beta$. Then, Eqs. (4.4) yield the formulas

$$2\varepsilon_{\alpha\alpha} = 2e_{\alpha\alpha} + e_{\alpha\alpha}^2. \quad (4.9)$$

Substituting these formulas into Eqs. (4.2), we derive the exact formulas

$$E_\alpha = \sqrt{1 + 2e_{\alpha\alpha} + e_{\alpha\alpha}^2} - 1 = e_{\alpha\alpha}, \quad (4.10)$$

which are similar to formulas (2.4). At the same time, using approximate formulas (4.6), we arrive at the result

$$E_\alpha \approx \varepsilon_{\alpha\alpha} = e_{\alpha\alpha} + \frac{e_{\alpha\alpha}^2}{2}. \quad (4.11)$$

5. CONSISTENT KINEMATIC RELATIONSHIPS IN THE QUADRATIC APPROXIMATION FOR SMALL TENSILE STRAINS AND INTERMEDIATE SHEAR STRAINS

According to the above results for small tensile strains ($E_\alpha \approx \varepsilon$) in orthogonal curvilinear coordinates,

the relationships

$$E_1 \approx e_{11} + \frac{e_{12}^2 + e_{13}^2}{2}, \ldots, \quad (5.1)$$

which are similar to relations (1.8), are more correct than commonly accepted relations. In contrast to Eq. (4.11), Eq. (5.1) admits the limiting transition to formulas (4.10). In this case, to find shear strains, it is necessary to use the relations

$$\sin\gamma_{12} \approx 2\varepsilon_{12}$$
$$= e_{12}(1 + e_{22}) + e_{21}(1 + e_{11}) + e_{13}e_{23}, \ldots, \quad (5.2)$$

similar to relations (1.6).

It is necessary to note that relations (5.1) result from Eqs. (4.4) and (4.6) only when the estimates

$$e_{\alpha\alpha} \approx \varepsilon, \quad e_{\alpha\beta} \approx \sqrt{\varepsilon}, \quad \alpha \neq \beta \quad (5.3)$$

along with the estimates $E_\alpha \approx \varepsilon$ [i.e., when approximations (4.6) are applicable], are valid.

In other words, tensile strains can be small only if $e_{\alpha\alpha}$ are small and $e_{\alpha\beta}$ ($\alpha \neq \beta$) are intermediate. For $h_\alpha^* \neq 1$, the geometrical meaning of the latter quantities is obvious from Eqs. (4.1). For example, $e_{12} = \cos(\mathbf{l}_1^*, \mathbf{l}_2^*)$, etc. Quantities $e_{\alpha\beta}$ ($\alpha \neq \beta$) determine shear strains that are intermediate (i.e., of the order of $\sqrt{\varepsilon}$) in accordance with Eq. (5.2) if estimates (5.3) are valid. Therefore, relations (5.2) with allowance for approximations (5.1) admit the further simplification to the form

$$\gamma_{12} \approx \sin\gamma_{12} \approx 2\varepsilon_{12} \approx e_{12} + e_{21} + e_{13}e_{23}, \ldots . \quad (5.4)$$

Finally, for small tensile strains and intermediate shear strains, the kinematic relationships given by Eqs. (5.1) and (5.4) in the quadratic approximation are correct and well defined. Geometrically nonlinear equations of elasticity theory that are formulated on their basis make it possible to find only the physically realizable forms of stability loss.

For the deformed state under consideration, expressions (4.1) take the form

$$\mathbf{l}_1^* = \mathbf{l}_1 + e_{12}\mathbf{l}_2 + e_{13}\mathbf{l}_3, \quad \mathbf{l}_2^* = e_{21}\mathbf{l}_1 + \mathbf{l}_2 + e_{23}\mathbf{l}_3,$$
$$\mathbf{l}_3^* = e_{31}\mathbf{l}_1 + e_{32}\mathbf{l}_2 + \mathbf{l}_3.$$

These expressions, along with the representations $\boldsymbol{\sigma}_\alpha = \sigma_{\alpha\beta}\mathbf{l}_\beta^* = \tilde{\sigma}_{\alpha\beta}\mathbf{l}_\beta$, provide the relations

$$\tilde{\sigma}_{11} = \sigma_{11} + \sigma_{12}e_{21} + \sigma_{13}e_{31},$$
$$\tilde{\sigma}_{12} = \sigma_{11}e_{12} + \sigma_{12} + \sigma_{13}e_{23}, \quad (5.5)$$
$$\tilde{\sigma}_{13} = \sigma_{11}e_{13} + \sigma_{12}e_{23} + \sigma_{13} \quad (\overrightarrow{1, 2, 3}).$$

These expressions are correct and do not lead to "absurd" force boundary conditions.

ACKNOWLEDGMENTS

This work was supported by the Russian Foundation for Basic Research (project nos. 03-01-00535a and 03-01-00071).

REFERENCES

1. V. V. Novozhilov, *Fundamentals of Nonlinear Theory of Elasticity* (Gostekhteorizdat, Moscow, 1948).
2. L. H. Donnell, *Beams, Plates, and Shells* (McGraw-Hill, New York, 1976; Nauka, Moscow, 1982).
3. F. N. Shklyarchuk, Izv. Ross. Akad. Nauk, Mekh. Tverd. Tela, No. 1, 140 (1998).
4. V. N. Paĭmushin and V. A. Ivanov, Mekh. Kompoz. Mater. **36**, 215 (2000).
5. V. N. Paĭmushin, Dokl. Akad. Nauk **378**, 58 (2001) [Dokl. Phys. **46**, 346 (2001)].
6. V. N. Paĭmushin and V. I. Shalashilin, Dokl. Akad. Nauk **39**, 195 (2003) [Dokl. Phys. **48**, 522 (2003)].
7. V. N. Paĭmushin, Mekh. Kompoz. Mater. **37**, 289 (2001).

Translated by Yu. Vishnyakov

Doklady Physics, Vol. 49, No. 6, 2004, pp. 378–382. Translated from Doklady Akademii Nauk, Vol. 396, No. 5, 2004, pp. 615–619.

MECHANICS

Criterion of the Hydrodynamic Stability of a Layer of a Heavy Fluid over the Light One in a Geothermal Reservoir

A. T. Il'ichev* and G. G. Tsypkin**

Presented by Academician G.G. Chernov February 11, 2004

Received February 27, 2004

1. Experience shows that geothermal systems can be in thermodynamic states such that a water layer exists over a vapor layer [1]. In the framework of classical hydrodynamics, the existence of a heavy fluid over the lighter one always leads to instability known as the Rayleigh–Taylor instability [2]. Schubert and Straus [3] investigated the stability of a water layer over a vapor layer; described a geothermal system, where the phases in an unperturbed state were at rest; and, by means of numerical analysis of the dispersion relation, showed the stability of the system for permeability values $k < 4 \times 10^{-17}$ m^2. The stabilizing factor for the interface was heat transfer caused by the temperature gradient in the entrails. Other physical mechanisms (e.g., the magnetic field [2]) responsible for the stable existence of a heavy fluid over the lighter one are also known in hydrodynamics.

In [4, 5], we considered a more general geothermal system, where the phase motion and phase transition in an unperturbed state were allowed. Calculations showed that there exist regimes of motion with phase transitions, where the water layer over the vapor layer in the geothermal system is stable even for permeability values exceeding the value obtained in [3] by an order of magnitude. The new threshold permeability explains the stability of a number of natural geothermal systems. The character of the arising secondary flows depends on the type of instability. Therefore, it is important to investigate in detail the possible types of transition to instability.

In this paper, we present the results of the analytical investigation of the stability of a flow in the geothermal system described in [4, 5]. The explicit criteria of the nonoscillatory transition to instability are obtained. It is established that the transition to the instability of the interface under the variation of physical parameters occurs through one of the following four mechanisms. First, it occurs spontaneously for all wave numbers of perturbations (degenerate case). Second, an unstable wave number arises at infinity. Third, the threshold of instability is determined by the double zero wave number. Fourth, the threshold of instability is determined by a pair of multiple nonzero wave numbers. In the last two cases, the transition to instability is accompanied by the bifurcations of the simple resonance and 1 : 1 resonance, respectively. These bifurcations lead to the branching of the basic regime describing horizontally homogeneous vertical phase flows and the appearance of secondary regimes depending on the horizontal coordinate. We note that the results of numerical investigation presented in [3] describe only one, 1 : 1 resonance, type of transition to an unstable flow.

2. We consider a high-temperature geothermal reservoir consisting of two high-permeability horizontal strata separated by a low-permeability, sufficiently long horizontal layer. The low-permeability layer represents a strip $y \in (-\infty, \infty) \times [0, L] \ni x$. Let us assume that thermodynamic conditions in the upper ($x < 0$) and lower ($x > L$) strata allow the existence of water and vapor, respectively. Then, the phase-transition interface $x = h$ separating domains occupied by water and vapor exists in the low-permeability layer. For certain boundary conditions and parameters of the process, the flow of phases from the upper stratum to the lower one, as well as the opposite flow, is possible.

In domains occupied by water and vapor, the equations of nonisothermal filtration are valid [6]. Following [2, 3], water and vapor are treated as incompressible. Then, the basic system of equations has the form

$$\begin{gathered} \operatorname{div} v_j = 0, \quad v_j = -\frac{k}{\mu_j}(\operatorname{grad} P - \rho_j g \mathbf{e}_x), \\ (\rho C)_{1,2}\frac{\partial T}{\partial t} + \rho_j C_j v_j \cdot \operatorname{grad} T = \operatorname{div}(\lambda_{1,2}\operatorname{grad} T), \\ \lambda_{1,2} = m\lambda_j + (1-m)\lambda_s, \end{gathered} \tag{1}$$

* *Steklov Institute of Mathematics, Russian Academy of Sciences, ul. Vavilova 42, Moscow, 117966 Russia*
e-mail: ilichev@mi.ras.ru

** *Institute for Problems in Mechanics, Russian Academy of Sciences, pr. Vernadskogo 101, Moscow, 119526 Russia*

1028-3358/04/4906-0378$26.00

$$(\rho C)_{1,2} = m\rho_j C_j + (1-m)\rho_s C_s, \quad j = v, w.$$

Here, v is the filtration rate, m is porosity, k is permeability, μ is viscosity, P is pressure, g is the gravitational acceleration, ρ is density, C is the specific heat at constant pressure, T is temperature, and λ is heat conductivity. The subscripts w, v, and s correspond to water, vapor, and skeleton of the porous medium, respectively, and the subscripts 1 and 2 correspond to the vapor and water domains, respectively.

At the interface, the following relations take place:

$$m\left(1-\frac{\rho_v}{\rho_w}\right)V_n = \frac{k}{\mu_v}\frac{\rho_v}{\rho_w}(\mathrm{grad}P)_{n+} - \frac{k}{\mu_w}(\mathrm{grad}P)_{n-}$$

$$+\frac{k}{\mu_w}\rho_w g\left(1-\frac{\mu_w}{\mu_v}\frac{\rho_v^2}{\rho_w^2}\right),$$

$$mq\rho_w V_n = \lambda_-(\mathrm{grad}T)_{n-} - \lambda_+(\mathrm{grad}T)_{n+}$$

$$-\frac{kq\rho_w}{\mu_w}((\mathrm{grad}P)_{n-} - \rho_w g), \quad T_+ = T_- = T_*, \qquad (2)$$

$$P_+ = P_- = P_*, \quad \ln\frac{P_*}{P_a} = A + \frac{B}{T_*},$$

$$A = 12.512, \quad B = -4611.73, \quad P_a = 10^5 \text{ Pa}.$$

Here, V is the speed of the interface and q is the specific heat of the phase transition. The subscript n denotes the normal and the subscripts plus, minus, and asterisk correspond to quantities in vapor, water, and at the interface, respectively.

Boundary conditions for the pressure and temperature in the high-permeability strata are given by

$$x = 0\colon P = P_0, \quad T = T_0;$$

$$x = L\colon P = P^0, \quad T = T^0.$$

Considering the class of flows, where convective energy transfer is considerably less than conductive transfer, we neglect the nonlinear term in the heat conduction equation [4, 5].

If the pressures and temperatures are constant in the high-permeability strata, then the flow is steady and characterized by the linear distribution of temperature and pressure in domains saturated by water and vapor. Substituting these distributions into the system of boundary conditions (2), we determine the unknown location of the interface $x = h$, as well as the pressure P_* and temperature T_* on this surface [4, 5].

3. For investigation of the normal stability of the flow with the phase-transition interface, we linearize the basic equations. The perturbations of the pressure and temperature satisfy the equations

$$\Delta P = 0, \quad \frac{\partial T}{\partial t} = a_{1,2}\Delta T, \quad \Delta = \frac{\partial^2}{\partial x^2} + \frac{\partial^2}{\partial y^2},$$

$$a_{1,2} = \frac{\lambda_{1,2}}{(\rho C)_{1,2}}, \quad 0 < x < h \cup h < x < L.$$

For the sake of simplicity, we assume that the specific heat and heat conductivity depend only on the corresponding parameters of the skeleton: $a = a_1 = a_2$.

The boundary conditions for perturbations read

$$P = 0, \quad T = 0 \text{ at } x = 0, L,$$

$$P_- = P_+ + \frac{P_0}{L}\Gamma_1\eta, \quad \Gamma_1 = \frac{1}{H} + \frac{P_1 H - P_f}{H(1-H)} \text{ at } x = h,$$

$$T_- = T_+ + \frac{T_0}{L}\Gamma_2\eta, \quad \Gamma_2 = \frac{1}{H} + \frac{T_1 H - T_f}{H(1-H)} \text{ at } x = h,$$

$$P_- = \left(\frac{\partial f(T)}{\partial T}\right)_{T=T_*} T_-$$

$$+\left[\left(\frac{\partial f(T)}{\partial T}\right)_{T=T_*}\left(\frac{\partial T}{\partial x}\right)_- - \left(\frac{\partial P}{\partial x}\right)_-\right]\eta$$

$$= -\frac{P_0 B}{T_0^2}\Gamma T_- - \frac{P_0}{L}\Gamma_0\eta, \quad \Gamma = \frac{P_f}{T_f^2},$$

$$\Gamma_0 = \frac{B}{T_0}\Gamma\frac{T_f - 1}{H} + \frac{P_f - 1}{H} \text{ at } x = h,$$

$$m(1-R)\frac{\partial\eta}{\partial t} = \frac{k}{\mu_v}R\left(\frac{\partial P}{\partial x}\right)_+ - \frac{k}{\mu_w}\left(\frac{\partial P}{\partial x}\right)_-,$$

$$R = \frac{\rho_v}{\rho_w} \text{ at } x = h,$$

$$mq\rho_w\frac{\partial\eta}{\partial t} = \lambda_-\left(\frac{\partial T}{\partial x}\right)_- - \lambda_+\left(\frac{\partial T}{\partial x}\right)_+ - \frac{kq\rho_w}{\mu_w}\left(\frac{\partial P}{\partial x}\right)_-$$

$$\text{at } x = h;$$

where $x = h + \eta(t, y)$ is the interface equation, $T_f = \frac{T_*}{T_0}$, $T_1 = \frac{T^0}{T_0}$, and $P_f = \frac{P_*}{P_0}$, where $P_1 = \frac{P^0}{P_0}$.

Assuming that the unknown functions can be represented as

$$\{P(x, y, t), T(x, y, t), \eta(y, t)\}$$

$$= \{\hat{P}(x), \hat{T}(x), \hat{\eta}\}\exp(\hat{\sigma}t + i\hat{\kappa}y),$$

and using the condition of the existence of a nontrivial

solution, we obtain the dispersion equation

$$F(\sigma, \kappa) \equiv \alpha\coth[\alpha(1-H)]\left[\frac{\omega_w}{a}\Gamma_3\kappa\coth(\kappa H) - (1-R)\sigma + \frac{\omega_v}{a}\Gamma_4 R\kappa\coth[\kappa(1-H)]\right] + \alpha\coth(\alpha H)\left[\frac{\omega_v}{a}\Gamma_5 R\kappa\coth[\kappa(1-H)] + \frac{\omega_w}{a}\Gamma_0\kappa\coth(\kappa H) - (1-R)\sigma\right] + \frac{\omega_v B m q \rho_w R}{T_0}\frac{}{\lambda T_0}\Gamma\kappa\left[\sigma\coth[\kappa(1-H)] + \sigma\frac{\mu_v}{\mu_w}\coth(\kappa H) + \Gamma_1\kappa\frac{\omega_w}{a}\coth(\kappa H)\coth[\kappa(1-H)]\right] = 0. \quad (3)$$

Here,

$$\Gamma_3 = \frac{B}{T_0}\Gamma\frac{T_1 - T_f}{1-H} + \frac{P_f - 1}{H},$$

$$\Gamma_4 = \frac{B}{T_0}\Gamma\frac{T_1 - T_f}{1-H} + \frac{P_1 - P_f}{1-H},$$

$$\Gamma_5 = \frac{B}{T_0}\Gamma\frac{T_f - 1}{H} + \frac{P_1 - P_f}{1-H}, \quad \alpha = \sqrt{\kappa^2 + \sigma},$$

$$\kappa = \frac{\hat{\kappa}}{L}, \quad \sigma = \frac{a\hat{\sigma}}{L^2}, \quad \omega_w = \frac{P_0 k}{m\mu_w}, \quad \omega_v = \frac{P_0 k}{m\mu_v}.$$

From Eq. (3), one obtains the asymptotic value $\sigma = \sigma_0|\kappa|$, $\kappa \to \pm\infty$,

$$\sigma_0 = \left[\frac{\omega_v}{a}R(\Gamma_4 + \Gamma_5) + \frac{\omega_w}{a}(\Gamma_0 + \Gamma_3) + \frac{\omega_w\omega_v}{a}\frac{B}{T_0}\frac{mq\rho_w R}{\lambda T_0}\Gamma\Gamma_1\right] \times\left[2(1-R) - \frac{\omega_v}{a}\frac{B}{T_0}\frac{mq\rho_w R}{\lambda T_0}\left(1 + \frac{\mu_v}{\mu_w}\right)\Gamma\right]^{-1}. \quad (4)$$

In [4, 5], we presented examples of the stable configurations of the geothermal system in question at permeabilities exceeding the critical permeability found in [3] by more than an order of magnitude.

4. Let us consider the nonoscillatory transition to the instability of the regime that is characterized by the interface location at $x = h = \frac{L}{2}$ and is stable at some values of the parameters. The necessary condition of stability ($\sigma < 0$ for all κ) is evidently the negativity of σ_0 in Eq. (4), or, equivalently, the negativity of its numerator

$$\sigma_1 = \omega_v R(\Gamma_4 + \Gamma_5) + \omega_w(\Gamma_0 + \Gamma_3) + \omega_w\omega_v\frac{B}{T_0}\frac{mq\rho_w R}{\lambda T_0}\Gamma\Gamma_1, \quad (5)$$

because its denominator is always positive.

Instability occurs when a value $\kappa_0 > 0$ such that $\sigma(\kappa_0) = 0$ arises upon the variation of the parameters. Substituting $\sigma = 0$ into dispersion equation (3) and taking into account the condition $h = \frac{L}{2}$ ($H = \frac{1}{2}$), we obtain the equality $\sigma_1 = 0$ for all κ. Then, it follows that, for $\sigma_1 > 0$, the quantity σ is positive simultaneously for all κ and the completely unstable regime (for all κ) is separated from the completely stable one by the hypersurface $\sigma_1 = 0$ in the space of the parameters. Therefore, the equality $\sigma_1 = 0$ is a criterion of the nonoscillatory transition to instability. This transition in the case under consideration occurs such that all perturbations become unstable.

5. Let us consider the case of the nondegenerate location of the interface $h \neq \frac{L}{2}$ ($H \neq \frac{1}{2}$).

Setting $\sigma = 0$ in dispersion relation (3) and dividing both of its sides by the positive function $\kappa^2\coth^2(1-H)\kappa$, we arrive at the equation

$$\Gamma_0\omega_w Z^2(\kappa) + \left(\omega_w\Gamma_3 + \omega_v\Gamma_5 R + \frac{\omega_v\omega_w B m q \rho_w R}{\lambda T_0^2}\Gamma\Gamma_1\right)Z(\kappa) + \omega_v\Gamma_4 R = 0, \quad (6)$$

where

$$Z(\kappa) = \frac{\coth H\kappa}{\coth(1-H)\kappa}.$$

It follows from Eq. (6) that

$$Z(\kappa) = Z_{1,2} = d \pm \sqrt{d^2 - b}, \quad (7)$$

where

$$d = -\frac{1}{2\Gamma_0}\left(\Gamma_3 + \frac{\omega_v}{\omega_w}\Gamma_5 R + \frac{\omega_v B m q \rho_w R}{\lambda T_0^2}\Gamma\Gamma_1\right),$$

$$b = \frac{\omega_v}{\omega_w}\frac{\Gamma_4}{\Gamma_0}R.$$

The left-hand side of Eq. (7) is an even and monotonic function of κ for $\kappa > 0$, and $\min\left[\frac{1-H}{H}, 1\right] \leq Z(\kappa) \leq \max\left[\frac{1-H}{H}, 1\right]$. The values $Z(\kappa)$ given by

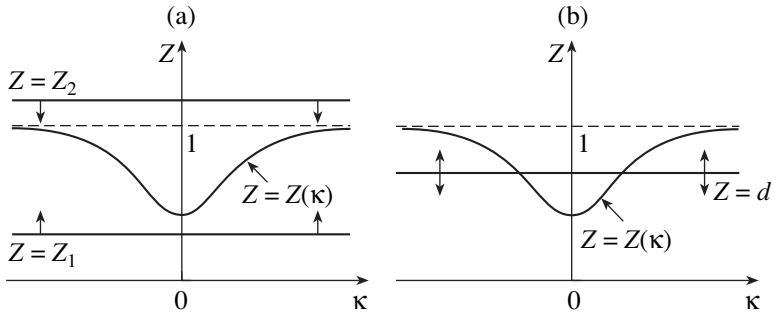

Fig. 1. Transition to instability in cases (a) (i) and (ii) and (b) (iii) for $H > \frac{1}{2}$. In case (i), the threshold of instability at $\kappa = \pm\infty$ is reached upon variation of the physical parameters when the line $Z = Z_2$ moving downward reaches the asymptote of the curve $Z = Z(\kappa)$. In case (ii), the threshold of instability is reached when the line $Z = Z_1$ moving upward touches the curve $Z = Z(\kappa)$ at the point $\kappa = 0$. In case (iii), for $D = 0$, the straight line $Z = d$ arises and, upon developing instability, splits into two lines moving in opposite directions.

Eq. (7) are real if the radicand is nonnegative. Instability takes place if Eq. (7) has finite simple real roots (their number is even, because the function $Z(\kappa)$ is symmetric), and the threshold of instability is reached when the real roots of this equation disappear (or appear). The appearance of the real roots of the first equation in (7) upon varying the physical parameters is possible only in the following cases.

(i) For $D = d^2 - b > 0, H < \frac{1}{2}, d < 1, Z_1 = 1$ or $H > \frac{1}{2}$, $d > 1$, and $Z_2 = 1$. These equalities occur at $\kappa = \pm\infty$, and the infinite wave number corresponds to the threshold of instability. As follows from Eq. (7), the conditions of transition to instability in this case are equivalent to the condition $\sigma_1 = 0$, where σ_1 is determined by Eq. (5). The parameter domains $\sigma_1 < 0$ and $\sigma_1 > 0$ correspond to the stable and unstable regimes, respectively. The transition to instability in the case $H > \frac{1}{2}$ is illustrated in Fig. 1a.

(ii) For $D > 0, H > \frac{1}{2}, d < \frac{1-H}{H}, Z_1 = \frac{1-H}{H}$ or $H < \frac{1}{2}, d > \frac{1-H}{H}$, and $Z_2 = \frac{1-H}{H}$. These equalities occur at $\kappa = 0$. As follows from Eq. (7), the conditions of transition to instability in this case are equivalent to the condition

$$\sigma_2 = \sigma_1 - \frac{1-2H}{H}\left(\frac{\omega_v H}{1-H}\Gamma_4 R - \omega_w \Gamma_0\right) = 0. \quad (8)$$

This equality is satisfied at zero wave number κ, which is a double root of Eq. (7). The parameter domains $\sigma_2 < 0$ and $\sigma_2 > 0$ correspond to the stable and unstable regimes, respectively. When the threshold of instability is not yet reached, i.e., at $\sigma_2 = \mu < 0, \mu \ll 1$, Eq. (7) has no real roots. At $\mu = 0$, the threshold of instability is reached, and the branch of the dispersion relation touches the axis $\sigma = 0$ at the point $\kappa = 0$ corresponding to the double root of Eq. (7). When, with further variation of parameters, the quantity σ_2 becomes positive, $\sigma_2 = \mu > 0, \mu \ll 1$, there are exactly two real (positive and negative) values κ satisfying Eq. (7) because the function $Z(\kappa)$ is monotonic. The transition to instability in the case $H > \frac{1}{2}$ is illustrated in Fig. 1a.

(iii) For $D = 0$, $\min\left[\frac{1-H}{H}, 1\right] < d < \max\left[\frac{1-H}{H}, 1\right]$. The equality $D = 0$ is satisfied at two nonzero values κ symmetric about zero. Each of these values is a double root of Eq. (7). Crossing the hypersurface determined in the space of the parameters by this equality, the system loses its stability: for $\sigma_1 < 0$, the parameter domains $D < 0$ and $D > 0$ correspond to the stable and unstable regimes, respectively. For $D = \mu$, where $\mu < 0$, Eq. (7) has no real roots. At $\mu = 0$, the transition to instability takes place and the roots of Eq. (7) reach the real axis from the complex plane. In this case, the branch of the dispersion relation touches the axis $\sigma = 0$ at the points corresponding to a pair of nonzero wave numbers. When, with further variation of the parameters, D ($\mu > 0$) becomes positive, and there are two wave number segments that lie on the real axis, are symmetric about the origin, and bounded by the roots of Eq. (7). These wave numbers are associated with unstable normal modes. The transition to instability in the case $H > \frac{1}{2}$ is illustrated in Fig. 1b.

The system of equations (1) in the absence of the time dependence of its solutions may be written in the form of an infinite-dimensional dynamical system, where the unbounded horizontal variable y plays the role of time. Bifurcation takes place when eigenvalues ν of the operator that is associated with the right-hand

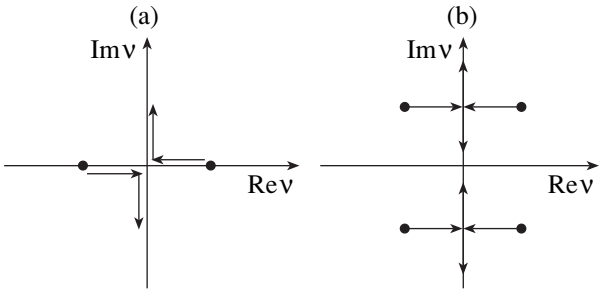

Fig. 2. Motion of the eigenvalues ν on the imaginary axis and those reaching the imaginary axis upon varying the parameter μ from negative to positive values for cases (a) (ii) and (b) (iii) of the transition to instability.

side of this dynamical system and is defined in a domain including the relations obtained by the linearization of boundary conditions (2) reach the imaginary axis. According to the correspondence $\kappa = i\nu$, it occurs in cases (ii) and (iii) of the transition to instability when dispersion equation (7) has either a double zero root or a pair of nonzero double roots at $\sigma = 0$. Bifurcations lead to the formation of horizontally inhomogeneous secondary regimes separating from the vertical flow losing its stability.

Because the function $F(0, \kappa)$ in Eq. (3) is even due to the reversibility of Eqs. (1) and boundary conditions (2) for $\frac{\partial}{\partial t} = 0$, the eigenvalues ν reach the imaginary axis in pairs. The motion of the eigenvalues when μ crosses the origin in the direction of the positive real semiaxis is shown in Figs. 2a and 2b for cases (ii) and (iii), respectively.

The type of bifurcations that corresponds to such a motion is well known and refers to the simple resonance and 1 : 1 resonance, respectively (see, e.g., [7]).

ACKNOWLEDGMENTS

This work was supported by the Russian Foundation for Basic Research (project no. 02-01-00486) and the Council of the President of the Russian Federation for Support of Young Russian Scientists and Leading Scientific Schools (project no. NSh-1697.2003.1).

REFERENCES

1. M. A. Grant, Geothermics **12**, 251 (1983).
2. S. Chandrasekhar, *Hydrodynamic and Hydromagnetic Stability* (Oxford Univ. Press, New York, 1967).
3. G. Schubert and J. M. Straus, J. Geophys. Res. **85**, 6505 (1980).
4. G. G. Tsypkin and A. T. Il'ichev, Dokl. Akad. Nauk **378**, 197 (2002) [Dokl. Phys. **46**, 359 (2002)].
5. G. Tsypkin and A. Il'ichev, Transp. Porous Media **55**, 183 (2004).
6. M. J. O'Sullivan, Int. J. Energy Res. **9**, 319 (1985).
7. A. T. Il'ichev, *Solitary Waves in Models of Hydromechanics* (Fizmatlit, Moscow, 2003).

Translated by A. Il'ichev

Doklady Physics, Vol. 49, No. 6, 2004, pp. 383–385. Translated from Doklady Akademii Nauk, Vol. 396, No. 5, 2004, pp. 620–623.

MECHANICS

Crack Growth Direction According to the Novozhilov Criterion

S. A. Nazarov

Presented by Academician N.F. Morozov December 25, 2003

Received February 10, 2004

The fracture criterion

$$\frac{1}{d}\int_0^d \sigma_{\varphi\varphi}(r, \varphi)|_{\varphi = \theta} dr = \sigma_c, \qquad (1)$$

proposed by Novozhilov [1] for finding the equilibrium state of cracks was adapted in [2–4] and in other studies to the determination of critical loads in the case of arbitrary stress concentrators. As is shown in the present study, this criterion makes it possible to establish both the direction of crack propagation and the possibility of branching in the case of crack formation from the vertex $\mathbb{O}$ of an angular cut in a homogeneous elastic brittle solid. In formula (1), the integration is performed along a segment I of length d initiated at the point $\mathbb{O}$, where (r, φ) are the polar coordinates with the center at the point $\mathbb{O}$ and $|\varphi| < \alpha$. Since the material is not assumed to be isotropic, its characteristics $d = d(\theta)$ and $\sigma_c = \sigma_c(\theta)$, as well as the characteristic size of the medium (e.g., grain diameter [3]) and the critical stress (theoretical strength [5]), are considered to be smoothly dependent on the direction $\theta \in (-\alpha, \alpha)$ of the segment $I = I(\theta)$. We emphasize that the aforementioned functions may have jumps or removable singularities that determine the preferable direction of the crack propagation (cf. [6]). This relates, e.g., to the case of reinforcement by high-strength fibers. However, such situations are beyond the scope of this work. In addition, the analysis deals only with the quasi-static development of cracks. The criterion of the incubation time [4] that generalizes criterion (1) for dynamic fracture was applied in [7] for the determination of the crack sprout deviation angle.

Let an external load $p(x, \tau)$ be applied to the surface of a plane solid in the absence of volume forces. The load is dependent on the dimensionless timelike parameter τ, which is a strictly monotonic function of the actual time t. The variation rate of this parameter is assumed to be much lower than the elastic-wave propagation velocity normalized to the characteristic size l of the body (e.g., to the crack length, but not to the parameter $d \ll l$). We also ignore inertial forces and deal with the quasi-static fracture process. In a complex stress state, no crack directions are preferable. Therefore, the problem of fracture mechanics is formulated as follows. One has to determine the time $\tau = \tau_*$ for which equality (1) is satisfied for a certain angle θ but the left-hand side of Eq. (1) for $\tau < \tau_*$ is strictly smaller than $\sigma_c(\theta)$ for an arbitrary θ value. The corresponding load $p(x, \tau_*)$ is just critical. In other words, the function

$$(-\alpha, \alpha) \ni \theta \to F(\tau_*; \theta) - \sigma_c(\theta),$$

where

$$F(\tau_*; \theta) = \frac{1}{d(\theta)} \int_0^{d(\theta)} \sigma_{\varphi\varphi}(\tau_*; r, \theta) dr \qquad (2)$$

reaches the global maximum (equal to zero) at one or several points, but $F(\tau, \theta) - \sigma_c(\theta) < 0$ for $\tau < \tau_*$ at all θ. This formulation is adequate for many fracture criteria. Generally speaking, it can be derived on the basis of the dynamic-fracture criterion [7] in the case of slow simple loading by setting $\tau = vt$, where $v > 0$ is the relative loading rate, and replacing σ_c by $\left(1 - \frac{1}{2} vt_0\right)^{-1} \sigma_c$, where $t_0 > 0$ is the incubation time (see, e.g., [4]). Since v is low, inertial terms can be disregarded and the additional coefficient of σ_c can be eliminated. It is worth mentioning a new conclusion that, if the equation $F(\tau_*; \theta) = \sigma_c(\theta)$ has several roots $\theta_i \in (-\alpha, \alpha)$, the formation of several cracks can be expected (if $\alpha = \pi$, then the main crack branches).

We fix the angle θ and introduce Cartesian coordinates (s, n) with the s axis along the segment $I(\theta)$. Using the equilibrium equation

$$\frac{\partial}{\partial s}\sigma_{ss} + \frac{\partial}{\partial n}\sigma_{sn} = 0, \quad \frac{\partial}{\partial s}\sigma_{ns} + \frac{\partial}{\partial n}\sigma_{nn} = 0, \qquad (3)$$

Institute of Problems of Mechanical Engineering, Russian Academy of Sciences, Bol'shoĭ pr., Vasil'evskiĭ ostrov, St. Petersburg, 199178 Russia
e-mail: serna@snark.ipme.ru

1028-3358/04/4906-0383$26.00

we represent the derivative F' of the function F with respect to the variable θ in the form

$$F'(\tau;\theta) = -\frac{d'(\theta)}{d(\theta)}F(\tau;\theta)$$

$$+ d'(\theta)\sigma_{nn}(\tau; d(\theta), \theta) + \frac{1}{d(\theta)}J(\tau;\theta),$$

$$J = \int_0^d \frac{\partial}{\partial\theta}\sigma_{nn}dr = \int_0^d s\frac{\partial}{\partial n}\sigma_{nn}ds$$

$$= -\int_0^d s\frac{\partial}{\partial s}\sigma_{ns}ds = \int_0^d \sigma_{ns}ds - d\sigma_{ns}\big|_{n=0,\,s=d}.$$

As a result, we arrive at the relationship

$$F'(\tau;\theta) = \left(1 + \left[\frac{d'(\theta)}{d(\theta)}\right]^2\right)^{1/2}$$

$$\times\left\{\frac{1}{d(\theta)}\int_0^{d(\theta)} \sigma_{nN}(\tau; r, \theta)dr - \sigma_{nN}(\tau; d(\theta), \theta)\right\}. \quad (4)$$

Here, N corresponds to the direction tangential to the plot of the function $r = d(\varphi)$ at the point $\varphi = \theta$.

Thus, when a crack is formed from the vertex $\mathbb{O}$ in the direction θ, expression (4) for the time $\tau = \tau_*$ coincides with the derivative $\sigma_c'(\theta)$. If the strength properties are isotropic (the elastic properties of the solid under consideration may keep anisotropy), the condition obtained above is simplified to the form

$$\sigma_{r\varphi}(\tau_*; d, \theta) = \frac{1}{d}\int_0^d \sigma_{r\varphi}(\tau_*; r, \theta)dr. \quad (5)$$

In other words, the tangential stress at the end of the segment $I(\theta)$ coincides with the mean value of this stress over the segment. In the case of a simple loading, $p(x;\tau) = \tau p^0(x)$, the angle θ is independent of the instant of fracture, so that the argument τ_* can be omitted in Eq. (5).

We note that Eq. (5) is only a necessary condition. For example, if the surface of the angular cut is free of stresses, then $\sigma_{c\varphi}(r, \pm\alpha) = 0$, and, consequently, equality (5) is satisfied for $\theta = \pm\alpha$. At the same time, $\sigma_{\varphi\varphi}(r, \pm\alpha) = 0$ and requirement (1) is certainly violated.

If the length d is negligibly small, the stress $\sigma_{r\varphi}(\tau_*, r, \varphi)$ can be replaced in some cases by the leading term $r^{\Lambda-1}\Sigma_{r\varphi}(\tau_*;\varphi)$ of its asymptotic expansion (for details, see [2], where, in particular, it is explained when this replacement is impossible). As a result, Eq. (5) for $\Lambda \neq 1$ provides the rather simple condition

$$\Sigma_{r\varphi}(\tau^*;\theta) = 0. \quad (6)$$

Thus, the crack propagates in the direction of the absence of tangential stresses. This conclusion is similar to the well-known criterion $K_{II} = 0$. However, it is known that this criterion in its *a posteriori* formulation (the coefficient K_{II} of the stress intensity vanishes in the vertex of the small crack branch) for isotropic solids (see [8, 9]) indicates a direction differing from that found by means of formula (6).

After the replacement $\sigma_{\varphi\varphi} \to r^{\Lambda-1}\Sigma_{\varphi\varphi}$, Novozhilov criterion (1) transforms into the criterion of the maximum tensile stress; the calculations show the necessity of condition (6) for this stress. We emphasize that, analyzing the crack propagation direction in an orthotropic material, Petrov and Ponikarov [10] used the above asymptotic version rather than criterion (1) itself. In this case, the parameter d was considered to be constant, and the quantity $\sigma_c(\theta)$ was taken to be equal to $\sigma_{cx}(\sin\theta)^2 + \sigma_{cy}(\cos\theta)^2$. The deviation of the crack from the rectilinear path that was found in [10] is caused only by the variability of the strength characteristic σ_c.

A rather interesting conclusion follows from formula (6). Since the angular part $\Sigma_{\varphi\varphi}(\tau, \varphi)$ of tensile stresses vanishes at $\varphi = \pm\alpha$, it takes the maximum (or minimum) value at the point φ_* within the interval $(-\alpha, \alpha)$. In this case, $\Sigma_{\varphi r}(\tau; \varphi_*) = 0$, and, consequently, the angular part of shear stress must change its sign within the interval $(-\alpha, \alpha)$ for an arbitrary anisotropic material and opening angle.

We now discuss the nucleation of an edge crack initiated at the point $\mathbb{O}$ of the rectilinear segment $\Gamma \in \{(x, y): y = 0\}$ of the boundary free of external actions. Since the stresses σ_{xy} and σ_{yy} vanish in Γ, we have

$$\begin{aligned}\sigma_{\varphi\varphi}(r, \varphi) &= \sigma_{xx}(\mathbb{O})\cos^2\varphi + O(r),\\ \sigma_{r\varphi}(r, \varphi) &= -\sigma_{xx}(\mathbb{O})\cos\varphi\sin\varphi + O(r).\end{aligned} \quad (7)$$

Let $\sigma_{xx}(\mathbb{O}) > 0$, the material be homogeneous, and its strength properties be isotropic (the last requirement does not relate to elastic properties). We note that relationship (6) for $\Lambda = 1$ does not formally follow from Eq. (5). However, it remains valid in any case. According to the leading terms of expansions (7), the crack nucleates perpendicularly to the boundary. Further, we take into account the lower terms of the expansions:

$$\begin{aligned}\sigma_{xx}(x, y) &= s_0 + s_1x + s_2y + s_{11}x^2\\ &\quad + 2s_{12}xy + s_{22}y^2 + O(r^3),\\ \sigma_{xy}(x, y) &= -s_1y - 2s_{11}xy - s_{12}y^2 + O(r^3),\\ \sigma_{yy}(x, y) &= s_{11}y^2 + O(r^3).\end{aligned} \quad (8)$$

We emphasize that only two of the coefficients s_{jk} are free, and the complementary relation generally includes elastic constants (in the isotropic case, $2s_{11} + s_{22} = 0$ due to the Mitchell equation). It is reasonable to assume that tensile forces are maximal at the nucleation point of the edge crack, i.e.,

$$s_0 = \sigma_{xx}(\mathbb{O}) > 0, \quad s_1 = \partial_x\sigma_{xx}(\mathbb{O}) = -\partial_y\sigma_{xy}(\mathbb{O}) = 0,$$
$$s_2 = \partial_y\sigma_{xx}(\mathbb{O}) > 0, \quad 2s_{12} = \partial_x\partial_y\sigma_{xx}(\mathbb{O}) = -\partial_y^2\sigma_{xy}(\mathbb{O}). \tag{9}$$

In the framework of the Novozhilov criterion, the variability of stress field (8) causes a deviation of the crack direction from the perpendicular by a (small) angle θ. Indeed, the substitution of Taylor formulas (8) into relationship (5) yields

$$\theta = \frac{2}{3}d^2\frac{s_{12}}{s_0} + O(d^3). \tag{10}$$

If $s_1 = 0$ and $s_{12} = 0$, then the symmetry of field (8) with respect to the y axis holds in principal, and, according to Eq. (10), the direction of the edge crack coincides with a perpendicular to the boundary within high accuracy.

We now analyze the problem of crack branching. In the absence of volume forces on free crack sides for an isotropic material, we have $\Lambda = \frac{1}{2}$ and

$$\Sigma_{r\varphi}(\varphi) = \frac{1}{\sqrt{2\pi}}\frac{1}{4}\left\{K_\mathrm{I}\left[\sin\frac{3}{2}\varphi + \sin\frac{1}{2}\varphi\right]\right.$$
$$\left. + K_\mathrm{II}\left[3\cos\frac{3}{2}\varphi + \cos\frac{1}{2}\varphi\right]\right\}, \tag{11}$$

where K_I and K_II are the stress intensity coefficients. As was mentioned above, Eqs. (2) and (4)–(6) show that crack branching requires that the angular part of Eq. (11) vanish at least twice within the interval $(-\pi, \pi)$ and change its sign from plus to minus in this case. This statement implies that the function $\Sigma_{r\varphi}$ must have no less than five roots within the segment $[-\pi, \pi]$. A third-order harmonic polynomial of the variable $\frac{\varphi}{2}$ obviously does not have this property. The absence of this number of roots is immediately shown by taking into account that the derivative of the factor after K_I with respect to φ coincides with half the factor after K_II (cf. [11]).

Thus, in the framework of the Novozhilov criterion, the crack does not branch when the parameter d is negligibly small. This conclusion is consistent with the well-known experimental fact that quasi-static crack branching (free of dynamic effects) is not observed in a homogeneous isotropic brittle material.

ACKNOWLEDGMENTS

This work was supported by the Russian Foundation for Basic Research, project no. 03-01-00835.

REFERENCES

1. V. V. Novozhilov, Prikl. Mat. Mekh. **33**, 797 (1969).
2. N. F. Morozov, Dokl. Akad. Nauk SSSR **253**, 1336 (1980) [Sov. Phys. Dokl. **25**, 656 (1980)].
3. N. F. Morozov and V. V. Novozhilov, Fiz.-Khim. Mekh. Mater. **24**, 21 (1988).
4. N. Morozov and Y. Petrov, *Dynamics of Fracture* (SPbGU, St. Petersburg, 1990; Springer-Verlag, Berlin, 2000).
5. L. M. Kachanov, *Fundamentals of Fracture Mechanics* (Nauka, Moscow, 1974).
6. D. Leguillon and E. Sanchez-Palencia, in *New Advances in Computational Structural Mechanics* (Elsevier, New York, 1992), pp. 423–434.
7. N. F. Morozov, Yu. V. Petrov, and A. A. Utkin, Dokl. Akad. Nauk **351**, 763 (1996) [Phys. Dokl. **41**, 615 (1996)].
8. M. Amestoy and J. B. Leblond, Int. J. Solids Struct. **29**, 465 (1992).
9. I. I. Argatov and S. A. Nazarov, Prikl. Mat. Mekh. **66**, 502 (2002).
10. Yu. V. Petrov and N. V. Ponikarov, Izv. Akad. Nauk, Mekh. Tverd. Tela, No. 4, 180 (1998).
11. S. A. Nazarov and O. R. Polyakova, Izv. Akad. Nauk, Mekh. Tverd. Tela, No. 1, 104 (1995).

Translated by G. Merzon

Doklady Physics, Vol. 49, No. 6, 2004, pp. 386–388. Translated from Doklady Akademii Nauk, Vol. 396, No. 5, 2004, pp. 624–627.

MECHANICS

Electric-Discharge Control over a Vortex Flow around Bodies of Revolution

Corresponding Member of the RAS V. M. Fomin[1], A. A. Maslov[1], B. Yu. Zanin[1], A. A. Sidorenko[1,*], V. P. Fomichev[1], B. V. Postnikov[1], and N. Malmuth[2]

Received February 13, 2004

The key feature of a flow around axisymmetric bodies at large angles of attack is the formation of a conic vortex flow, where a pair of primary vortices dominates (Fig. 1). With an increase in the ratio of the angle of attack α to the half-apex angle θ of the model vertex, the initial attached flow is transformed to a detached flow with the formation of a pair of symmetric stationary vortices. With a further increase in the parameter $\frac{\alpha}{\theta}$, the flow is abruptly rearranged with the formation of an asymmetric pair of vortices. This process is associated with the loss of the stability of the vortex flow above the critical parameter $\frac{\alpha}{\theta}$ [1–3]. Small asymmetry of the forward part, roughness, and irregularity of the outer flow may serve as initial perturbations. In addition, this process depends on the presence or absence of the transition from a laminar flow to a turbulent one in the preseparation region of the flow [4]. The change of a symmetric flow to an asymmetric one is not very predictable and generally undesirable, because it generates uncontrollable lateral loading on the streamlined body [3].

It is known that the initial asymmetry of a vortex flow arises near the model vertex and holds downstream. The characteristic feature of large-scale vortices arising in the separation region is their high sensitivity to external perturbations, which enables one to control the flow by creating artificial perturbations at the place of their origin. Attempts to control a vortex flow around axisymmetric bodies were successfully realized by action on the flow near the vertex [5, 6]. Traditional methods such as change in the vertex shape, use of various vortex generators, and injection–suction of the gas are usually considered.

In this work, we analyze the possibility of using an electric discharge for controlling the symmetry of the vortex flow around a cone at the angle of attack. The possibility of fast change in both the discharge frequency and its power provides flexible control over the intensity of action and its application in feedback control systems for flows. A spark gap is a set of electrodes placed on the surface along generatrices of the cone. Various pairs or groups of electrodes can be used, depending on the velocity of the incident flow and the angle of attack.

Despite numerous studies in this direction, the basic physical processes accompanying the separation of the flow on bodies of revolution are poorly understood. The possibilities of controlling the asymmetry of the flow were theoretically analyzed in [7], where the basic idea was the plasma action on hydrodynamic stability at the key singular points of the flow. Flow control strategy implies that the position of flow separation lines on both sides of the cone can be changed by an electric discharge. In this case, the discharge can be treated as a source of artificial periodic oscillations, as a local heat source, or as a stationary bulge on the cone surface. In any case, the discharge introduces additional perturbation into the initial flow and finally shifts the separation

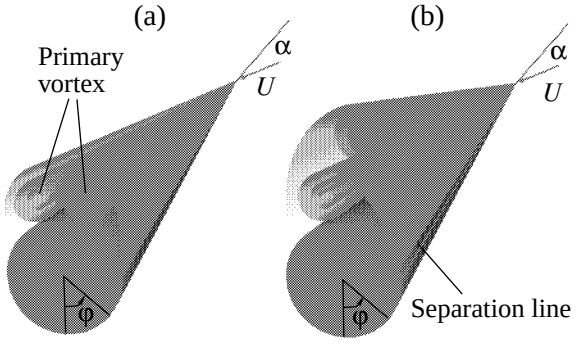

Fig. 1. Scheme of the flow around an axisymmetric cone at a large angle of attack for the (a) symmetric and (b) asymmetric configurations of vortices.

[1] *Institute of Theoretical and Applied Mechanics, Siberian Division, Russian Academy of Sciences, ul. Institutskaya 4/1, Novosibirsk, 630090 Russia*

[2] *Rockwell Scientific Company, 1049 Camino Dos Rios, Thousand Oaks, California, USA*

* *e-mail: sindr@itam.nsc.ru*

1028-3358/04/4906-0386$26.00 © 2004 MAIK "Nauka/Interperiodica"

point upstream from the saddle point of the transverse flow. As a result, vortices are displaced from the surface, and the distance between their centers increases. The saddle point of the transverse flow is shifted towards the surface of the model, and a more stable state preventing the appearance of asymmetry is achieved. According to estimates made in [7], the heating of a gas by 50–100 K by a thin cylindrical (1 mm in diameter) volume heat source placed along the initial flow-separation line is enough for the necessary displacement of the separation line. The lower boundary of the required power is estimated as 200 W for a discharge length of 1 m with a specific power of 2 W/cm.

Experiments were carried out in a small-turbulent aerodynamic tube T-324 at the Institute of Theoretical and Applied Mechanics, Siberian Division, Russian Academy of Sciences, in the flow velocity range $U = 5$–20 m/s. The turbulence level of the free flow in the setup was less than 0.04% for the cross section 1×1 m of the closed working section. The average velocities and velocity pulsations in the boundary layer and flow separation regions were measured by a hot-wire anemometer, static pressure distributions over the model surface were determined, and the vortex structure of the flow was visualized by the laser knife method.

A 1-m-long cone model with a half-angle of 5° was used in experiments. The model was placed in the working section of the aerodynamic tube at the angle of attack $\alpha = 0°$–40° and had a set of changeable heads with various shapes and a dielectric insertion, where electric spark gaps were placed. Pressure on the model surface was measured at ten points uniformly distributed over a circle in the cross section at distance $x = 576$ mm. Investigations were carried out for the separation of both laminar and turbulent boundary layers. In the latter case, abrasive-paper turbulizers were stuck on the model to ensure the transition of the preseparation boundary layer to the turbulent state.

Initial experiments were carried out without electric spark gaps and aimed to analyze the structure of an unperturbed flow and to determine cone-surface domains, where the discharge action would be applied most efficiently. These domains were sought by means of bulges 3–5 mm in height and 20–100 mm in length that were mounted symmetrically with two sides of the model before the flow separation lines at various distances from the cone vertex.

Experiments show that, for flow velocities from 10 to 15 m/s, vortices over the model without bulges are located symmetrically if the angle of attack α does not exceed 15° (Fig. 1). With an increase in α to 20°, the vortex pattern is transformed to an asymmetric one, and the directions of asymmetry are different for different angles of attack. This behavior is caused by small transverse changes in the position of the model and testifies to the high sensitivity of the flow to small inhomogeneities of the flow. It was found that the symmetric vortex pattern of the flow could be reached by the installation of bulges. The placing of bulges near the vertex of the model is most efficient. Bulges may be shorter if they are placed closer to the vertex. This result is consistent with the data obtained in [5], where it was experimentally shown that small action near the vertex could change the pattern of the entire flow.

According to the above results, electric spark gaps are placed on the both sides of the model as close as possible to the vertex. Electrodes were mounted such that the plasma channel was upstream from the separation line and oriented along a generatrix of the cone. Both arc and spark discharges were used in experiments. An arc discharge was ignited between two electrodes that were mounted flush on the cone surface and spaced by 10 mm. The discharge runs off a high voltage source with industrial frequency (50 Hz) through a ballast resistor. The discharge current was equal to about 100 mA for 1200-V voltage on the arc. The spark discharge was generated on the array of electrodes, which were mounted flush on the cone surface, by the method described in [8]. The distance between the outer electrodes was equal to 20 mm. The discharge runs off a pulsed generator with a voltage up to 20 kV. The discharge duration was equal to about 10 μs, and the repetition frequency was equal to 400 Hz.

The effect of the arc discharge on the flow pattern was studied on the cone model with both sharp and hemispherical heads with a radius of 10 mm. The distance from the model vertex to the first electrode was equal to 150 and 55 mm, respectively. The discharge power was insufficient for controlling the flow structure in the sharp-vertex configuration. The blunted configuration ensures the location of the electric spark gaps closer to the model vertex, which must increase the efficiency of the action. The use of the hemispherical head for the same discharge power allows the efficient control over the flow and a symmetric vortex pattern.

The effect of the simultaneous action of two symmetric arc discharges from both right and left sides of the model was analyzed. In these experiments, the total electric power of two discharges was constant and equal to about 120 W. The discharge was initially ignited only on the first (right) electric spark gap. After 3–5 s, the second discharge was ignited and power was about equally distributed between the discharges (about 60 W per channel). This procedure made it possible to obtain data corresponding to the symmetric and asymmetric actions on the flow in the same experiment.

Figure 2 shows the distribution of the pressure coefficient C_p over the model surface. The pressure coefficient is defined as the difference between static pressure at a given point and static pressure in the incident flow as divided by the velocity head. It is seen that the initially symmetric state is distorted by the discharge from the right and was partially restored by two symmetric discharges.

For experiments with a spark discharge, a head with a radius of 2.5 mm was mounted on the model. The flow

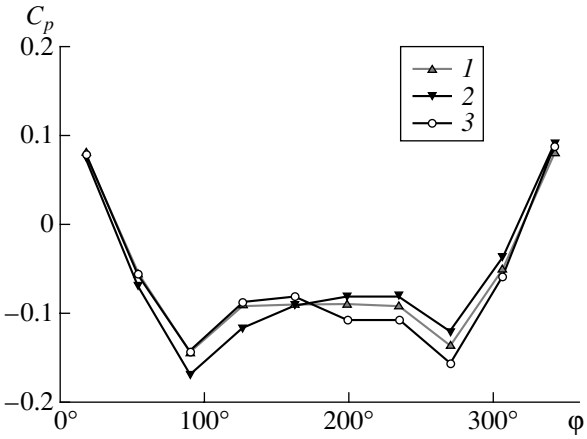

Fig. 2. Distribution of the pressure coefficient over the model surface in the cross section x = 576 mm in the presence of an arc discharge: (*1*) without discharge, (*2*) discharge on the right is turned on, and (*3*) discharge on both sides is turned on.

Fig. 3. Initial asymmetric pattern obtained by smoking visualization by the laser-knife method for a flow without a spark discharge for the parameters U = 15 m/s and $\alpha = 17.5°$.

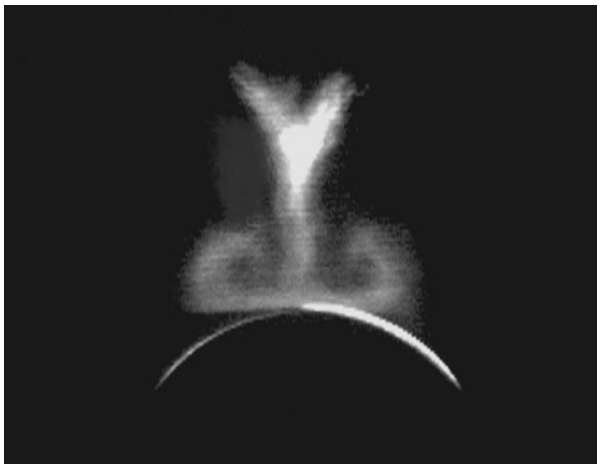

Fig. 4. Symmetric pattern obtained by smoking visualization by the laser-knife method for a flow with a spark discharge for the parameters U = 15 m/s and $\alpha = 17.5°$.

velocity varied from 9.2 to 15 m/s, and the angle of attack, from 17.5° to 20°. The discharge was ignited from the right, left, or from the both sides of the model simultaneously. In the flow around the model without the discharge, right asymmetry was observed; i.e., the vortex on the right side was further from the model than the vortex on the left side (see Fig. 3). In this case, the symmetric state was obtained by the ignition of the discharge on the left side of the model (Fig. 4). When both discharges were used simultaneously, the flow was also symmetrized. When the discharge appeared, the vortex trace was transformed to the symmetric state and remained symmetric when the discharge was turned on. When the discharge was turned off, the flow returned to the asymmetric state. For various flow velocities and discharge powers, various vortex configurations with different degrees of asymmetry were obtained. With an increase in the flow velocity, the effect of the spark discharge was weakened due to insufficient discharge power.

Thus, the use of an electric discharge near the vertex of an axisymmetric body streamlined at the angle of attack was experimentally shown to be an efficient mechanism of controlling the flow. We achieved both the symmetrization of an initially asymmetric flow and control over the direction of artificially created asymmetry and, therefore, over the aerodynamic force. Moreover, the effect of proportional control, when the aerodynamic force monotonically depends on the action intensity, was obtained. The results enable one to consider an electric discharge as an active element of control systems for promising aircraft.

ACKNOWLEDGMENTS

This work was supported by the International Science and Technology Center, project no. 2235.

REFERENCES

1. A. M. Skow and D. J. Peake, AGARD Lect. Ser. **121**, 10-1 (1982).
2. B. L. Hunt, AIAA Pap., No. 82-1336 (1982).
3. L. E. Ericsson and J. P. Reding, AIAA Pap., No. 85-1797 (1985).
4. P. J. Lamont, AIAA J. **20**, 1492 (1982).
5. J. E. Bernhardt and D. R. Williams, AIAA J. **36**, 2087 (1998).
6. J. E. Bernhardt and D. R. Williams, J. Aircr. **37**, 491 (2000).
7. V. I. Shalaev, A. V. Fedorov, N. Malmuth, *et al.*, AIAA Pap., No. 2003-34 (2003).
8. S. P. Bardakhanov, V. V. Kozlov, and A. N. Malov, Izv. Sib. Otd. Akad. Nauk SSSR, Ser. Tekh. Nauki, No. 7, 53 (1988).

Translated by R. Tyapaev

Doklady Physics, Vol. 49, No. 6, 2004, pp. 389–392. Translated from Doklady Akademii Nauk, Vol. 396, No. 6, 2004, pp. 766–769.

MECHANICS

Direct Numerical Simulation of the Statistical Characteristics of Wave Ensembles

S. Yu. Annenkov and V. I. Shrira*

Presented by Academician V.E. Zakharov December 25, 2003

Received February 18, 2004

INTRODUCTION

At present, the nonlinear evolution of random wave fields, including the field of wind-generated waves on the ocean surface, is statistically described in a general nonlinear wave physical approach, where the evolution of the second-order statistical moments is described by a kinetic equation (Boltzmann equation) [1]. This approach is based on the hypothesis that a statistically uniform wave field is quasi-Gaussian or on equivalent hypotheses: odd-order statistical moments are set to zero, and higher even-order moments are expressed in terms of the second-order moments. Although the kinetic equation is successfully applied to a number of various important physical problems [1], its justification, requiring independent verification of the above hypotheses, remains an open problem. Moreover, observations of waves on water often reveal the presence of long-lived coherent structures in the wave field, which contradicts, at first glance, the above hypotheses.

It is most important to determine the applicability limits of the approach based on the kinetic equation by verifying its base hypotheses, including the quasi-Gaussian hypothesis. The applicability conditions for models based on the kinetic equation, as well as factors violating these conditions, can be determined only by direct numerical simulation including the integration of the primitive equations of motion in continuum. In this work, we propose a verification method based on direct numerical simulation for a nonlinear wave field on the surface of a fluid.

Since numerical simulation of hydrodynamic equations must be performed for numerous interacting waves at large time scales much longer than the characteristic times of developed turbulence, the choice of an appropriate numerical method is important. Such a simulation directly for the basic hydrodynamic equations (e.g., Navier–Stokes equations) is beyond the capabilities of current computers. Spectral methods based on the weak-nonlinearity assumption, where a field is represented in terms of a discrete set of interacting Fourier harmonics, are much more appropriate for solving the problem. To efficiently simulate the statistical evolution of the continuous wave field, numerical integration must be performed for a large number of discrete harmonics. In this case, the problems of discretization and role of resonant and nonresonant interactions require special attention. A regular grid in the wave-vector space **k** is usually used in spectral methods, which gives rise to undesirable artifacts of integer discretization [2]. A new approach that is proposed in this work and based on the truncated Hamiltonian equations (Zakharov equation) enables one to overcome these difficulties. In particular, it does not require discretization on regular grids and makes it possible to efficiently simulate any number of interacting waves.

The first attempts to apply spectral methods to direct numerical simulation of the results predicted by the kinetic equation were reported in recent works [3, 4], where it was shown that the final stage of the evolution of wave ensembles obtained with the kinetic equation was close to direct numerical simulation. However, quantitative comparison of evolution itself was not performed.

In this work, we develop a method of direct numerical simulation of random wave fields. This method is applied to reproduce solutions of the kinetic equation, when the latter is applicable, in order to provide the possibility of applying this method for a wider class of problems. It is necessary to answer the following important questions.

(i) Is it fundamentally possible to develop an efficient numerical scheme for a quite accurate simulation of the evolution of statistical characteristics of wave ensembles with the conservation of the fundamental properties of a continuous wave field?

Shirshov Institute of Oceanology,
Russian Academy of Sciences,
ul. Krasikova 23, Moscow, 117218 Russia
e-mail: serge@wave.sio.rssi.ru
**Current address:*
Department of Mathematics,
Keele University, Keele,
ST5 5BG United Kingdom
e-mail: v.i.shrira@maths.keele.ac.uk

1028-3358/04/4906-0389$26.00

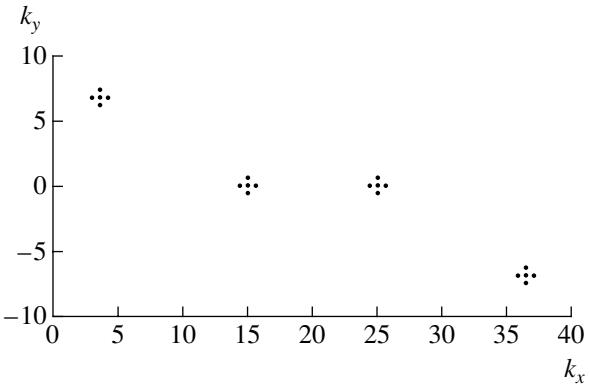

Fig. 1. Wave vectors in the **k** space corresponding to the four-cluster case.

(ii) What is the role of resonant, approximately resonant, and nonresonant interactions?

(iii) What is the form of evolution at the initial stage, whose duration is about the characteristic time of phase mixing?

(iv) How can the above effects modify the initial conditions of the kinetic equation?

In this work, for simplicity, answers to most of these questions are given for a relatively particular case, where the wave field consists of a finite number of localized, spectrally narrow, wave packets that are in exact resonance.

BASIC EQUATIONS AND AN ALGORITHM

Let us consider potential gravity waves with low (about ε) steepness on the surface of a deep incompressible fluid. Following [5], we write the equations of motion in the Hamiltonian form

$$i\frac{\partial b(\mathbf{k})}{\partial t} = \frac{\delta H}{\delta b^*(\mathbf{k})}, \quad (1)$$

where the Hamiltonian H is represented as the integral power series in $b(\mathbf{k})$ and $b^*(\mathbf{k})$:

$$H = \int \omega(\mathbf{k}) b(\mathbf{k}) b^*(\mathbf{k}) d\mathbf{k} + \sum_{n=3}^{\infty} H_n. \quad (2)$$

The dispersion relation has the form $\omega(\mathbf{k}) = (gk)^{1/2}$, where g is the gravitational acceleration, integration is hereinafter performed over the entire **k** plane, and the asterisk stands for complex conjugation. The complex canonical variable $b(\mathbf{k})$ in the Fourier space is expressed in terms of the physical variables $\varphi(\mathbf{k}, t)$ and $\eta(\mathbf{k}, t)$ (potential on the free surface and free-space elevation) through the integral power series

$$b(\mathbf{k}) = \frac{1}{\sqrt{2}}\left\{\sqrt{\frac{\omega(\mathbf{k})}{k}}\eta(\mathbf{k}) + i\sqrt{\frac{k}{\omega(\mathbf{k})}}\varphi(\mathbf{k})\right\} + O(\varepsilon). \quad (3)$$

Then, the evolution equation for $b(\mathbf{k})$ including the leading (four-wave) interactions is written in the form [6]

$$i\frac{\partial b_0}{\partial t} = \omega_0 b_0 + \int V_{0123} b_1^* b_2 b_3 \delta_{0+1-2-3} d\mathbf{k}_{123}, \quad (4)$$

where the compact notation is used with the replacement of arguments by subscripts, e.g., $b_0 = b(\mathbf{k}_0)$. Equation (4) is called the Zakharov equation. Its detailed derivation and expression for V_{0123} were given in [6].

An algorithm for numerically solving Eq. (4) was developed in [7] and successfully applied to integrate dynamic equations in a number of problems. In this work, it is used for the first time to analyze the evolution of the statistical characteristics of wave ensembles. An important feature of the algorithm is a free choice of the position of harmonics in the **k** space. This advantage enables one to remove restrictions imposed by a regular grid, control the presence of exact and approximate resonances in a system, and identify narrow resonant regions for higher order resonances already with a few harmonics.

EVOLUTION OF THE STATISTICAL CHARACTERISTICS OF A WAVE ENSEMBLE

We consider a gravity-wave ensemble consisting of a finite number of quasi-monochromatic wave packets. Let us represent each packet as a cluster of random-phase harmonics such that the sum of their amplitudes squared is equal to the total intensity of a packet and perform phase averaging. The simplest example of such an approach corresponds to four packets in exact resonance (Fig. 1). The kinetic equation for this case can be obtained by discretizing the general kinetic equation [1, 8] or derived directly by using the random phase approximation [9] and has the form

$$\frac{\partial N_0}{\partial t} = 8\pi V_{0123}^2 [N_2 N_3 (N_0 + N_1) - N_0 N_1 (N_2 + N_3)], \quad (5)$$

where $N_j = b_j^2$, $j = 1$–4, is the intensity of the jth wave packet. Each wave packet is represented as a cluster of five harmonics $\mathbf{k}_j$, $\mathbf{k}_j \pm \mathbf{d}_x$, $\mathbf{k}_j \pm \mathbf{d}_y$, where $\mathbf{d}_x = \Delta\kappa_x$, $\mathbf{d}_y = \Delta\kappa_y$, and $\kappa_x = (1, 0)$ and $\kappa_y = (0, 1)$ are the unit wave vectors. The quantity Δ is called the cluster size in the **k** space. Such a procedure of constructing clusters includes the parallel translation of the original resonant quartet by $\mathbf{d}_x$ and $\mathbf{d}_y$ with the appearance of numerous quartets that are in approximate resonance and simulate the modulation instability of the original wave packets. In the taken configuration, the sole resonant quartet in the kinetic equation corresponds to the interaction of 180 coupled quartets in the Zakharov equation.

Figure 2 shows the evolution of packet intensities for a time of about 7000 characteristic periods of waves as obtained by numerically solving the kinetic and Zakharov equations (with averaging over an ensemble

of 1000 realizations each corresponding to a random choice of the initial phases of the harmonics). Both approaches show that the system tends to the thermodynamic equilibrium state, which does not generally correspond to the Rayleigh–Jeans spectrum due to the presence of additional integrals relating the amplitudes of interacting packets (Manley–Rowe integrals).

To illustrate the role of interactions that are not exact resonant interactions, the points in Fig. 2 show numerical solutions of the Zakharov equation for the initial resonant quartet without the introduction of clusters and with averaging over an ensemble of 10 000 realizations. In this case, the harmonic amplitudes evolve with a much shorter time scale and fast, gradually damping, oscillations. Such a numerical solution obtained disregarding approximate resonances differs strongly from the corresponding solution of the kinetic equation and cannot be used to simulate it.

To analyze the dependence of the results on the cluster size Δ, we calculate the ratio of the evolution time scale obtained by direct numerical simulation to that obtained by numerically solving the kinetic equation. This ratio is close to unity in a wide range of Δ, when the cluster size is much smaller than the characteristic size of the system. A moderate increase in the number of elements in each cluster does not noticeably change evolution. In the initial interval [with the characteristic time $O(\varepsilon^{-2})$], evolution obtained by direct numerical simulation in most cases proceeds faster than it follows from the numerical solution of the kinetic equation.

Similar properties are also obtained for much more complex systems consisting of numerous (up to 1000) localized wave packets. As an illustrative example, we present the evolution of the system of 24 wave packets. Figure 3 shows the numerical solution for this system. As is seen, the system tends to the thermodynamic equilibrium state, and direct numerical simulation beyond the initial stage of evolution virtually coincides with the solution of the kinetic equation. Direct calculation of the fourth moments also corroborates that they can be represented in the form of the product of the second moments. This representation is of key importance for the derivation of the kinetic equation.

DISCUSSION

In this work, a new approach based on the integration of the Zakharov equation and representation of packets by clusters is proposed and tested for direct numerical simulation of wave fields. Analysis of the evolution of systems consisting of a finite number of localized interacting wave packets shows that this approach predicts a field evolution quite close to the solution of the kinetic equation when the latter is applicable. Interactions close to resonant interactions play a key role. We emphasize that the inclusion of only exact resonant interactions gives physically meaningless results. Analysis of the test problems also indepen-

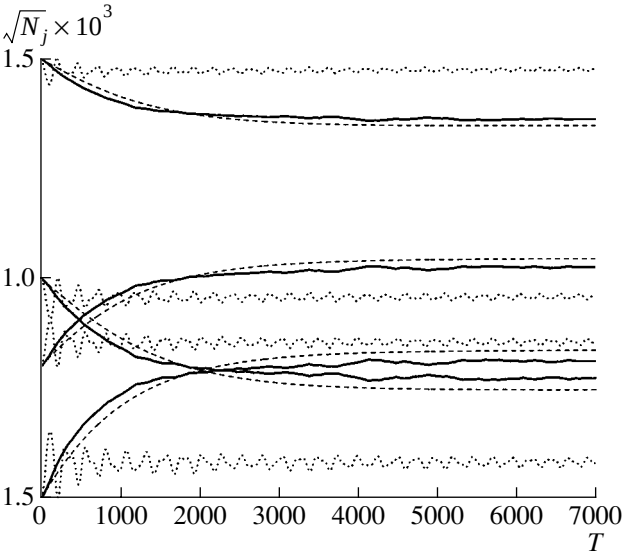

Fig. 2. (Solid lines) Evolution of the intensity of clusters as obtained by numerically solving the Zakharov equation with averaging over an ensemble of 1000 realizations, (dashed lines) numerical solutions of the kinetic equation, and (dotted lines) solutions of the Zakharov equation that are averaged over an ensemble of 10 000 realizations for four harmonics with the same initial conditions for the amplitudes.

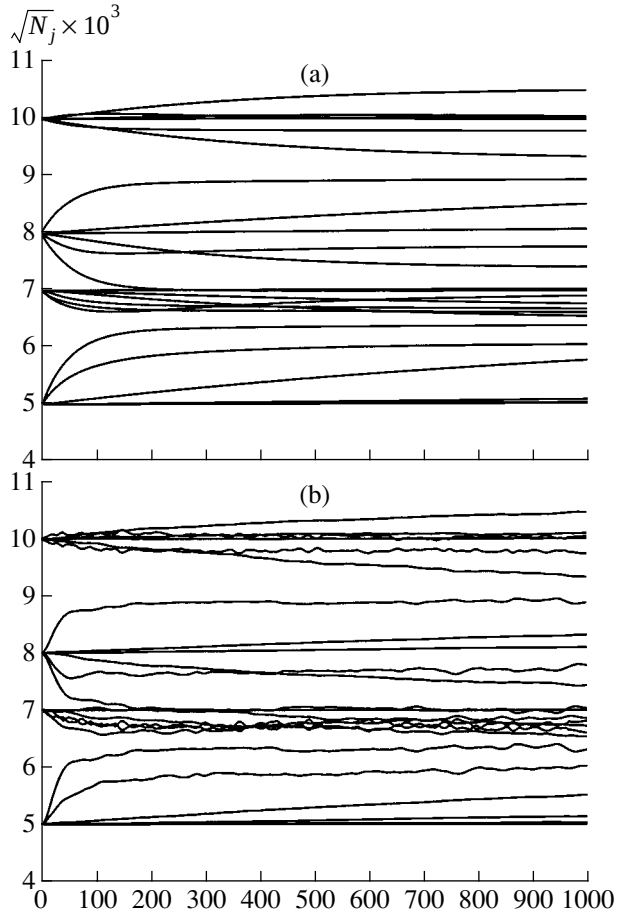

Fig. 3. (a) Numerical solution of the kinetic equation for a discrete ensemble of 24 harmonics and (b) direct numerical simulation for a discrete ensemble of 24 harmonics.

dently corroborates the quantitative adequacy of the kinetic equation at least for the cases being considered.

The above method is supposed to be applied to much more complex cases of the evolution of a continuous wave field, where the kinetic equation is inapplicable and/or higher order resonant interactions must be taken into account. The advantage of the method using arbitrary-form grids becomes substantial already for five-wave interactions for which resonant regions are narrow and cannot be identified by using a regular grid.

ACKNOWLEDGMENTS

This work was supported by the Russian Foundation for Basic Research (project no. 02-05-65140) and INTAS (grant no. 01-234).

REFERENCES

1. E. A. Kartashova, Physica D **54**, 125 (1991).
2. M. Onorato, A. R. Osborne, D. Resio, *et al.*, Phys. Rev. Lett. **89**, 144501 (2002).
3. A. I. D'yachenko, A. O. Korotkevich, and V. E. Zakharov, Pis'ma Zh. Éksp. Teor. Fiz. **77**, 649 (2003) [JETP Lett. **77**, 546 (2003)].
4. V. E. Zakharov, Prikl. Mekh. Tekh. Fiz., No. 2, 86 (1968).
5. V. P. Krasitskii, J. Fluid Mech. **272**, 1 (1994).
6. S. Yu. Annenkov and V. I. Shrira, J. Fluid Mech. **449**, 341 (2001).
7. V. E. Zakharov, Eur. J. Mech. B/Fluids **18**, 327 (1999).
8. V. E. Zakharov, V. S. L'vov, and G. Falkovich, *Kolmogorov Spectra of Turbulence I: Wave Turbulence. Springer Series in Nonlinear Dynamics* (Springer, Berlin, 1992).
9. B. B. Kadomtsev, *Collective Phenomena in Plasma* (Nauka, Moscow, 1976).

Translated by R. Tyapaev

Doklady Physics, Vol. 49, No. 6, 2004, pp. 393–395. Translated from Doklady Akademii Nauk, Vol. 396, No. 6, 2004, pp. 770–772.

MECHANICS

Hydrodynamic Instability Caused by the Anomalous Temperature Dependence of the Water Density

V. I. Bukreev

Presented by Academician G.G. Chernyĭ March 19, 2004

Received March 15, 2004

Under normal conditions, the density of water is maximal at a temperature of about 4°C (the exact value depends on both pressure and the impurity content). This fact leads to a number of effects, including hydrodynamic ones. When water masses whose temperatures are higher or lower than 4°C come into contact, a maximum-density front surrounded by water of lower density is formed in the contact zone. Conditions for the formation of a horizontal maximum-density front arise in fresh water reservoirs. Another effect is the appearance of a seasonal thermal bar in lakes and water reservoirs [1] with a more complicated orientation of this front. In Lake Baikal, processes associated with the anomalous dependence of the water density on temperature significantly affect the oxygen enrichment of deep water layers and the transportation of nutrients into surface layers [2, 3].

In the gravitational field, water particles of the maximum density are subjected to the action of the force directed downward (the difference between the gravity force and buoyancy force). In this case, the development of instability is possible. In essence, this instability is similar to the well-known Rayleigh–Taylor instability [4, 5], although it has a substantial intrinsic feature. The instability of initially immovable unboundedly thick layers with the horizontal interface is usually considered for the case, where the upper layer has a higher density. Under actual conditions, the maximum-density layer is thin and can be arbitrarily oriented.

In this paper, we present brief information on the results of laboratory experiments in which the orientation of the front of the maximum water density continuously varied from the vertical orientation to the horizontal one. The experiments were carried out in a 6-cm-wide ill-drained Plexiglas channel 2.5 m in length. The channel was filled with a 7.6-cm-deep water layer with temperature T_1. A water jet of temperature T_2 and volume flow rate of 66.7 $cm^3\ s^{-1}$ was injected into this initially quiescent water layer over a plate inclined at an angle of 13.4° to the channel bottom. In the simplified form, such a statement of the problem allows us to study processes governing the propagation of water of the Selenga River in Lake Baikal in the spring thermal bar period. The injection occurred for a limited time interval. During the experiment, the water depth in the channel increases by 5 cm.

Figures 1 and 2 present photographs obtained in two experiments for different combinations of T_1 and T_2. All other conditions in both experiments were the same, including a density difference of 0.00034 g cm^{-3}

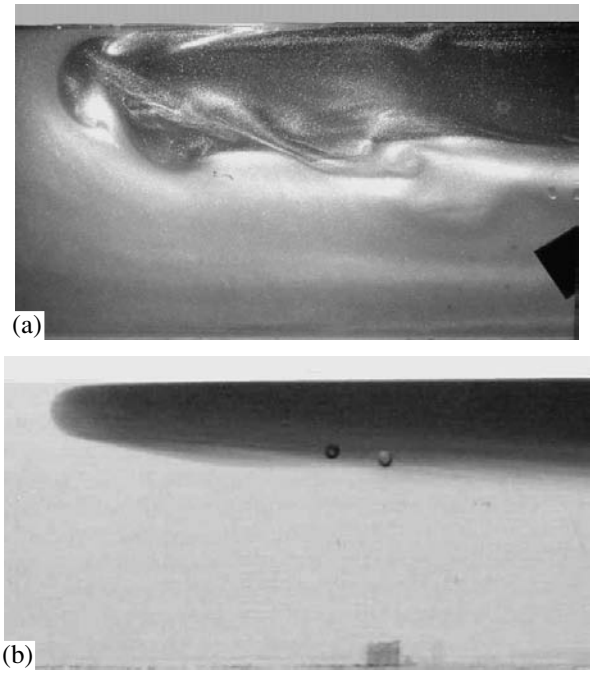

Fig. 1. Leading part of a jet at t = 165 s in experiments (a) 1 and (b) 2.

Lavrent'ev Institute of Hydrodynamics, Siberian Division, Russian Academy of Sciences,
pr. Akademika Lavrent'eva 15, Novosibirsk, 630090 Russia
e-mail: bukreev@hydro.nsc.ru

1028-3358/04/4906-0393$26.00 © 2004 MAIK "Nauka/Interperiodica"

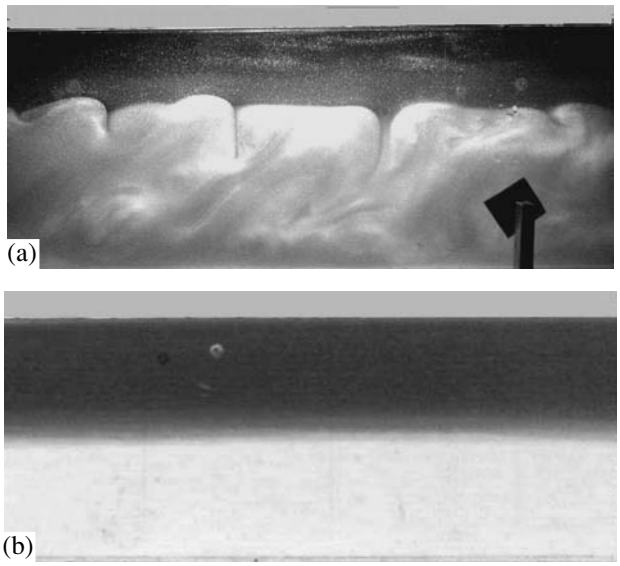

Fig. 2. Stratification pattern at $t = 350$ s in experiments (a) 1 and (b) 2.

between the quiescent layer and jet. In experiment 1, the temperatures were $T_1 = (0.5 \pm 0.2)$°C and $T_2 = (11.7 \pm 0.1)$°C, so that the maximum-density temperature was between these values. In experiment 2, $T_1 = (11.5 \pm 0.1)$°C and $T_2 = (14.2 \pm 0.1)$°C; i.e., both values were higher than the maximum-density temperature. Due to the existence of the density difference, the warmer liquid propagated near the free surface in both experiments. However, when warm water came into contact with cold water in experiment 1, an unstable front of the maximum density was formed, whereas in experiment 2, conditions for the development of the instability under discussion were absent.

Figures 1 and 2 show flow patterns recorded in experiments (a) 1 and (b) 2 at the same time t from the onset of the jet injection. The photographs were taken through the side channel wall. Preliminary experiments have revealed an optimal method of visualizing effects caused by the anomalous temperature dependence of the density. For example, in experiment 1, the most suitable method implied the use of uncolored water with temperature T_2, whereas small suspended particles of aluminum powder reflecting incident light were added into water of temperature T_1. In this case, a vertical light "knife" with a thickness of about 1.5 cm was used to illuminate a flow region near the longitudinal symmetry plane of the channel. In experiment 2, water of temperature T_1 was not colored, whereas water of temperature T_2 was colored with ink. The entire bulk of the liquid was illuminated. For both visualization methods, water of temperature T_2 was darker in the photographs.

In experiment 1, the instability of the maximum-density front led to the continuous variation of the flow pattern from the instant of the jet injection to the complete equalization of temperature. In experiment 2, instability was observed only in the initial time interval with a duration of about 20 s. This instability was caused by only the velocity shift between the different-density layers. Afterwards, due to the stabilizing effect of the buoyancy force directed upward in this case, the flow in this experiment became stable even in the zone of the jet injection.

The photographs were obtained (Fig. 1) at the instant the water supply was ceased and (Fig. 2) when the velocity shift between the two layers virtually vanished. The photographs show that the instability caused by the anomalous temperature dependence of density qualitatively changes the shape and internal structure of the leading part of the surface jet (Fig. 1). For long times, isolated jets of warmer water descend into cold water (Fig. 2a). In the case of thick unstable layers, a similar pattern usually exists only at the initial stage of the development of the Rayleigh–Taylor instability. Thereupon, instability is enhanced due to the excess potential energy of the entire upper layer, and the mixing process becomes chaotic.

Instability seen in Fig. 2a is caused by the excess potential energy of only the thin layer near the maximum density, whereas the density difference between this layer and the surrounding liquid is small. Under these conditions, the molecular thermal diffusion and viscosity of the liquid can efficiently counteract the development of the chaotic motion. In this experiment, the chaotic stage of the instability was not observed. Temperature over the channel depth was equalized slower than upon chaotic mixing but much faster than in experiment 2. In the experiment with the lower-layer temperature $T_1 = 2.8$°C, the excess potential energy was so low that the molecular diffusion suppressed the instability even at the initial stage. In this case, the flow pattern with concentrated jets shown in Fig. 2a was not observed.

The experiment for $T_1 = 14.1$°C and $T_2 = 0.4$°C was carried out such that the cold water propagated over the channel bottom. At long times after ceasing the water flow supply, the characteristic distance between the concentrated jets in the stratification pattern was considerably smaller than in the pattern given in Fig. 2a. In this case, the concentrated jets of the warm liquid descended into the cold liquid, and the cold liquid ascended into the warm liquid.

It is worthwhile to compare the given illustrations with photographs from [7, 8]. In [7], the process of the jet propagation along the interface between two liquids of different densities was analyzed in the absence of anomalous effects. Under these conditions, only the shear instability was manifested. In [8], the Rayleigh–Taylor instability of a liquid heated from the bottom was investigated.

In experiments with other flow rates and initial depths, two more effects caused by the anomalous tem-

perature dependence of the water density were found. Under certain conditions, warmer water with the maximum-density front like a piston can displace the cold water in the entire depth of the channel. In this case, after ceasing the water flow supply, the similarity with the processes near a thermal bar becomes particularly close. For larger values of both the initial depth and the flow rate, shear instability was developed. In the absence of the maximum-density front, it is similar to the well-known Kelvin–Helmholtz instability [6]. In the presence of the maximum-density front, the region of the existence of shear instability and the character of its development changed significantly. The maximum-density front counteracted the development of the shear instability and, at the same time, was unstable itself.

ACKNOWLEDGMENTS

I am grateful to N.V. Gavrilov and A.V. Gusev for their help in performing the experiments. This work was supported by the Russian Academy of Sciences (Integration Program no. 3.13.1) and Siberian Division, Russian Academy of Sciences (Program “Gidrodinamika Vod Baĭkala”).

REFERENCES

1. S. S. Zilitinkevich, K. D. Reiman, and A. Yu. Terzhevik, J. Fluid Mech. **236**, 27 (1992).
2. M. N. Shimaraev, V. I. Verbolov, N. G. Granin, and P. P. Sherstyankin, *Physical Limnology of Lake Baikal: A Review* (Baikal Int. Center Ecol. Res., Irkutsk, 1994).
3. V. I. Kwon and D. V. Kwon, Vychisl. Tekhnologii **2** (5), 46 (1997).
4. Lord Rayleigh, Philos. Mag. **32**, 529 (1916).
5. G. I. Taylor, Proc. R. Soc. London, Ser. A **132**, 499 (1931).
6. J. S. Turner, *Buoyancy Effects in Fluids* (Cambridge Univ. Press, Cambridge, 1973; Mir, Moscow, 1977).
7. R. E. Britter and J. E. Simpson, J. Fluid Mech. **112**, 459 (1981).
8. J. W. Elder, J. Fluid Mech. **32** (1), 69 (1968).

Translated by G. Merzon

Doklady Physics, Vol. 49, No. 6, 2004, pp. 396–400. Translated from Doklady Akademii Nauk, Vol. 396, No. 6, 2004, pp. 773–778.

MECHANICS

Experimental Investigation of a Boundary Layer on the Attachment Line of a Swept Wing

Corresponding Member of the RAS V. Ya. Neyland and V. M. Filippov

Received December 25, 2003

The turbulent regime attracts constant interest, because it often occurs in flows of fluids and gases under both natural and artificial conditions. Interest in the turbulence problem in motion of bodies in gases and fluids is primarily associated with the laminar–turbulent transition that occurs in the boundary layer and whose mechanism depends sometimes on the place (conditions) of its origin. In particular, when the boundary layer is developed on a swept wing, the transition can occur, first, on the attachment line, second, near the front edge in the domain of secondary-flow instability, and, third, downstream due to the instability of Tollman–Schlichting waves.

The laminar–turbulence transition on the attachment line leads to the turbulization of the entire boundary layer on the wing. For this reason, study of the features of this transition is of particular interest. The basic aim of this work is to experimentally investigate the features of the development of the boundary layer along the attachment line of a forward swept wing narrowed to the end. The boundary layer is developed from the region of large perturbations that is located at the place of connection of the front model end and the wall of the working section of an aerodynamic tube with a turbulent layer on it (see Fig. 1). Detailed results are obtained for the statistical and pulsation characteristics of the laminar–turbulence transition region and previous relaxation zone. Experimental investigations of the boundary layer on the attachment line were previously carried out under the conditions of its development either from the region of uncontrollable large perturbations (attachment of a wing with the fuselage of an airplane and a model with the wall of the aerodynamic tube $Z = 0$) known as the contamination regime or from the region of artificially induced perturbations. In the latter case, the turbulization of the layer is realized primarily by mounting wires of various diameters d on the surface of the front edge perpendicularly to the attachment line. Investigations were primarily focused on the determination of the Reynolds numbers of the beginning $\mathrm{Re}_{\theta b}$ and end $\mathrm{Re}_{\theta e}$ of the transition region as functions of the distance Z from a turbulizer:

$$\mathrm{Re}_\theta = F\left(\frac{d}{\eta}, \frac{Z}{\eta}\right),$$

where $\eta = 2.47\theta$ is the length scale proportional to the momentum-loss thickness θ. The Reynolds number is calculated by the formula [3]

$$\mathrm{Re}_\theta = 0.404\left(\frac{U_0 r \sin\chi\tan\chi}{2\nu}\right)^{0.5},$$

where U_0 is the velocity of the free flow, r is the radius of the front edge in the cross section orthogonal to the front edge, χ is the swept angle, and ν is the kinematic viscosity. The applicability of this formula to individual cases is verified experimentally. The effect of turbulence ε in an incompressible flow is disregarded.

According to [1–5], the first turbulent bursts appear in an incompressible boundary layer quite far from the region of large perturbations at the minimum Reynolds number $\mathrm{Re}_{\theta cr} = 90$–$105$. For $\mathrm{Re}_\theta < \mathrm{Re}_{\theta cr}$, all perturbations are damped downstream. For $\mathrm{Re}_\theta > \mathrm{Re}_{\theta cr}$, the laminar–turbulence transition occurs, leading to the complete turbulization of the layer for $\mathrm{Re}_\theta > 120$.

Virtually all basic experimental results on the development of the boundary layer were obtained by hot wire anemometers. The beginning of the transition was identified by the appearance of the first turbulent bursts, and the end of the transition was detected by the complete disappearance of laminar regions. Because of the considerable uncertainty, the end of the transition region was not determined [5]. Information on any characteristics of the laminar–turbulence transition region and on the effect of incident-flow turbulence on the development of the boundary layer along the attachment line is absent, although its importance is widely recognized. It is difficult to identify the beginning of the transition even under the comparatively simple conditions of the two-dimensional boundary layer. Different criteria used for this identification yield considerably different results [6, 7]. In particular, the determination of the transition by a hot wire anemometer yields $\tau_b =$ 600 and 500 mm when using the criteria of the mini-

Zhukovsky Central Aerohydrodynamic Institute (TsAGI), Zhukovskiĭ, Moscow oblast, 140160 Russia

1028-3358/04/4906-0396$26.00

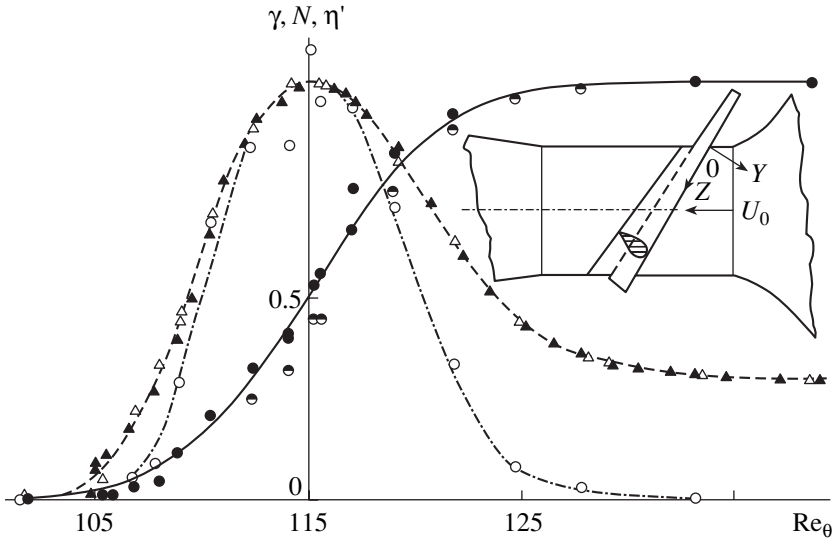

Fig. 1. Typical (●, ◓) intermittence coefficient γ, (○) frequency $N = \frac{n}{n_{\max}}$ of changing the flow regimes, and (▲, △) rms intensity of the pulsation intensity $\eta' = \frac{\sqrt{\overline{l'^2}}}{\sqrt{\overline{l'^2_{\max}}}}$. The inset shows the position of the model in the working section of the tube.

mum local surface friction τ_w and intermittence coefficient $\gamma = 1\%$, respectively [7].

This work is primarily focused on the determination of the boundaries of the laminar–turbulence transition region and its statistical and pulsation characteristics, which are possibly obtained for the first time in such detailed and thorough experiments.

The model is a truncated cone with a wedge tail cowl (Fig. 1). It was horizontally mounted at $\chi = 51.4°$ in the middle plane of the $1 \times 1 \times 4$-m working section of a T-124 aerodynamic tube at the Zhukovsky Central Institute of Aerohydrodynamics. At the upper point of connection of the attachment line with the lateral wall ($Z = 0$), the model has curvature radius $r = 61.2$ mm and $dr/dz = 0.0205$. The chord of the model along the normal to the attachment line was $b = 4r$, and the roughness of the surface near the front edge was $R_a \approx 1.64$ μm.

Incident-flow turbulence

$$\varepsilon = \sqrt{\frac{\overline{u'^2} + \overline{v'^2} + \overline{w'^2}}{3U_0^2}}$$

increases linearly from 0.02% for the flow velocity $U_0 \le 20$ m/s to 0.055% for $U_0 = 35$ m/s, then remains virtually constant to $U_0 \approx 60$ m/s, and again increases linearly to 0.08% for $U_0 = 100$ m/s. For $U_0 \le 20$ m/s, $\varepsilon \approx 0.02\%$ and all components of the pulsation velocity are equal to each other, $\varepsilon_u = \frac{\sqrt{\overline{u'^2}}}{U_0} = \varepsilon_v = \varepsilon_w$. For $U_0 \ge 20$ m/s, $\varepsilon_u \approx 0.6\varepsilon_v = 0.6\varepsilon_w$.

Turbulence varied slightly along the working section and decreased slightly downstream. The mounting of the model did not noticeably change the turbulence of the free flow. Measurements of the frequency distribution of pulsation intensity $\varepsilon_u = F(f)$ showed that most of the energy is concentrated in the range $U_0 \le 30$ Hz for velocities $U_0 \le 30$ m/s. With an increase in velocity U_0, intensity ε_u increased primarily in the low-frequency band of the spectrum, and the spectrum had pronounced peaks, e.g., at $f \approx 10$, 20, 48, 56, 60 Hz for $U_0 \approx 70$ m/s.

The turbulence of the flow was increased by mounting a turbulizing grid at the end of the tube collector. Measurements yielded $|\bar{\varepsilon}|_u = 1.32$, 1.15, and 0.88% in three cross sections at distances $X \approx 0.5$, 1.0, and 1.8 m, respectively, from the entry of the working section. Deviations of ε_u from the above average values $\bar{\varepsilon}_u$ were about $\pm 0.1\%$ $\bar{\varepsilon}_u$ in the working velocity range. Measurements in the cross section $X = 1.8$ m were carried out in the empty tube.

The characteristics of the boundary layer were measured by a hot wire anemometer with constant resistance and copper-coated tungsten-filament sensors 4.5 μm in diameter. The outer copper coating was removed from a sensitive tungsten element by chemical etching in a film of water solution of nitric acid [8] in a special setup [9].

Work was performed in two stages. At the first stage, a superimposed sensor based on a 40-μm-thick polyamide film was used. A sensitive element was placed at the beginning of the film parallel to its front cut. The

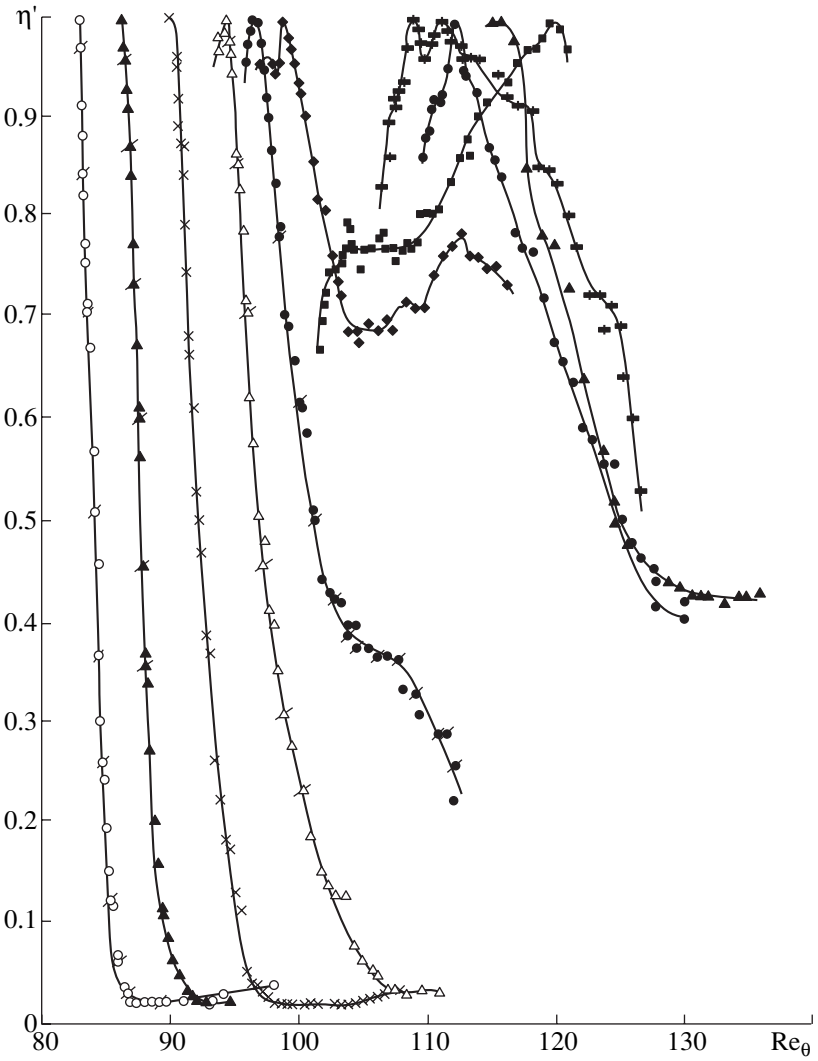

Fig. 2. Variation of the pulsation intensity η' along the attachment line moving away from the connection point (Z = 0) with the wall for Re_1 (in 10^6 m^{-1}) = (○) 1.35, (▲) 1.45, (×) 1.57, (△) 1.72, (●) 1.80, (◆) 1.88, (■) 2.02, (▬) 2.22, (●) 2.36, and (▲) 2.59 and for $\mathrm{Re}_\theta = 0.2824\sqrt{\mathrm{Re}_1} \times \sqrt{0.0205Z + 0.0612}$. Crossed points are obtained in the reverse motion (decrease in velocity U_0).

sensor was mounted at a chosen place of the streamlined surface by vacuum grease. After the relocation of the sensor to a new place, grease residues were removed by a kerosene-moistened tampon without changing the roughness of the surface. At the second stage, the characteristics of the boundary layer were measured by a specially designed coordinate system ensuring the displacement of the sensor along the attachment line with an accuracy of 1 mm at a distance of $\bar{Y}_0 \approx 0.2$ mm from the streamlined surface. The systematic measurements of the distance Y_0 over all the length Z by the noncontact thermal method showed that deviation from the average value $\bar{Y}_0$ were no more than 20 μm.

The constant component $E \sim F(U)$ of the signal and its rms component $\sqrt{\overline{l^{12}}} \sim F(\sqrt{\overline{u^{12}}})$ with sufficient averaging time were measured in experiments. Instantaneous pulsations l' were observed on an electron oscillograph, detected on oscillograms by a train oscillograph, and used to determine the intermittence coefficient γ and frequency n of changing flow regimes. To determine the flow parameters, pressure and temperature were measured simultaneously. At the first and second stages, the temperature of the flow varied from about 5 to 15°C and from about 20 to 30°C, respectively.

Figure 1 shows the typical characteristics measured for the boundary layer in the laminar–turbulence transition region. As is seen, the accuracy and reliability of the results are comparatively high. At the second stage, measurements in the cross section Z = 975 mm were performed in two experiments with an interval of six days. Only E and $\sqrt{\overline{l^{12}}}$ were measured in the first exper-

iment, and $l' = F(t)$ was additionally recorded in the second experiment. These results enabled us to obtain data on the intermittence coefficient γ and frequency n of changing flow regimes. The results of the first two experiments were identical. The differences between $\overline{\mathrm{Re}}_\theta$ values at the maxima of functions $\eta' = F(\mathrm{Re}_\theta)$, $N = F(\mathrm{Re}_\theta)$, and $\gamma_{0.5} = (\mathrm{Re}_\theta)$ were equal to about 1%. The solid line of dependence $\gamma = f(\mathrm{Re}_\theta)$ corresponding to the normal distribution of a random value with the parameters $\overline{\mathrm{Re}}_\theta = 115$ and $\sigma = 5$ agrees satisfactorily with experimental points.

The transition-region beginning, which was associated with the detection of the first turbulent bursts (centers of turbulent spots), as well as the corresponding change in the rate of increasing pulsations η' and intermittence coefficient γ, occurred at $\mathrm{Re}_{\theta b} \approx 102$. The transition-region end, which was associated with the complete disappearance of laminar regions ($N = 0$ and $\gamma = 1$), occurred at $\mathrm{Re}_{\theta e} = 132$, where a decrease in the pulsation intensity $\eta' = f(\mathrm{Re}_\theta)$ was virtually completed. Analysis of measurements of these characteristic points of the transition region in experiments at the first stage in five cross sections $Z > 0.3$ m showed that their deviations from the average values were less than 1%. The measurements of dependence $E = F(\mathrm{Re}_\theta)$ did not provide such a high accuracy of determining the boundaries of the transition region and overestimated the beginning of the transition region and underestimated its end. It was found that measurements of the dependence $\eta' = F(\mathrm{Re}_\theta)$ provided most simple and sufficiently accurate investigations of the boundary layer.

Although oscillographic records of pulsations $l' = F(t)$ extend information on the properties of the laminar–turbulence transition, they strongly increase the laboriousness of experiments and data processing.

Figure 2 shows the results of detailed measurements of the dependence $\eta' = F(\mathrm{Re}_\theta)$ for ten Re_1 values from 1.35×10^6 to 2.59×10^6 m^{-1}. Analysis of data and similar results for some of the above Re_1 values in the form $\gamma = F(\mathrm{Re}_\theta)$ and $N = F(\mathrm{Re}_\theta)$ made it possible to reconstruct the following scenario of boundary-layer development along the attachment line from the high-turbulence (contamination) zone toward higher Re_θ values (radius of the front edge of the wing).

First, for $\mathrm{Re}_\theta < 100$ and moving away from the contamination zone, the intensity of pulsations decreases in the boundary layer on the attachment line, which gives rise to the intermittent flow regime with $\gamma \neq 1$ at a certain distance Z. For $\mathrm{Re}_1 < 1.75 \times 10^6$ m^{-1}, the intermittent flow regime is completed at a certain distance Z_l with the formation of a pure laminar boundary layer with $\gamma = 0$, which extends to the end of the model. With an increase in Re_1, turbulence relaxes in a region of higher Re_θ values that increases its length due to a decrease in the laminar section of the layer, which virtually disappears for $\mathrm{Re}_1 \approx 1.8 \times 10^6$ m^{-1}.

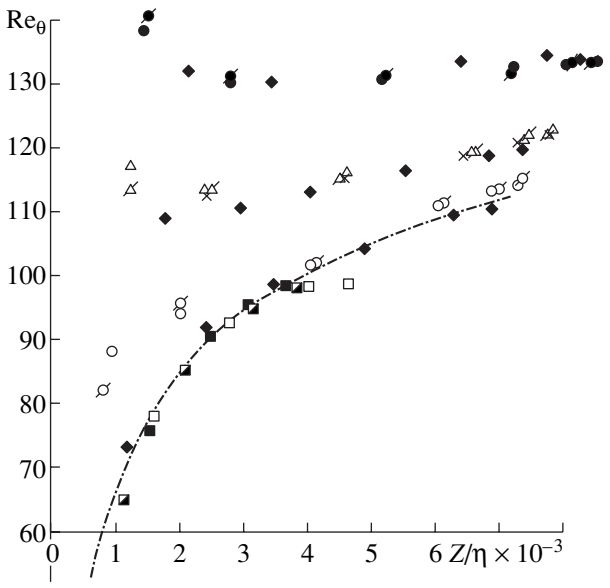

Fig. 3. Reynolds numbers of the beginning $\mathrm{Re}_{\theta b}$, middle $\overline{\mathrm{Re}}_\theta$, and end $\mathrm{Re}_{\theta e}$ of the transition region in various cross sections along the attachment line ($\eta = 0.404\theta$): (○) $\eta' = F(\mathrm{Re}_{\theta\,b})$, (⌀) n, (×) $\gamma = F(\overline{\mathrm{Re}}_\theta)$, (△) η', (⌀) n, (●) $\eta' = F(\mathrm{Re}_{\theta\,e})$, (⌀) n, (◆) the second stage ($\mathrm{Re}_{\theta\,b}$, $\overline{\mathrm{Re}}_\theta$, $\mathrm{Re}_{\theta\,e}$). The line is obtained by Eq. (1), and data are taken from Fig. 8 in [3] for a cylinder with sliding and a turbulizer plate along the flow for χ = (□) 55°, (◪) 60°, and (■) 65°.

A further increase in Re_1 transforms the incomplete relaxation regime to the turbulization regime, whose position is shifted upstream along the attachment line. In particular, for $\mathrm{Re}_1 = 1.88 \times 10^6$ m^{-1}, relaxation is completed in the cross section $Z = 0.5$ m ($\mathrm{Re}_\theta = 104$, $\eta' = 0.7$, $\gamma = 0.25$, and $n = 150$ Hz), and then the intermittence coefficient and pulsation intensity remain approximately constant up to $Z = 0.95$ m ($\mathrm{Re}_\theta = 110$). For $\mathrm{Re}_1 = 2.02 \times 10^6$ m^{-1}, relaxation is completed in the cross section $Z = 0.3$ m ($\mathrm{Re}_\theta = 104$ and $\gamma = 0.6$), and the transition (increase in pulsation intensity) begins in the cross section $Z = 0.6$ m ($\mathrm{Re}_\theta = 109$).

Figure 3 shows the number Re_θ of the disappearance of the last turbulent bursts as a function of the distance $\frac{Z}{\eta}$ from the source of large perturbations along with the data taken from [3] for a cylinder and numbers $\overline{\mathrm{Re}}_\theta$ and $\mathrm{Re}_{\theta e}$ obtained in this work. The dash–dotted line is calculated under the assumption that

$$\int_0^{Z_l} (\mathrm{Re}_{\theta\,\mathrm{cr}} - \mathrm{Re}_{\theta z})\,dz = \mathrm{const}, \qquad (1)$$

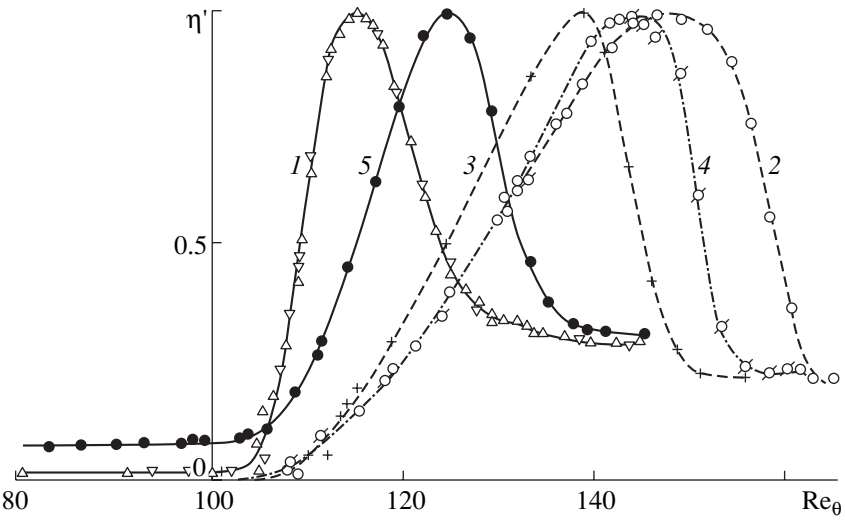

Fig. 4. Effect of the Gaster-bump turbulizer and flow turbulence on the laminar–turbulence transition for Z = 975 mm (*1*) without the Gaster bump, (*2*) with the Gaster bump, (*3*) with the lacquer-coated Gaster bump, (*4*) after the polishing of the lacquer coating of the Gaster bump, and (*5*) similar to the fourth case but with the turbulizing grid.

where const corresponds to the average value for $\mathrm{Re}_1 \le 1.72 \times 10^6$ m^{-1} (Fig. 2).

The coordinates of the points for the second stage were obtained from the dependences $\eta' = F(\mathrm{Re}_\theta)$ measured in the cross sections Z = 275, 475, 675, 975, 1275, and 1400 mm. As is seen, with an increase in the distance Z, the number $\mathrm{Re}_{\theta b}$ increases and the number $\mathrm{Re}_{\theta e}$ remains virtually a constant of about 132. An increase in the flow turbulence somewhat shifts the laminar–turbulence transition region towards smaller numbers Re_θ.

More extensive results on the effect of the turbulence of the free flow on the laminar–turbulence transition in the boundary layer on the attachment line were obtained under the strong weakening of the contamination effect by mounting a special Gaster bump in the path of large perturbations propagating from the connecting domain of the model with the walls of the working section (Fig. 4).

The plots in Fig. 4 in the form of the dependence $\eta' = F(\mathrm{Re}_\theta)$ clearly illustrate the effect of the Gaster bump and turbulence ε_u on the position of the laminar–turbulence transition region. In particular, the weakening of contamination increases $\overline{\mathrm{Re}}_\theta$ from 115 to 148, and the transition-region end $\mathrm{Re}_{\theta e}$ is shifted from 133 to 163. At the same time, the effect of the surface roughness of the bump on the efficiency of its action on the flow in the boundary layer is observed.

Due to the increase in flow turbulence, the numbers $\overline{\mathrm{Re}}_\theta$ and $\mathrm{Re}_{\theta e}$ decreased from 144 to 125 and from 158 to 140, respectively. At the second stage, experiments were carried out in the cross section Z = 975 mm in the following sequence: first, without a turbulizing grid and Gaster bump; second, without the turbulizing grid and with the Gaster bump; third, without the turbulizing grid and with the lacquer-coated Gaster bump; fourth, similar to the third case after the polishing of the Gaster bump; and, fifth, similar to the fourth case with the turbulizing grid.

ACKNOWLEDGMENTS

This work was supported by the Russian Foundation for Basic Research (project no. 01-01-00190).

REFERENCES

1. M. Gaster, Aeronaut. Quart. **18**, 165 (1967).
2. N. A. Cumpsty and M. R. Head, Aeronaut. Quart. **20**, 99 (1969).
3. D. I. A. Poll, Aeronaut. Quart. **30**, 607 (1979).
4. D. I. A. Poll, Aeronaut. Quart. **34**, 1 (1983).
5. D. I. A. Poll and D. J. Paisley, Aeronaut. J. **89**, 109 (1985).
6. W. Nitsche and J. Szobruch, in *Proceedings of the International Congress on Aerodynamic Sciences, Stockholm, 1990*, Vol. 1, pp. 197–209.
7. W. J. Feiereisen and M. Acharya, AIAA J. **24**, 1642 (1986); Aérokosm. Tekhn., No. 4, 14 (1987).
8. V. M. Filippov and V. K. Kolesnikov, USSR Inventor's Certificate No. 163480, Byul. Izobr., No. 12 (1964).
9. V. K. Kolesnikov and V. M. Filippov, USSR Inventor's Certificate No. 264015, Byul. Izobr., No. 8 (1970).

Translated by R. Tyapaev